Magnetodielectric Coupling in Multiferroic Transition Metal Oxides

COVER: *A 2D projection of 3D plot of the dielectric constant of $Y_2Cu_2O_5$ as a function of the temperature and the magnetic field, see Chapter 3.*

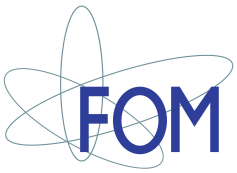

University of Groningen
Zernike Institute
for Advanced Materials

The work described in this thesis was performed in the group "Solid State Chemistry" (part of the Zernike Institute for Advanced Materials) of the University of Groningen, The Netherlands. This work is sponsored by the "Stichting voor Fundamenteel Onderzoek der Materie" (FOM) which is financially supported by the "Nederlandse organisatie voor Wetenschappelijk Onderzoek" (NWO).

PRINTED BY: FACILITAIR BEDRIJF RUG, GRONINGEN. September 2008.

ISBN No: 978-90-367-3566-7

Zernike Institute for Advanced Materials Ph.D. thesis series 2008-26

ISSN 1570-1530

RIJKSUNIVERSITEIT GRONINGEN

Magnetodielectric Coupling in Multiferroic Transition Metal Oxides

Proefschrift

ter verkrijging van het doctoraat in de
Wiskunde en Natuurwetenschappen
aan de Rijksuniversiteit Groningen
op gezag van de
Rector Magnificus, dr. F. Zwarts,
in het openbaar te verdedigen op
vrijdag 24 oktober 2008
om 14:45 uur

door

Umut Adem

geboren op 9 juli 1979
te Ankara, Turkije

Promotor:	Prof. Dr. Thomas T. M. Palstra
Copromotor:	Dr. Graeme R. Blake

Beoordelingscommissie:	Prof. Dr. Bernd Büchner
	Prof. Dr. Tsuyoshi Kimura
	Prof. Dr. Charles Simon

To my parents

Contents

CHAPTER 1

Introduction

1.1. Historical Development of the Field of Linear Magnetoelectrics and Multiferroics

1.1.1. Multiferroics

After 30 years of limited activity, the field of linear magnetoelectrics and multiferroics research has been "revived" from 2000 onwards. Because the topic of multiferroics and magnetoelectrics involves both ferroelectric and magnetic properties of matter, it has attracted researchers from both backgrounds: magnetism and ferroelectricity. The term *multiferroic* was coined relatively late, in 1994 by H. Schmid [1]. It refers to materials that have either two or three different ferroic orders at the same time: ferromagnetism, ferroelectricity and ferroelasticity. However, the general usage of this term is not restricted to ferromagnets only, but antiferromagnets with ferroelectric order are also included. In this thesis, the term *multiferroics* implies simultaneous ferroelectric and magnetic ordering rather than ferroelastic ordering. In the earlier literature, the term *ferroelectromagnet* was used to refer to the same set of materials [2]. The revival of research into magnetoelectrics and multiferroics coincided with the integration of ferroelectric thin films and new high-k dielectrics in Si technology starting in the 1990s. This integration became possible because fabrication using newly developed thin film technology decreased the voltages necessary to switch polarization (thereby to store charge) to less than 5 Volts. Multiferroic thin films allow the coupling of polarization P to

magnetization M, which can be potentially exploited for multiple-state memory elements. This multistate memory can be read magnetically (non-destructive readout) and can be erased and rewritten electrically (faster and less power consuming than magnetic rewriting). However, applications such as multistate memories are still far away on the horizon. This is mainly due to three reasons: 1) There exist only a few materials that are multiferroic at RT; 2) The coupling between P and M in multiferroics is so weak that one needs very high electric (magnetic) fields to switch the magnetization (electrical polarization); 3) Another problem for many multiferroics and linear magnetoelectrics is the fact that they are bad insulators. This limits electrical characterization leading to the erroneous analysis of systems.

1.1.2. Linear Magnetoelectrics

Linear magnetoelectrics are different to multiferroics in the sense that they are also magnetically ordered oxides but they do not possess spontaneous electrical polarization. Nevertheless, electrical polarization (magnetization) can be induced by applying a magnetic (electric) field. Since the presence/absence of the linear magnetoelectric effect is a symmetry property, materials allowing a linear magnetoelectric effect can be distinguished using the magnetic point group of the materials. The Landau free energy is invariant with respect to the symmetry operations of the magnetic space group. The Landau free energy expression for linear magnetoelectric materials contains a term linear in E and H:

$$\phi = \phi_0 - \alpha_{ij} E_i H_j \tag{1.1}$$

The subscripts i,j and k refer to the three directions of a right-handed Cartesian coordinate system, ϕ_0 is the free energy for E = H = 0, and α_{ij} is the magnetoelectric susceptibility tensor. The derivative of this free energy with respect to E(H) gives the polarization, P (magnetization, M), in terms of the applied magnetic (electric) field H(E):

$$P_i = -\frac{\partial \phi}{\partial E_i} = \alpha_{ij} H_j \tag{1.2}$$

$$M_j = -\frac{\partial \phi}{\partial H_j} = \alpha_{ij} E_i \tag{1.3}$$

The free energy may contain terms that are nonlinear in E and H, in which case we have nonlinear, higher order magnetoelectric effects.

$$\phi = \phi_0 - \alpha_{ik} E_i H_k - \frac{1}{2}\beta_{ijk} E_i H_j H_k - \frac{1}{2}\gamma_{ijk} H_i E_j E_k \tag{1.4}$$

There is a theoretical limit to the magnetoelectric coupling [3], where α_{ij} is the magnetoelectric susceptibility tensor, ε_{ii} is the dielectric permittivity and μ_{jj} is the magnetic permittivity.

$$\alpha_{ij}^2 < \varepsilon_{ii}\mu_{jj} \tag{1.5}$$

Therefore, larger coupling might be expected for systems that are simultaneously ferromagnetic and ferroelectric in general. We note that this limit to magnetoelectric coupling applies to materials that have linear coupling terms. Materials that display higher-order magnetoelectric effects might overcome this limit [4].

It is worth stressing that a linear magnetoelectric is not necessarily a multiferroic. The magnetic point group (symmetry) of the material might allow spontaneous polarization in addition to the linear magnetoelectric effect but this is not very common. The converse is also true: the linear ME effect is not allowed for all multiferroics. We will introduce later another term, *magnetodielectric*, to refer to materials that exhibit dielectric anomalies at magnetic phase transition temperatures or finite magnetocapacitance (change of the capacitance under applied magnetic field). Fig. 1.1 schematically describes these three classes.

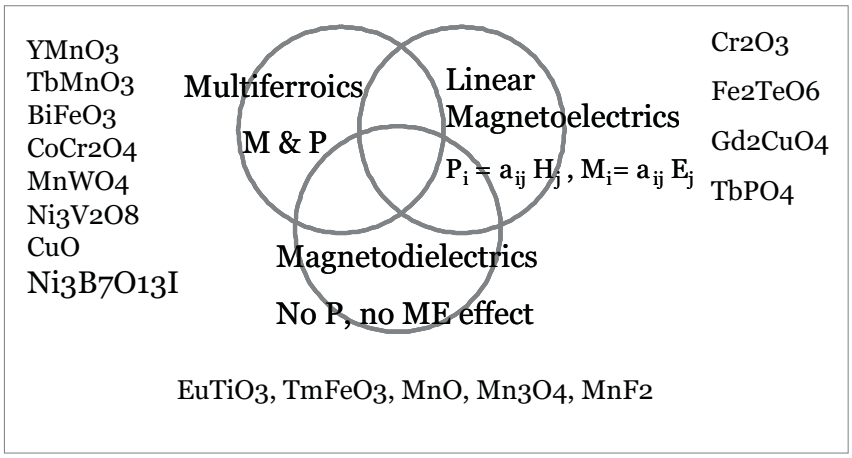

Figure 1.1: *Schematic picture of multiferroics (MF), linear magnetoelectrics (ME) and magnetodielectrics (MdE), showing the relationship between them. MC denotes magnetocapacitance.*

Fig. 1.2 shows a schematic picture describing a microscopic mechanism of magnetoelectric coupling. An applied electric field displaces the ions and induces electrical polarization. Since the applied electric field shifts one of the cations closer to the anion, while the other cation is shifted away from the anion, the ligand field of the anions experienced by the two cations is different, which creates a difference between the orbital moments of the cations, causing a net magnetization.

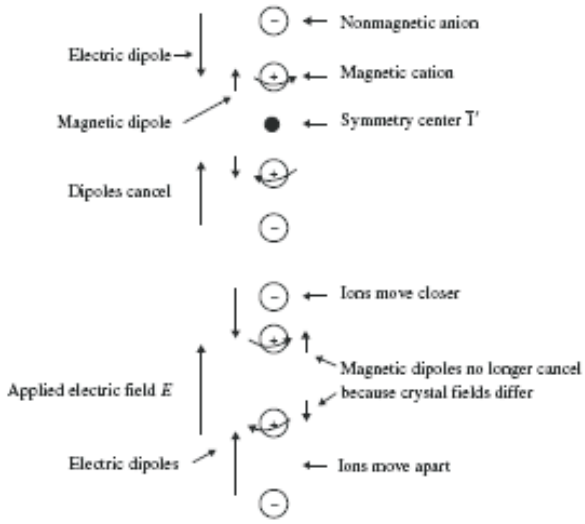

.

Figure 1.2: *"One-dimensional model of linear magnetoelectric effect in antiferromagnets" taken from [5]*

1.1.3. Examples of Multiferroics and Linear Magnetoelectrics

The revival of interest in multiferroics and linear magnetoelectrics was started partially by a paper of Huang et al. in 1997, which shows nothing but an anomaly in the dielectric constant of $YMnO_3$ at the magnetic ordering temperature [6]. This attracted attention because it was the first report that showed such an anomaly in a multiferroic material. Dielectric anomalies at the magnetic ordering temperatures had already been observed in the 1960's and 70's in a number of compounds that were not multiferroic. For example, the textbook example of linear magnetoelectrics, Cr_2O_3, was shown to present an anomaly in the dielectric constant at T_N [7]. Another example is the prototypical antiferromagnet MnF_2 (for which the linear magnetoelectric effect is not allowed), which also displays an anomaly in the dielectric constant at T_N [8].

Interest in the field of multiferroics increased further after the paper of N. Hill (now N. Spaldin) in 2000, who showed that ferroelectricity and magnetism are "contraindicated", that is, the coexistence of these two types of ordering is hampered due to the chemical incompability of the physical origin of these phenomena [9]. In conventional ferroelectrics like $BaTiO_3$, the ferroelectricity is due to the off-center displacement of the Ti ion, and this off-center displacement is only possible for a transition metal cation with an empty d-shell. However, a partially filled d-shell is necessary for magnetic ordering. Therefore, different mechanisms of ferroelectricity are necessary in order to obtain multiferroic materials. In fact, this "d^0ness" criterion had already been empirically put

forward in 1949. B.T. Matthias proposed, by using an analogy to $BaTiO_3$, to look for materials with the perovskite structure containing cations with the same noble-gas electron configuration as Ti^{4+}; it was then proved that $NaNbO_3$ is ferroelectric (Nb^{5+} having the d^0 configuration) [10].

In fact, materials with alternative mechanisms of ferroelectricity have been known for a long time. For example, the $BaMF_4$ (M = Mn, Fe, Ni, Co, Zn, Mg) family has two ferroelectric members where the ferroelectricity is not due to the off-center displacement of the M ion. The ferroelectricity of hexagonal $YMnO_3$ has been known since 1963 [11], but the origin of the ferroelectricity has recently been revised. It has been shown that the ferroelectricity is not due to the displacement of Mn ions to off-center positions as originally claimed by Yakel et al. [12], but rather is due to the relative displacements of R and O ions [13]. These hexagonal manganites constitute another example of so called "geometric ferroelectrics".

Another solution proposed to solve the problem of finding new multiferroics was to partially substitute the transition metal site of known ferroelectrics by paramagnetic ions. This gives a site containing one cation with an empty d-shell to promote ferroelectricity and one cation with a partially-filled d-shell to promote magnetism. Examples include $PbFe_{1/2}Nb_{1/2}O_3$ [14] and $PbFe_{1/2}Ti_{1/2}O_3$ [15]. However, using this approach the ferroelectric ordering is disturbed by magnetic "impurities" which can result in relaxor-like behavior or leaky samples. The coupling is expected to be low since both the magnetic and ferroelectric sublattices are diluted.

In 1978 it was already reported that antiferromagnetic ordering of the helical type breaks the inversion symmetry in Cr_2BeO_4 and induces spontaneous polarization with a value 4-6 orders of magnitude lower than that of typical ferroelectrics [16]. However, the importance of these materials was more widely understood when the response of polarization or capacitance to an external magnetic field was measured in a highly popular class of transition metal oxides known more particularly for their colossal magnetoresistance properties: the orthorhombic manganites. In 2003, Kimura et al. showed that orthorhombic $TbMnO_3$ develops electrical polarization below the transition into the spiral magnetically ordered state and displays a peak in the dielectric constant at this transition [17]. More importantly, the polarization and the dielectric constant are very susceptible to external magnetic fields; the dielectric constant changes by 10 percent under modest fields of around 4T. The strong interplay of frustrated magnetism and electrical polarization in this system attracted a lot of attention and this group of ferroelectric magnets with a spiral spin structure constitute the most popular class of multiferroics at the moment. The disadvantages of this type of multiferroics with regard to potential applications are: (1) The induced polarization is small, of the order of 0.08 $\mu C/cm^2$ compared to ~ 30 $\mu C/cm^2$ for $BaTiO_3$ [18]; (2) Due to the frustrated magnetism, the magnetic ordering and spiral ordering temperatures are usually low. Most new magnetoelectrics discovered in recent years fall into this class, including the recently reported CuO which is multiferroic which is

multiferroic below 230 K [19]. These magnetically-induced ferroelectrics belong to the class of improper ferroelectrics, for which "the electrical polarization is a secondary order parameter coupled to a magnetic order parameter" [20]. Among the spiral magnets, $DyMnO_3$ exhibits the highest magnetodielectric coupling: the dielectric constant of this material can be increased by 600 percent on applying a magnetic field [21]. This has been associated with the complex ordering of Dy spins [22].

1.1.4. Magnetodielectric Coupling

Apart from *linear magnetoelectrics* and *multiferroics*, a third term has recently been introduced to classify certain magnetic materials that possess neither spontaneous polarization nor satisfy the symmetry constraints for the linear magnetoelectric effect, but nevertheless show some kind of coupling between dielectric properties and magnetization. Throughout this thesis, we apply magnetic fields to various multiferroic or magnetoelectric samples and measure their capacitance in order to study the coupling between the electric and magnetic order parameters. It was first suggested by Lawes et al., who refer to the book by Landau and Lifshitz [23], that the term *magnetoelectric* should be reserved for special symmetries where a free energy invariant proportional to PM is allowed. They introduced "for more general couplings" the term *magnetodielectric effects* [24]. This terminology has been used for many systems, especially for magnetocapacitance measurements on systems that are not known to be linear magnetoelectrics by symmetry. Such materials display a change in dielectric constant at the magnetic ordering temperature, or show finite magnetocapacitance. This class includes $EuTiO_3$ [25], $TmFeO_3$ [26], MnF_2 [8], MnO [27], Mn_3O_4 [28], and $Tb_3Fe_5O_{12}$ [29] . We will accordingly use the term *magnetodielectric coupling* instead of *magnetoelectric coupling* for systems that do not allow the linear magnetoelectric effect by symmetry.

We can split the class of magnetodielectrics into two further subgroups. The first subgroup contains frustrated magnets, such as $Dy_2Ti_2O_7$ [30], $Tb_2Ti_2O_7$ [31] and $ZnFe_2O_4$ [32]. Although the magnetically frustrated nature of these materials does not lead to spiral ground states and ferroelectricity, their dielectric constants have been shown to couple to the magnetization and to be affected by a magnetic field. Magnetocapacitance measurements provide valuable information about the nature of the magnetic exchange interactions in these frustrated magnets. The second subgroup consists of magnets that display a large degree of magnetostriction as a common property. The materials in this class exhibit dielectric anomalies at their magnetic ordering temperatures and/or significant magnetocapacitance. MnO [27], MnF_2 [8], $TmFeO_3$ [26], $Tb_3Fe_5O_{12}$ [29] can be listed in this category.

The most prominent example of a magnetodielectric reported so far is $EuTiO_3$. $EuTiO_3$ is an incipient ferroelectric (quantum ferroelectric). This means that there is a polar phonon mode associated with the dielectric constant, which tends to zero frequency as the temperature tends to zero.

However, down to the lowest measured temperatures, no transition to the ferroelectric state takes place. It has been experimentally suggested and theoretically modeled that the frequency of this soft polar mode is coupled to the magnetic ordering of Eu spins that takes place at 5.5 K and is very susceptible to the application of a magnetic field [25, 33]. Despite the fact that this material is not ferroelectric, there seems to be direct coupling between the electric and magnetic ordering. Because the polar mode to which the magnetic ordering couples is soft, the magnetodielectric coupling and thus magnetocapacitance is large: the dielectric constant of the material can be changed by 6 percent at 2K. After giving an outline of various multiferroics, magnetoelectrics and magnetodielectrics, it is time to mention the magnitudes of magnetodielectric coupling in these systems. As we mentioned, the largest magnetocapacitance was measured in multiferroic $DyMnO_3$ [21]. In general, when the magnetic ordering breaks the inversion symmetry, the coupling and the measured magnetocapacitance are expected to be large. This is not always the case; there are also variations within the family of magnetically induced ferroelectrics. Nonetheless, the class of magnetically induced ferroelectrics is the most promising class among the multiferroics. Within the linear magnetoelectric materials, the coupling is smaller than the magnetically induced ferroelectrics. That shows that even though the symmetry of the materials allows for the natural coupling between magnetic field and electrical polarization, this coupling does not have to be large. Therefore, coupling mechanism is important to determine the magnitude of coupling, not the fulfillment of the symmetry conditions. Another distinct example that displays large coupling is $EuTiO_3$ which we mention just above. A soft phonon coupled to magnetic ordering is the key factor to obtain the large coupling in this material.

1.1.5. Two-phase Systems

Apart from single-phase approaches to obtain coupling between magnetism and ferroelectricity, two-phase systems have also been utilized. The coupling now takes place indirectly via strain. One of the two phases should be piezomagnetic or magnetostrictive while the other should be piezoelectric or electrostrictive. Usually, ferroelectrics in combination with ferromagnets are used for this purpose. These systems can be put into contact in the form of laminates, composites or epitaxial layers of thin films [4]. The coupling coefficients achieved are many orders of magnitude larger than in single-phase multiferroics.

1.2. Aspects of the Current Theoretical Understanding of Magnetoelectric Coupling

Having listed the different types of materials that show coupling between electrical and magnetic orderings, we can summarize some aspects of our current theoretical understanding in the field.

To model the magneto(di)electric coupling, that is, magnetocapacitance and anomalies in the dielectric constant due to magnetic ordering, the Landau theory of phase transitions is extensively used. Landau theory is a symmetry-based analysis of equilibrium behavior near a phase transition [34]. Landau theory characterizes the phase transition in terms of an "order parameter", which is zero in the high-temperature disordered state, and becomes finite continuously or discontinuously as the symmetry is lowered. The free energy is then expanded as a power series in this order parameter. Only terms which are invariant with respect to all symmetry operations are included. The equilibrium state is found by minimizing the free energy with respect to the order parameter. Other thermodynamic properties can be computed by relevant differentiation [34]. In the field of multiferroics, Landau modelling has mainly been used to explain the magnetocapacitance properties of various samples [35–37].

Smolenskii defined [2] and Kimura et al. [35] used the order parameters for ferroelectric and magnetic subsystems and added a term $\gamma \mathrm{P}^2\mathrm{M}^2$ to account for the magnetoelectric coupling. The polarization, P, is the order parameter for the ferroelectric subsystem, and the magnetization, M, is the order parameter for the magnetic subsystem, while γ is the magnetoelectric coupling coefficient.

A crystallographic space group defines the symmetry elements of a system including the magnetic spins. The terms in the Landau free energy expression must be invariant upon the application of all symmetry operators of the group, including the time reversal operator, T. Ferroelectrics have no inversion symmetry operator, i. Linear magnetoelectrics contain bilinear terms such as EH, and the multiplication of these terms are invariant under $T \times i$. Biquadratic terms are invariant to all symmetry operators and thus they are always invariant. Spatial inversion reverses the sign of the electrical polarization while magnetization is unaffected, whereas the time-reversal operator reverses the sign of the spins -and hence the magnetization- while the polarization is unaffected.

$$\phi = \phi_0 + \alpha P^2 + \frac{\beta}{2} P^4 - PE + \alpha' M^2 + \frac{\beta'}{2} M^4 - MH + \gamma P^2 M^2 \tag{1.6}$$

Here, P and M are the order parameters for the polarization and magnetization, respectively, and α, β, α', β' and γ are coupling coefficients. The term representing magnetoelectric coupling, $\mathrm{P}^2\mathrm{M}^2$, is always allowed regardless of symmetry. Kimura et al. used this free energy expression to calculate the effect of magnetic ordering on the dielectric susceptibility, χ=ε+1. The dielectric constant can

be derived using $\chi^{-1}=\frac{d^2\phi}{dP^2}$. It can be shown that the effect of magnetic ordering on the dielectric constant will be proportional to $\Delta\varepsilon \sim M^2$ [35].

The dielectric constant is related to the phonon frequencies through the Lyddane-Sachs-Teller (LST) relation

$$\omega_L^2 = \frac{\varepsilon_0}{\varepsilon_\infty}\omega_T^2 \tag{1.7}$$

In this equation ω_L and ω_T are the long wavelength longitudinal and transverse optical-phonon mode frequencies, respectively. ε_0 is the static dielectric constant, that is, the dielectric constant at zero frequency, and ε_∞ is the optical dielectric constant.

Because the dielectric constant is related to the optical phonon modes, the effect of the magnetic ordering on the dielectric constant may be proven by measuring the low-lying phonon modes through the magnetic ordering temperature (see, for example, [38]).

The ferroelectricity induced by spiral magnetic ordering can be explained by the spin-current model [39] or the Dzyaloshinskii-Moriya interaction [40]. According to the latter model, the electrical polarization is expressed by

$$P = \sum_{\mathrm{i,j}} A e_{i,j} \times (S_i \times S_j) \tag{1.8}$$

where $e_{i,j}$ denotes the unit vector connecting the spins S_i and S_j, and A is the constant representing the exchange interaction and the spin-orbit interaction. This model concludes that any helimagnet with a transverse-spiral spin arrangement (that is, when the magnetic propagation wave vector **k** is parallel to the spin-spiral plane) may show ferroelectricity.

1.3. Motivation of this thesis

This thesis aims to understand the nature of magneto(di)electric coupling. As explained previously, there are several signatures of magneto(di)electric coupling: an anomaly in the temperature dependence of the dielectric constant at the magnetic ordering temperature, a finite magnetic-field dependence of the dielectric constant known as magnetocapacitance, and a finite magnetic-field dependence of the electrical polarization. It is also possible to perform the converse experiments, such as electric-field induced magnetization, but these effects are more difficult to measure. An overview of magnetoelectric measurements can be found in [3] and [41].

We have used structural, magneto(capacitance) and pyroelectric current measurements to study the magnetodielectric coupling in two families of compounds. The first family is the multiferroic hexagonal manganites. The second is the orthorhombic polar $R_2Cu_2O_5$ materials, which exhibit

complex magnetic phase diagrams. The fundamental questions we try to address in the course of this study are:

- What can we learn from the dielectric anomalies at the magnetic ordering temperature?
- Can we model the magnetocapacitance behavior?
- How does magnetoelectric coupling change with the development of magnetic order parameters?
- What type of spin orderings favor large magnetodielectric coupling?
- How can extrinsic and intrinsic contributions to the dielectric constant be differentiated?

Bibliography

[1] H. Schmid, Ferroelectrics, 162, 317, (1994).

[2] G. A. Smolenskii and I. E. Chupis, Sov. Phys. Usp. 25, 475 (1982).

[3] M. Fiebig, J.Phys. D: Appl. Phys. 38, R123, (2005).

[4] W. Eerenstein, N. D. Mathur, and J.F. Scott, Nature, 442, 759, (2006).

[5] Robert E. Newnham, Properties of Materials, Oxford University Press, (2005).

[6] Z. J. Huang, Y. Cao, Y. Y. Sun, Y. Y. Xue, and C. W. Chu, Phys. Rev. B, 56, 2623 (1997).

[7] H. B. Lal, R. Srivastava, and K. G. Srivastava, Phys. Rev., 154, (1967).

[8] M. S. Seehra and R. E. Helmick, J. Appl Phys. 55, 2330, (1984).

[9] N. Hill, Journal of Physical Chemistry B, 104, 6694, (2000).

[10] B. T. Matthias, Phys. Rev. 75, 1771 (1949).

[11] E. F. Bertaut, P. Fang, and P. Forrat, C. R. Hebd. Seances Acad. Sci. 256, 1958 (1963).

[12] H. L. Yakel, W. C. Koehler, E. F. Bertaut, and E. F. Forrat, Acta Crystallogr., 16, 957, (1963).

[13] B. B. van Aken, T. T. M. Palstra, A. Filippetti, and N. A. Spaldin, Nature Materials, 3, 164, (2004).

[14] Y. Yang, J. M. Liu, H. B. Huang, W. Q. Zou, P. Bao, and Z. G. Liu, Phys. Rev. B 70, 132101 (2004).

[15] V.R. Palkar and S.K. Malik, Solid State Commun., 134, 783, (2005).

[16] R. E. Newnham, J. J. Kramer, W.A. Schulze, and L. E. Cross, J. Appl. Phys. 49, 6088, (1978).

[17] T. Kimura, T. Goto, H. Shintani, K. Ishizaka, T. Arima, Y. Tokura, Nature, 426, 55, (2003).

[18] N. A. Spaldin, Physics of Ferroelectrics: A Modern Perspective, Book Series: Topics in Applied Physics, 105, pp. 175-217, (2007).

[19] T. Kimura, Y. Sekio, H. Nakamura, T. Siegrist, and A. P. Ramirez, Nature Materials, 7, 291, (2008).

[20] K. M. Rabe, P. Ghosez, Physics of Ferroelectrics: A Modern Perspective, Book Series: Topics in Applied Physics, 105, pp. 117-174, (2007).

[21] T. Goto, T. Kimura, G. Lawes, A. P. Ramirez, and Y. Tokura, Phys. Rev. Lett. 92, 257201 (2004).

[22] O. Prokhnenko, R. Feyerherm, E. Dudzik, S. Landsgesell, N. Aliouane, L. C. Chapon, and D. N. Argyriou, Phys. Rev. Lett. 98, 057206 (2007).

[23] L.D. Landau, E.M. Lifshitz, and L.P. Pitaevskii, Electrodynamics of Continuous Media, Pergamon, New York, (1984).

[24] G. Lawes, A. P. Ramirez, C. M. Varma, and M. A. Subramanian, Phys. Rev. Lett. 91, 257208, (2003).

[25] T. Katsufuji and H. Takagi, Phys. Rev.B, 64, 054415, (2001).

[26] R. Muralidharan, T. -H. Jang, C. -H. Yang, Y. H. Jeong, and T. Y. Koo, Appl. Phys. Lett. 90, 012506, (2007).

[27] M. S. Seehra and R. E. Helmick, Phys. Rev.B, 24, 5068, (1981).

[28] R. Tackett, G. Lawes, B. C. Melot, M. Grossman, E. S. Toberer, and R. Seshadri, Phys. Rev.B, 76, 024409, (2007).

[29] N. Hur, S. Park, S. Guha, A. Borissov, V. Kiryukhin and S. -W. Cheong, Appl. Phys. Lett. 87, 042901, (2005).

[30] M. Saito, R. Higashinaka, and Y. Maeno, Phys. Rev.B, 72, 144422, (2005).

[31] T. Katsufuji and H. Takagi, Phys. Rev.B, 69, 064422, (2004).

[32] T. Suzuki, Y. Aikawa and T. Katsufuji, J. Phys. Soc. Japan, 74, 863, (2005).

[33] C. J. Fennie and K. M. Rabe, Phys. Rev. Lett. 97, 267602, (2006).

[34] P. Chandra and P. B. Littlewood, Physics of Ferroelectrics: A Modern Perspective, Book Series: Topics in Applied Physics, 105, pp. 69-115, (2007).

[35] T. Kimura, S. Kawamoto, I. Yamada, M. Azuma, M. Takano, and Y. Tokura, Phys. Rev.B, 67, 180401, (2003).

[36] A. A. Nugroho, N. Bellido, U. Adem, G. Nenert, Ch. Simon, M. O. Tija, M. Mostovoy, and T. T. M. Palstra, Phys. Rev. B, 75, 174435, (2007).

[37] N. Bellido, Ch. Simon, and A. Maignan, Phys. Rev.B, 77, 054430, (2008).

[38] A. P. Litvinchuk, M. N. Iliev, V. N. Popov, and M. M. Gospodinov, J. Phys.: Condens. Matter 16, 809 (2004).

[39] H. Katsura, N. Nagaosa, and A. V. Balatsky, Phys. Rev. Lett. 95, 057205 (2005).

[40] M. Mostovoy, Phys. Rev. Lett. 96, 067601 (2006).

[41] T. H. O'Dell, Magnetoelectric Interaction Phenomena in Crystals, edited by A.J. Freeman and H. Schmid, Gordon and Breach Science Publishers, 1975.

CHAPTER 2

Experimental Techniques

This thesis consists of structural, magnetic, capacitance, pyroelectric current and ferroelectricity measurements on a number of multiferroic and magnetodielectric compounds. In this chapter, the experimental methods and instruments used for these measurements will be described.

2.1. Synthesis

Single crystals of the materials studied in this thesis were grown using a floating zone technique. In order to prepare the polycrystalline samples necessary for crystal growth, conventional solid state synthesis was used. Because the rare-earth sesquioxide precursors used are hydroscopic, such as Y_2O_3, Yb_2O_3, and Er_2O_3, they were dried prior to the grinding step. Grinding was done in an acetone medium in order to improve the homogeneity. The powders were then mixed in stoichiometric ratios and sintered. A rod-shaped rubber mold was then filled with finely ground powder of the resulting compound and placed in a quartz tube. The tube was evacuated using a vacuum pump for densification. The rod was then pressed using a hydrostatic press at a pressure of 600 bars. Usually, this pressed rod was resintered for further densification.

The sintered rod was placed in a Crystal Systems Inc. floating zone furnace (Model FZ-T-10000-H-VI-VP). This model has four mirrors which allow operation up to 1900 °C. The principle of this technique is to melt a small section of a feed rod using infrared radiation that has been focused by means of the mirrors. The molten (floating) zone is then translated along the sample length by

moving the sample with respect to the radiation focus. The crystal is grown on the solidifying end of the floating zone, on top of the seed, which should be a material with a similar crystal structure to the feed rod. The advantages of this growth method are: (1) large crystals can be obtained; (2) no crucible is used, avoiding contamination from the crucible.

The actual growth of the crystals was kindly undertaken by Agung A. Nugroho (all the hexagonal manganites including $Yb_{0.5}Y_{0.5}MnO_3$) and N. Mufti ($Y_2Cu_2O_5$) from our group, while the rods were prepared by the author (undoped hexagonal manganites), Agung A. Nugroho (Ga substituted hexagonal manganites), and a Masters student Arramel ($Y_2Cu_2O_5$). Further details of the travelling floating zone technique can be found in the chapter on cuprates.

2.2. X-ray Diffraction Experiments

2.2.1. X-ray Powder Diffraction (XRPD)

XRPD was used both for phase analysis and crystal structure refinement. A Bruker D8 difractometer operating in Bragg-Brentano geometry was used. This diffractometer utilizes an energy dispersive detector (SolX). The standard powder diffraction software PowderCell (W. Kraus and G. Nolze, J. Appl. Cryst. 29, 301, (1996)) was used for rapid phase analysis. To obtain data suitable for crystal structure refinements, scans were typically performed with a step size of 0.02 °C and 10 seconds exposure at each step. The measured diffraction patterns were compared to those of existing structural models in the ICSD Database. The GSAS (General Structure Analysis System) software package (A. C. Larson and R. B. Von Dreele, "General Structure Analysis System (GSAS)", Los Alamos National Laboratory Report LAUR 86-748, (2000)) was used for Rietveld refinement of the crystal structures. This involves adjusting parameters such as the atomic positions, site occupancies and displacement parameters in order to optimize the fit of the diffraction pattern calculated from the structural model to the measured data.

2.2.2. Single Crystal X-ray Diffraction (SXD)

Compared to XRPD, SXD is generally a more powerful tool for the solution of crystal structures and symmetry due to the independent measurement of all Bragg reflections; however, XRPD has better angular resolution which enables more accurate determination of the lattice parameters. The SXD experiments were performed using a Bruker AXS APEX single crystal diffractometer operating with monochromatized Mo-Kα radiation equipped with a CCD camera. The SHELXL software package was used for structural refinement (G. M. Sheldrick, SHELXL-97, Program for the Refinement of the Crystal Structures, University of Göttingen, Germany, (1997)).

The single crystals investigated in this thesis were oriented for various physical measurements using an Enraf-Nonius CAD4 single crystal diffractometer.

2.3. Magnetization Measurements

Magnetization measurements were performed using a Quantum Design MPMS7. The MPMS is a very sensitive magnetometer due to the utilization of a liquid-helium-cooled SQUID (superconducting quantum interference device) to measure changes in the magnetic flux (converted to current) that occur as the sample moves through the superconducting detection coil. Our Quantum Design MPMS allows the magnetic properties of materials to be measured over a temperature range of 1.8 to 400 K, at magnetic fields of between -7 and +7 T. It is possible to measure materials in powder, crystal or pellet form.

The samples were placed in gelatin capsules (which have a small diamagnetic signal), contained in a plastic straw that was attached to the MPMS sample probe. For samples with a large magnetic moment and sharp magnetic transitions such as $ErMnO_3$, GE varnish was used to glue the sample to the capsule in order avoid movement of the sample due to magnetic torque.

Almost all of the magnetic measurements were performed after zero-field cooling (ZFC), which involves cooling the sample through its magnetic ordering temperature without applying a magnetic field, and then applying a field at the lowest temperature and measuring the magnetization of the sample on heating. The reason to perform mainly ZFC measurements is the fact that the samples in this thesis are ordinary antiferromagnets with no ferromagnetic component in the ground state.

2.4. Capacitance Measurements

Our aim in this thesis was to study the coupling between electrical polarization and magnetic ordering. This can be done by measuring the change in electrical polarization upon the application of a magnetic field, or alternatively and indirectly by measuring the change of the capacitance upon magnetic ordering or upon the application of a magnetic field.

The dielectric susceptibility, χ, of a material is related to the electrical polarization by dP/dE = $\varepsilon_0.\chi$. Thus, the slope of a plot of P vs E is proportional to the dielectric constant of the material, via $\varepsilon = 1 + \chi$, which is proportional to capacitance.

The capacitance of a dielectric in parallel-plate geometry is defined as $C = \varepsilon_0 \varepsilon \frac{A}{d}$, where ε_0 is the permittivity of free space, ε is the dielectric constant, A is the area of the contacts, and d is the thickness of the sample. The dielectric constant is unitless.

A home-built probe was used to measure the capacitance of the samples in a commercial Physical

Properties Measurement System (PPMS). Although this setup is designed to perform both four-point and two-point capacitance measurements, two-point measurements were generally used. Fig. 2.1 shows a picture of the probe. The flange contains four triax connectors; their shields are not isolated from each other. The triax connectors are connected to stainless steel coaxial wires below the flange. The inner parts of the coaxial wires are connected at the bottom of the probe to the sample holder. The shields of the coaxial wires are connected to a copper block at the bottom of the sample holder. This copper block is kept at the same voltage potential as the flange.

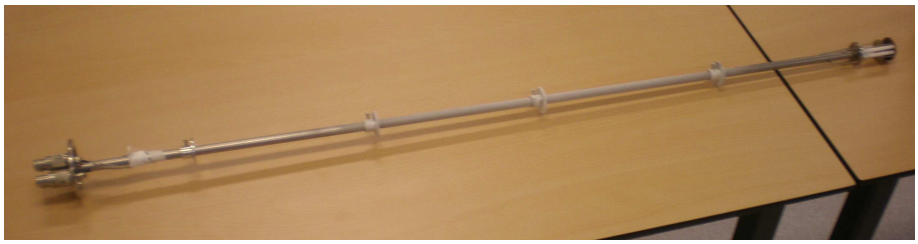

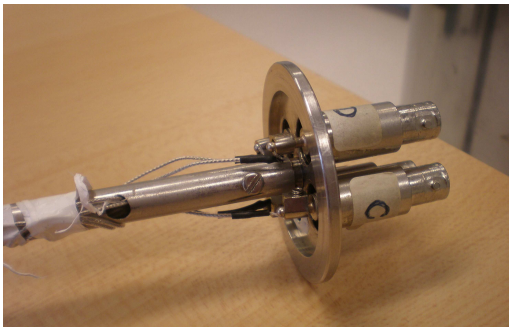

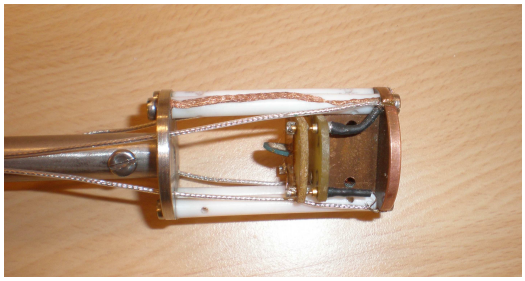

Figure 2.1: *Different views of the dielectric probe used to measure the capacitance of the samples in the PPMS. At the top, the whole probe is shown. At the bottom left, a closer view of the connectors is provided and at the bottom right, a sample attached to the sample holder is shown.*

In order to form a parallel plate capacitor, electrodes were formed on the largest surfaces of the samples, usually by using two-component Ag epoxy. The Ag epoxy was cured. In other cases contacts were made by Au sputtering using an Edwards Sputter Coater. The sample was polished prior to the application of contacts in order to obtain a smooth surface and better sample-contact interface. For the pellets, care was taken at the pressing stage to obtain a smooth surface.

Capacitance measurements were performed using a precision capacitance bridge AH 2500A at a fixed frequency of 1kHz, and using an Agilent LCR Meter for frequencies from 20 Hz-1 MHz.

The PPMS is a cryogenic platform that is used to carry out temperature (between 1.8 K and 375 K) and magnetic field (between -9 T and 9 T) dependent physical measurements. It allows the

conduction of transport measurements such as resistivity, Hall effect, Seebeck effect, magnetoresistance and capacitance measurements. By means of a sample rotator, it is possible to measure the anisotropic properties of single crystal samples. The measurements were controlled using LabView and Visual Basic programs.

2.5. Pyroelectric current measurements

A commonly used method of measuring spontaneous polarization is to perform so-called pyroelectric current measurements. All materials that exhibit spontaneous polarization are also pyroelectric; the electrical polarization changes when the temperature is changed in zero electric field. A typical pyroelectric current measurement first involves ”poling” the sample by cooling in an applied electric field through the transition at which the sample becomes pyroelectric or polar. When the temperature at which the measurement will be started is reached, the electric field is removed and the material is then heated at a constant rate. At the transition temperature a maximum in the pyroelectric current is expected, which can be then integrated in time to obtain the electrical polarization. A Keithley 238 electrometer was used to pole the samples and a Keithley 6517A electrometer was used to measure the pyroelectric current.

The pyroelectric current measurements shown in this thesis were actually performed in an unconventional manner. The hexagonal manganites have high ferroelectric transition temperatures (close to 1000 K), and it is thus very difficult to measure the transition temperature by pyroelectric current measurements. Furthermore, such measurements do not fall under the scope of this thesis. The orthorhombic cuprates measured in this thesis are predicted to be linear magnetoelectrics (see the chapter on cuprates) and the linear magnetoelectric effect was thus examined by performing pyroelectricity measurements under magnetic fields. These measurements involved heating the samples to above their magnetic ordering temperature. Then, both magnetic and electric fields were applied simultaneously in order to achieve a single-domain state, and the sample was cooled down to the lowest practically achievable temperature, usually to 5 K. This cooling procedure is known as ”magnetoelectric annealing”. At 5 K, only the electric field was removed and the top and bottom electrodes were shorted in order to eliminate the surface charges. Then, the sample was heated at a constant rate -typically 4 K per min- while the magnetic field was kept constant. If the sample is magnetoelectric, electrical polarization is induced upon the application of the magnetic field. Above the magnetic ordering temperature, the polarization should vanish.

2.6. Ferroelectricity Measurements

Although no results from ferroelectricity measurements have been included in the thesis, most of the samples were examined for ferroelectricity using a Radiant Precision Workstation ferroelectric tester. A maximum of 100 Volts can be applied to the sample internally; however, for bulk samples this is usually insufficient because the typical thickness of the crystal pieces measured is around 1 mm, while the electrical coercive field of the materials is larger than 1 kV/cm. Therefore, at room temperature a high-voltage amplifier was used together with an interface to increase the maximum voltage externally to 4 kV. These high voltage tests were carried out in silicone oil for insulation purposes. Attempts were made to measure P-E loops for $YbMnO_3$ using high electrical fields at room temperature, but because the sample was a bad insulator, lossy behavior was observed in the P-E loops.

2.7. High Magnetic Field Measurements

High magnetic field measurements were performed at the Grenoble High Magnetic Field Laboratory (LCMI) and at the Nijmegen High Magnetic Field Laboratory (NHFML).

The magnetization of $ErMnO_3$ samples was measured using an extraction technique at LCMI in fields of up to 28 Tesla and temperatures from 2-80 K. The sample was glued to the ”bore” using Apiezon grease to avoid possible movement. Magnetocapacitance measurements were performed both at LCMI (fields of up to 28 T) and at NHMFL (up to 30 T). In order to measure capacitance, a probe similar to that used in the laboratory experiments was designed in collaboration with local contacts. The probe was placed in a flow cryostat located at the center of the magnet installation. At LCMI an Agilent 4284A capacitance bridge was used, whereas at NHMFL an Andeen-Hagerling AH 2700A capacitance bridge was employed. There are certain experimental difficulties involved in measuring capacitance at high magnetic field facilities. Firstly, controlling the temperature is more problematical compared to using a PPMS for the same purpose, because one needs to take into account the magnetoresistance of the thermometer material. Therefore, a capacitive thermometer was employed during the field scans after stabilizing the temperature with a resistive thermometer (CERNOX). Secondly, the impedance contribution from the long BNC cables connecting the sample to the capacitance bridge/LCR meter is significant. Longer wires are necessary because the measument setup has to be far away from the magnet during operation. At LCMI a standard cable-length correction operation was performed for the LCR Meter. At NHFML it was possible to keep the cable length shorter. For better signal to noise ratio, 10 kHz was chosen as the measurement frequency both at LCMI and NHFML.

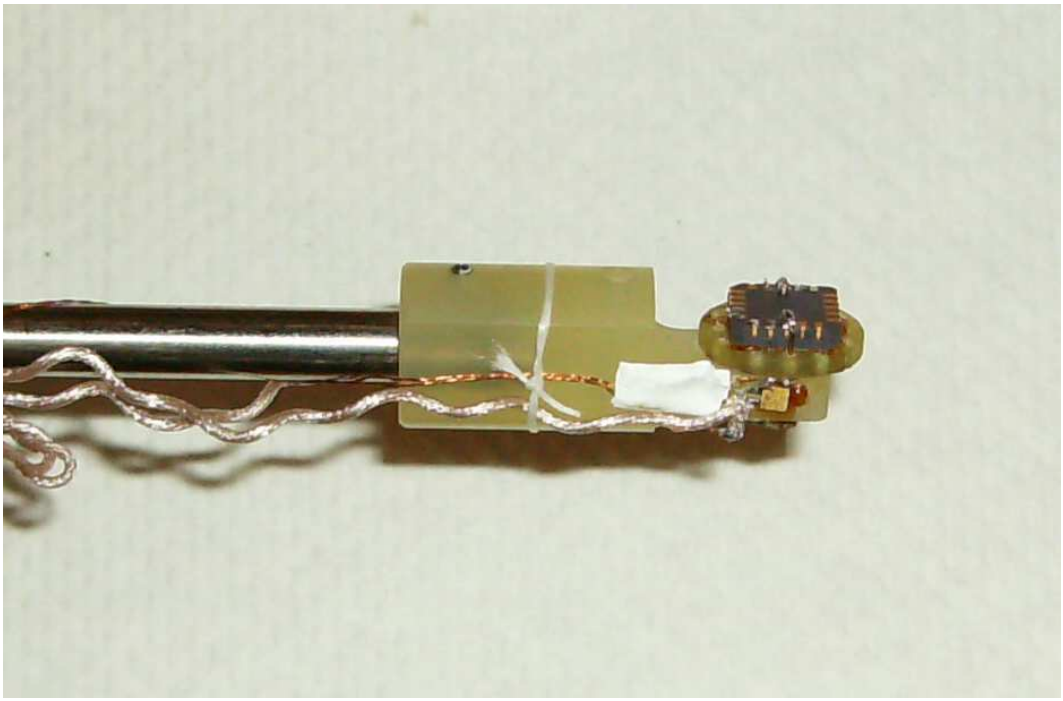

Figure 2.2: *A view of the sample holder section of the dielectric probe used at NHFML.*

CHAPTER 3

Magnetodielectric Coupling in $R_2Cu_2O_5$

3.1. Introduction

There is at the moment enormous interest in multiferroic and magnetoelectric materials [1]. Ferroelectricity and magnetism seldom coexist, due to the fact that many ferroelectrics need atoms with an empty d-shell for off-centering to occur, whereas magnetism requires partially filled d-shells [2]. Nevertheless, mechanisms for obtaining ferroelectricity that do not involve off-center displacements of transition metal cations have been discovered. Examples are geometric ferroelectrics such as $BaMnF_4$ [3] and hexagonal $RMnO_3$ [4], electronic ferroelectricity [5], and magnetically induced ferroelectricity [6]. The last discovery has become the focus of research on multiferroics, since large coupling is observed between electric and magnetic ordering. Despite the increase in the variety of mechanisms and materials in the study of multiferroic materials, more systems must be studied to understand the microscopic mechanisms involved in magnetoelectric coupling.

Magnetic insulators with a polar space group have the potential to be multiferroic. Not all polar materials are ferroelectric, because this requires that the polarization must be switchable. Therefore, a simple approach for obtaining new multiferroics involves selecting polar magnetic insulators and checking for the presence of ferroelectricity. This approach, however, is rather too exploratory, since there are many pyroelectric materials that are not ferroelectric. For example, among the polar $BaMF_4$ family (M is Ni, Co, Mg, Zn, Fe, Mn), the first four have been proved to be ferroelectric, that is, switchable spontaneous polarization has been demonstrated. However, ferroelectricity has not been

proved in the Mn and Fe compounds, due in part to their appreciable electric conductivities, which make the measurements difficult to perform, but also due to the larger ionic sizes of Mn and Fe that hinder the ionic displacements responsible for ferroelectricity [3, 7, 8].

One can add another restriction to this exploratory approach: one should look for a polar magnetic insulator that allows the linear magnetoelectric effect by symmetry. This might contribute to larger magnetoelectric coupling compared to that in an ordinary polar magnet. The symmetry of the material in the magnetically ordered state determines whether the linear magnetoelectric effect is allowed.

Here, we present evidence for magneto(di)electric coupling in a polar antiferromagnet $Y_2Cu_2O_5$. There were three main reasons to choose this compound: (1) the fact that it is a potential multiferroic; (2) we have carried out symmetry analysis and concluded that in the magnetic ground state, magnetoelectric coupling is allowed, that is, the symmetry of the magnetic ground state allows the linear magnetoelectric effect; (3) it has been established from measurements on many multiferroics and magnetodielectric materials that magnetocapacitance measurements are sometimes able to probe the presence and nature of the magnetic phase transitions even better than magnetization measurements [9–11]. Taking into account that $Y_2Cu_2O_5$ shows two metamagnetic transitions, it is interesting to study these transitions by measuring the dielectric constant.

$Y_2Cu_2O_5$ is the so-called "blue phase" of the family of cuprates that exists in the ternary R_2O_3-CuO-BaO phase diagram, from where the high Tc superconductor $YBa_2Cu_3O_x$ originates .$Y_2Cu_2O_5$ is encountered as a secondary phase during the synthesis of $YBa_2Cu_3O_x$ [12]. The original interest in $Y_2Cu_2O_5$ was to understand the effect of the ordering of rare-earth spins on that of Cu spins, which is useful to understand the exchange interactions in superconducting $YBa_2Cu_3O_x$ [13].

$R_2Cu_2O_5$ compounds crystallize in the polar orthorhombic space group $Pna2_1$ for R having an ionic radius smaller than Gd, as well as for Y, Sc and In. The crystal structure, together with a more detailed view of one Cu chain, is depicted in Fig. 3.1. There are 2 different sites for both Cu and R ions in the unit cell, with very similar coordination. Cu ions have a distorted square planar coordination; there are four O ions within a distance of 1.9 Å, and a fifth at a distance of 2.7 Å. The Cu1 and Cu2 ions are coupled to form dimers, which form Cu_2O_5 zigzag chains along the *a* axis. The Cu ions in adjacent chains are also connected along the *b* axis to form *ab* pseudoplanes. These pseudoplanes are separated by the rare-earth ions, which have a distorted octahedral coordination and are connected in three dimensions [14].

Magnetic ordering in $R_2Cu_2O_5$ systems is complicated, with several exchange interactions being present. The magnetic ordering has been studied by neutron diffraction by Garcia-Munoz *et al.* [15]. At 1.5 K, the magnetic structures are commensurate with the propagation vector **k** = [0, 0, 0] for Y, Er and Tm, **k** = [0, 1/2, 0] for Ho and **k** = [0, 1/2, 1/2] for Yb. The Cu^{2+} moments

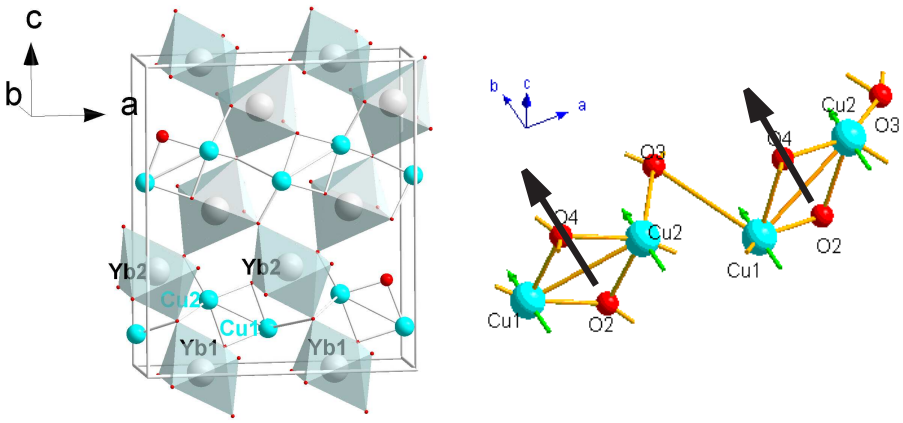

Figure 3.1: *Crystal structure of $Yb_2Cu_2O_5$ is shown on the left. On the right, copper chain along a is shown. The black lines denote the S=1 Cu dimer spins oriented along b axis.*

are aligned ferromagnetically along the [010] direction in the *ab* pseudo-planes formed by the Cu chains, and adjacent pseudoplanes are antiferromagnetically (AF) coupled along the c axis. For all the materials with magnetic R cations except Yb, the R spins order simultaneously with the Cu spins. For members of the family containing non-magnetic R cations, the Curie-Weiss temperatures are positive, suggesting that the dominant interactions are ferromagnetic [16]. This is in contrast to the negative Weiss temperatures observed for the cuprates with magnetic rare earths [15]. Among the non-magnetic rare-earth cuprates, the magnetic ordering temperature T_N increases with increasing a/c ratio, because the decrease of the c lattice parameter increases the strength of the AF exchange [16]. Metamagnetic transitions have been observed in $R_2Cu_2O_5$, first reported by Cheong *et al.* [12] for a single crystal of $Y_2Cu_2O_5$. In $Y_2Cu_2O_5$ these transitions occur when the magnetic field is applied parallel to the easy-axis, b. At 4.2 K, the first field-induced transition occurs at a critical field of H_{C1} = 2.8 T. It is marked by a step-like increase in magnetization, amounting to one third of the saturation magnetization. A second step is observed at H_{C2} = 4.71 T, and the magnetization reaches saturation at 7.3 T [17]. A phase diagram has been constructed from anomalies in the magnetization measurements [12]. Other members of the family, except for R = Tb and Tm, have various numbers of metamagnetic transitions; the highest number of transitions (five transitions below 12 T) is found in $Yb_2Cu_2O_5$ [18]. However, due to the lack of large single crystals and the high critical fields, neutron diffraction studies to determine the magnetic structures of the field induced phases have only been carried out for $Y_2Cu_2O_5$ [17].

In this study, we use magnetocapacitance measurements to show that magnetodielectric coupling occurs in $Y_2Cu_2O_5$ single crystals.

3.2. $Y_2Cu_2O_5$ Single Crystals

3.2.1. Crystal Growth and Experimental Methods

Polycrystalline $Y_2Cu_2O_5$ was synthesized from Y_2O_3 and CuO precursors using standard solid state reaction. The precursors were dried and sintered at 1000^oC for 12 hours. After regrinding, the powder was pelletized and sintered at the same temperature. This grinding-sintering cycle was repeated until a pure compound was obtained. For the synthesis of the single crystal, the travelling solvent floating zone technique (TSFZ) was used, following the method of Nishimura *et al.* [19]. Both flux growth and TSFZ growth techniques have been reported for the preparation of $R_2Cu_2O_5$ crystals [18–20]. Both techniques are suitable for compounds that melt incongruently [21], which is the case for $R_2Cu_2O_5$. Fig. 3.2 shows the phase diagram of from ref. Y_2O_3 [22], showing the incongruent character of the phase diagram.

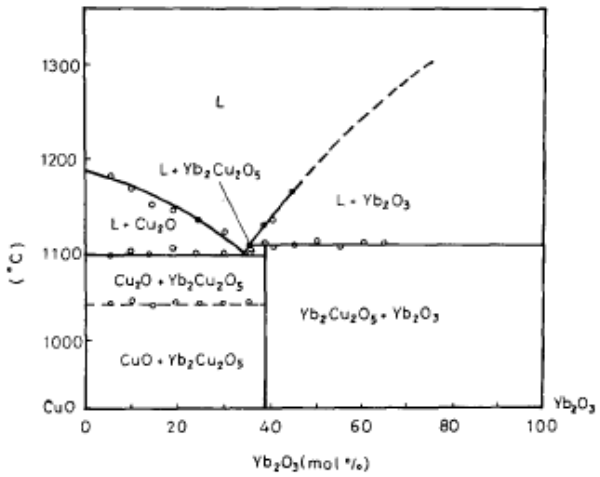

Figure 3.2: *Binary phase diagram for $Yb_2Cu_2O_5$ from [22].*

In the TSFZ technique, a so-called 'solution rod' is introduced between the seed and feed rods so that a liquid is formed at lower temperatures. Then, very slow growth rates are employed in order to give enough time for the mass transport through the liquid. The ratio of Y_2O_3:CuO in our solution rod was 4.6:95.4 [19]. Crystal growth took place only at a slow growth rate of 0.1 mm/h. An atmosphere of 60% Ar : 40% O_2 was used. The growth process lasted for a total of 3 weeks. The upper and lower shafts were both rotated at 20 rpm. The single crystal obtained was 15mm long and 6mm in diameter. We also attempted to grow crystals by the flux method reported in Refs. [18] and [20]. These attempts were unsuccessful, yielding only very small crystallites.

The crystallinity and lattice parameters of our $Y_2Cu_2O_5$ single crystal were checked using powder X-ray diffraction on a crushed single crystal. The lattice parameters, a = 10.8117(23) Å, b =

3.4993(7) Å, and c = 12.4756(26) Å, are slightly different to those in previous reports [14]. Powder diffraction on a crushed piece of the single crystal (see Fig. 3.3) showed that the sample contained a very small amount of CuO impurity, possibly due to contamination from the solution rod. Nevertheless, a good fit was obtained between the observed and calculated diffraction patterns. However, the corresponding fit using single crystal diffraction data was rather poor and the refined atomic parameters had large standard deviations. This was largely attributable to the broadness of the reflections, suggesting that the crystal quality was not perfect.

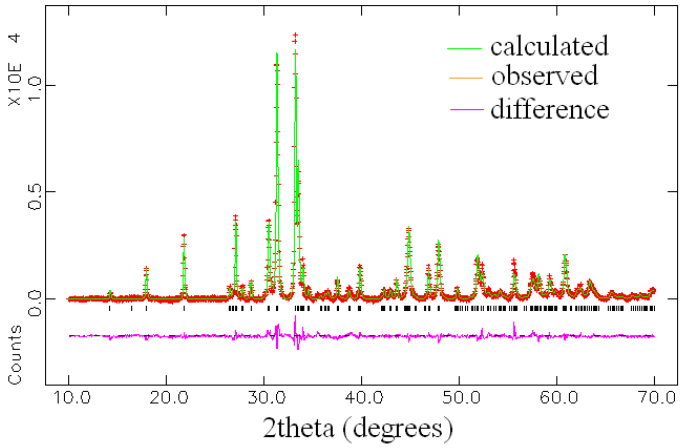

Figure 3.3: *Refinement results for $Y_2Cu_2O_5$ crushed single crystal.*

The magnetization M(T,H) of the samples was measured using a SQUID magnetometer (MPMS7 Quantum Design) in applied fields of up to 7 T. The capacitance of the samples was measured using a commercial system (PPMS Quantum Design) with a home-made insert and an Andeen-Hagerling 2500A capacitance bridge operating at a fixed measurement frequency of 1 kHz; the frequency could be varied using an Agilent 4284A LCR meter. A maximum magnetic field of 9 T was applied. Electrical contacts were made in parallel plate capacitor geometry using Ag epoxy, which was cured at 120°C for 15 minutes. The typical thickness of the crystals was 1 mm, with a surface area of 2 by 3 mm. We checked for the presence of a linear magnetoelectric effect by performing pyroelectricity measurements under applied magnetic fields, as described in section 2.5 of this thesis.

3.2.2. Magnetic Properties

We first present the results of our magnetization measurements. In Fig. 3.4(a) the magnetic susceptibility and inverse susceptibility of a $Y_2Cu_2O_5$ single crystal oriented along the c axis are plotted as a function of temperature. A sharp maximum at 12 K is observed, marking a 3D AF ordering as reported previously [12, 13, 23]. Curie-Weiss fits to the linear region of the inverse susceptibility

yield a positive Curie-Weiss temperature of 43.5 K, indicating the presence of ferromagnetic exchange interactions [13]. The effective magnetic moment was calculated as 2.75 μB per formula unit in agreement with the value reported by Troc *et al.* [24]. In Fig. 3.4(b), magnetic susceptibility measurements along the three different crystallographic axes are presented. The magnetic anisotropy is small, but the susceptibility along *b* is larger than that for the other directions, thus *b* is the easy axis. In Fig. 3.5(a), the magnetic susceptibility along the easy axis is plotted for different applied fields. AF ordering is suppressed by a magnetic field, as reported previously [12].

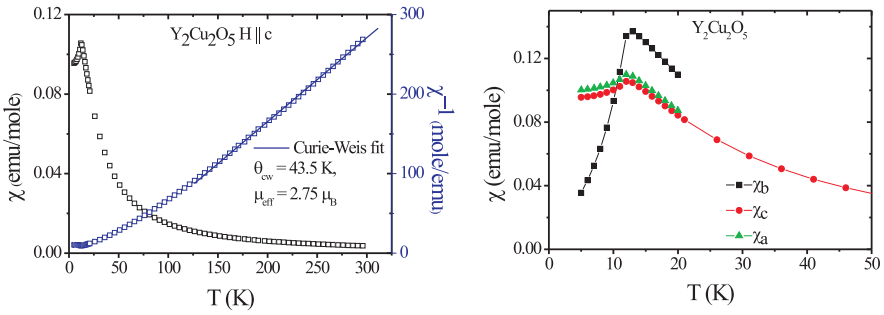

Figure 3.4: *(a) Magnetic susceptibility and its inverse vs temperature along the c axis. (b) Temperature dependence of magnetic susceptibility along different directions.*

The magnetic field dependence of the magnetization along the three crystallographic axes is also plotted in Fig. 3.5(c). Two field-induced transitions are observed, marked by steps in the magnetization, only when the magnetic field is applied parallel to the easy axis, *b*. Fig. 3.5(b) also shows how these magnetic transitions evolve with temperature; both transitions become broader on heating, while the critical field for the second transition, H_{c2}, decreases significantly. The critical fields for the two transitions and the maxima in the magnetic susceptibility measurements were previously used by Cheong *et al.* to construct a magnetic phase diagram [12]. The magnetic phase diagram obtained using our data was very similar, marking the presence of three magnetic phases [Fig. 3.5(d)].

The field-induced phase transitions have previously been investigated by neutron diffraction and symmetry analysis [17, 25]. The magnetic unit cell in the ground state consists of AF-coupled Cu pseudolayers stacked along the *c* axis; the magnetic moments in the layers point along [010]. The first step in the magnetization coincides with a tripling of the magnetic unit cell, which is due to the flip of one of the three spin dimers in every second layer to become aligned with the magnetic field [15, 17]. The magnitude of the increase in magnetization corresponds to 1/3 of the saturation magnetization [15]. The second field-induced transition has been interpreted as a spin-flop; the spins rotate such that they all become perpendicular to the field. After the spin-flop transition, upon further

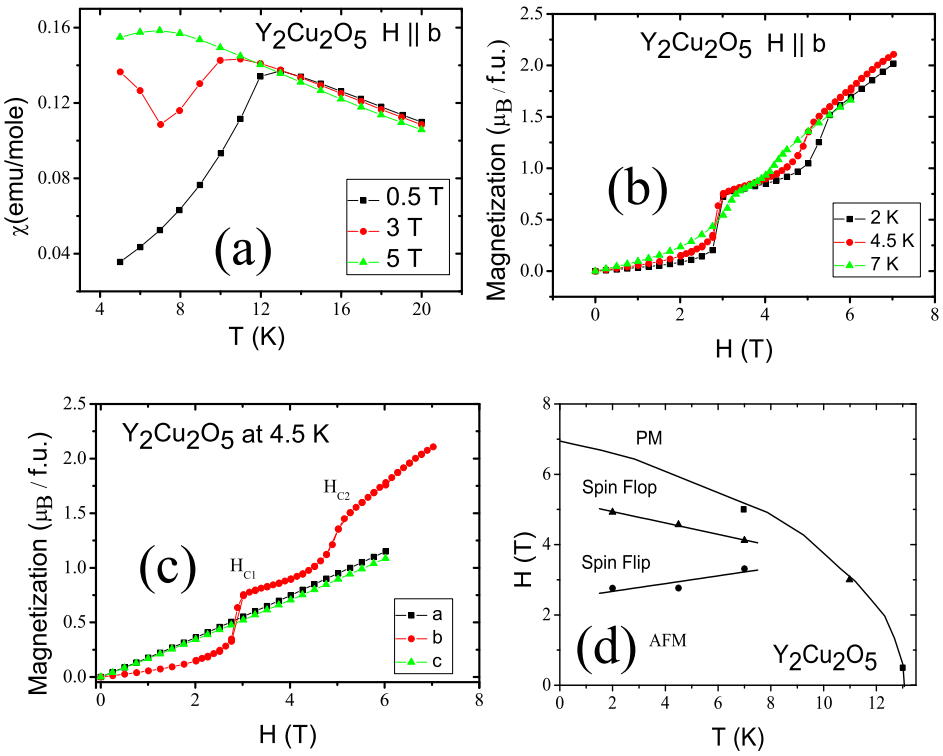

Figure 3.5: *(a) The magnetic susceptibility along the easy axis b is plotted for different applied fields. (b) Magnetic field dependence of b axis magnetization at different temperatures. (c)The magnetic field dependence of the magnetization along the three crystallographic axes. (d) Magnetic phase diagram obtained from magnetization measurements. Thin lines are guides to the eye.*

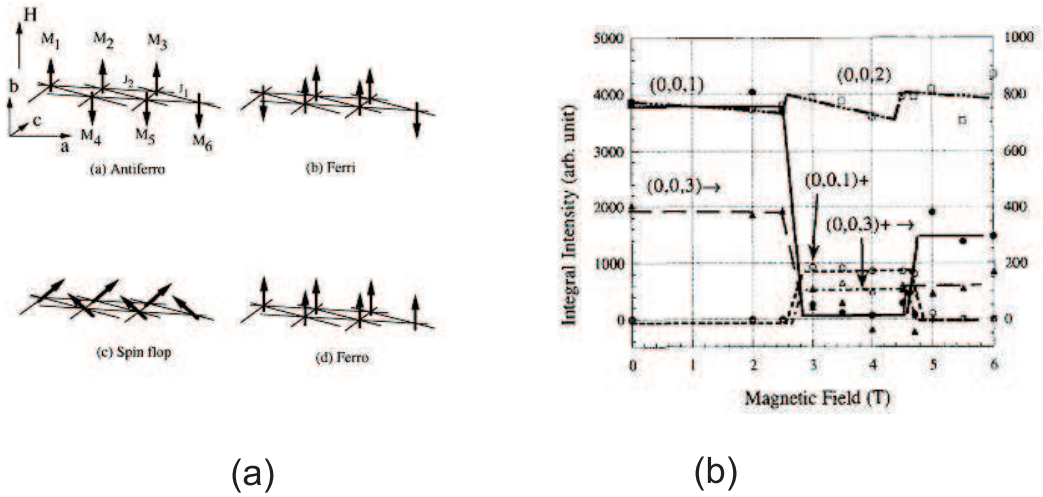

Figure 3.6: *(a) Magnetic structures of $Y_2Cu_2O_5$ reproduced from [26]. (b) Evolution of the diffraction intensities of magnetic reflections relevant to the field-induced transitions adapted from [17].*

increase in magnetic field the spins become aligned in the direction of the field and the magnetic moment is saturated [27]. Fig. 3.6(a) summarizes the different magnetic structures (from S.Kimura *et al.*, [26]), while the representative magnetic reflections from neutron diffraction are shown in Fig. 3.6(b). The magnetic field dependence of these reflections was used to solve the magnetic structure as a function of field [17]. The details of the different magnetic phases will be important when we discuss the magnetic field dependence of the dielectric constant.

Field-Induced Magnetic Transitions

It has been stated that "metamagnets are antiferromagnets, which upon the application of a magnetic field, can undergo first-order magnetic phase transitions to a state with a relatively large magnetic moment" [28]. Field-induced magnetic transitions differ in character for magnetic materials with strong anisotropy and with low or no anisotropy [28].

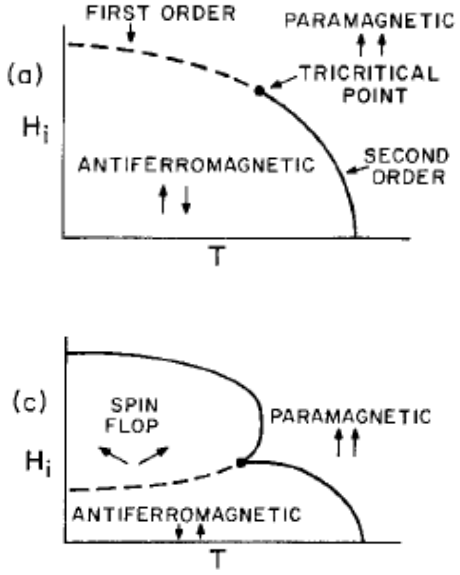

Figure 3.7: *Typical magnetic phase diagram for magnets having strong anisotropy (top) and low anisotropy (bottom) [28].*

Metamagnetic or spin-flip transitions occur when the anisotropy field is larger than the exchange field [29]. They are distinguished by simple reversals of the local spin directions. This is in contrast to what happens in materials with no or low magnetic anisotropy, where rotation of the local spins usually occurs. Fig. 3.7 shows typical examples of phase diagrams for both kinds of field-induced transitions. In Fig. 3.7(top), a schematic phase diagram for materials such as $FeCl_2$ and $DyPO_4$, which have strong magnetic anisotropy, is shown. As the temperature is decreased below T_N in zero field, the materials become antiferromagnetically ordered in a two-sublattice structure, where

the large anisotropy restricts the spins to lie either parallel or antiparallel to the easy axis. When a magnetic field is applied at temperatures just below T_N, a second-order phase transition to the paramagnetic phase occurs. At low applied fields, this transition occurs over a range of temperatures, forming a line of critical points. At lower temperatures and higher fields, the transition becomes first-order. The critical points of the second-order transition meet the line corresponding to the first-order phase transition at a tricritical point. Both in the AF and paramagnetic phases, the spins are restricted by the anisotropy to lie along the easy axis.

In Fig. 3.7 (bottom), a schematic magnetic phase diagram for two typical materials that display the second type of field-induced magnetic transition (MnF_2 and $GdAlO_3$) is shown. These materials do not have strong anisotropy. They order antiferromagnetically in zero field, and at low fields and temperatures just below T_N they display a second-order transition. However, at low temperatures, applied fields cause a first-order phase transition to take place where the spins become aligned perpendicular to the applied field. Further application of field induces a second-order transition to the paramagnetic phase as the spins rotate continuously to become aligned parallel to the magnetic field.

In $Y_2Cu_2O_5$ there is no single ion anisotropy because this is an $S = \frac{1}{2}$ system. Therefore, the magnetic anisotropy in the cuprates does not originate from single ion anisotropy [29].

3.2.3. (Magneto)Capacitance and Magnetoelectricity Measurements

It is known that $Y_2Cu_2O_5$ has a polar structure with space group $Pna2_1$, in which the polar axis is c. Therefore, spontaneous electrical polarization can be expected only along this direction. However, a polar crystal structure does not necessitate the presence of reversible spontaneous polarization, that is, ferroelectricity. In some pyroelectric materials the polarization is not switchable by an electric field. To the best of our knowledge, there are no reports in the literature on the existence of ferroelectricity in the polar $R_2Cu_2O_5$ family. There are two general signatures of ferroelectricity: the observation of a ferroelectric hysteresis loop or divergence of the dielectric constant and Curie-Weiss type behavior around the ferroelectric ordering temperature. We have measured ferroelectric (P-E) hysteresis loops for $Er_2Cu_2O_5$ and $Yb_2Cu_2O_5$ pellets at both room temperature and lower temperatures. The $Er_2Cu_2O_5$ pellet was 0.74 mm thick whereas the $Yb_2Cu_2O_5$ pellet was thinner. A voltage pulse with a maximum amplitude of 500 V was applied to measure the P-E loops. We observed a slight opening of the loop at room temperature, which was due to the lossy character of the sample. At lower temperatures a linear behavior was observed. The same kind of linear behavior was observed for the $Yb_2Cu_2O_5$ pellet. Therefore, we conclude that $R_2Cu_2O_5$ does not exhibit ferroelectricity.

Analyzing the unit cell one can see that the space group $Pna2_1$ has magnetic symmetry m'm'2,

by applying the time reversal operator to the crystal structure. For this magnetic point group, the linear magnetoelectric effect is allowed. According to Ref. [30] the corresponding magnetoelectricity tensor is

$$\begin{pmatrix} \alpha_{11} & 0 & 0 \\ 0 & \alpha_{22} & 0 \\ 0 & 0 & \alpha_{33} \end{pmatrix}$$

Therefore, we expect to observe magnetoelectric coupling in our measurements.

The free energy of materials displaying the linear magnetoelectric effect is $\Phi=\Phi_0-\alpha_{ij}E_iH_j$. An electrical polarization, P, can be induced under applied magnetic field: $P_i = d\Phi / dE_i = \alpha_{ij}H_j$. The magnetoelectricity tensor includes the α_{ij} for different directions. In the case of point group m'm'2, only the diagonal elements are non-zero. This means that if we apply a magnetic (electric) field along one axis, polarization (magnetization) must be induced along the same axis. We have measured the magnetoelectric effect along the *b* axis. Details of the measurement are given in section 2.5 of this thesis. Different magnetic and electric fields were used during the "magnetoelectric annealing" process. We were unable to observe any induced polarization along the *b* axis, which may be due to insufficient electrical poling and low magnetoelectric coupling, resulting in small induced currents. We note that the linear magnetoelectric effect in $GaFeO_3$ could not be demonstrated for exactly the same reason [31].

Within the polar cuprate family (R = Tb-Lu, Sc, Y and In), the dielectric constant has been reported only for $Er_2Cu_2O_5$, which has a high-frequency (ε_∞) value of 9 for polycrystalline samples [32]. We have measured for the first time the dielectric constant of $Y_2Cu_2O_5$ single crystal at low temperatures. Thus far, all of our measurements have been performed on crystals oriented along the easy *b* axis. For more detailed analysis of the origin of the dielectric anomaly at T_N, further measurements are necessary, especially along the polar axis, *c*. Moreover, measurements along this direction are essential to support our result regarding the absence of ferroelectricity.

The temperature dependence of the dielectric constant of $Y_2Cu_2O_5$ along the *b* axis is shown in Fig. 3.8. The value of dielectric constant is approximately 30 at low temperatures; this may differ from the value previously reported for polycrystalline $Er_2Cu_2O_5$ due to the anisotropy of our $Y_2Cu_2O_5$ single crystal. We note that the dielectric constant does not strongly depend on the measurement frequency in the low temperature range where our interest lies.

Dielectric anomalies are often observed at the magnetic ordering temperature in multiferroic and magnetoelectric materials (irrespective of the type of magnetic ordering). This is the case, for example, in $YMnO_3$, $BiMnO_3$ and Cr_2O_3, where it is recognized as evidence for magneto(di)electric coupling. We also observe such an anomaly in the dielectric constant of $Y_2Cu_2O_5$ at 13.2 K, where

AF ordering emerges. Two physical mechanisms might be responsible for this anomaly: magnetostriction and direct polar optical phonon-magnon (magnetoelectric) coupling [33]. Magnetostriction causes the lattice to contract along the direction of the exchange interaction, giving rise to an increase in the phonon energies of modes corresponding to the displacements, and the dielectric constant will decrease according to the LST (Lyddane-Sachs-Teller) equation. In the second mechanism direct magnon-phonon coupling can increase the energy of the lowest frequency transverse optical phonon, decreasing the dielectric constant. Such shifts of the phonon frequencies upon magnetic ordering have been reported for hexagonal $HoMnO_3$ [34] and $GdFe_3(BO_3)_4$ [35]. The temperature dependence of the dielectric constant involves the excitation of low-lying optical phonons. We have fitted the curve of the dielectric constant vs temperature to the Barrett's equation $\varepsilon_b(T)=\varepsilon_b(0)+C_0/[\exp(\hbar\omega_0/k_bT)-1]$ following Ref. [36]. In this equation, C_0 is a coupling constant and ω_0 is the mean frequency of the final states in the lowest lying optical phonon branch. We obtained values of 0.05 for C_0 and 16 ± 2 cm^{-1} for ω_0. No Raman or infrared studies have been carried out on single crystals of $Y_2Cu_2O_5$, and thus we are unable to say whether the phonon mode obtained from our dielectric constant fits corresponds to any particular Raman or infrared-active phonon in the sample. From studies on polycrystalline samples, the frequency of the lowest lying infrared active phonon is 74 cm^{-1} [37].

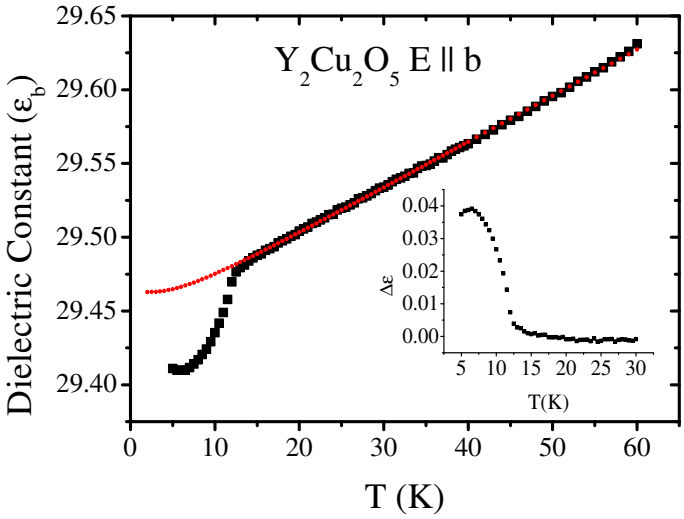

Figure 3.8: *Temperature dependence of the dielectric constant of $Y_2Cu_2O_5$. The line is a fit to the expression in Ref. [36]. The inset shows $\Delta\varepsilon$, the change in ε_b upon magnetic ordering, which is proportional to the square of the AF order parameter, L^2 (see main text for details).*

To evaluate the sharpness of the dielectric anomaly, and thus the coupling of magnetic ordering to polarization, we provide different examples from the literature. We observe that the dielectric anomaly in $Y_2Cu_2O_5$ is rather weak compared to those of the selected samples. $EuTiO_3$ is different to the other materials listed, because the transverse optical phonon that is affected by the magnetic ordering is "soft" i.e. phonon frequency is approaching zero and the change in the frequency is large [38].

Compound	$\Delta\varepsilon/\varepsilon(\%)$	T_N
$YMnO_3$	0.085	74 K [39]
MnF_2	0.025	67 K [40]
$EuTiO_3$	1	5.5 K [38]
$Y_2Cu_2O_5$	0.012	12 K (this thesis)
$Er_2Cu_2O_5$	0.0062	28 K (this thesis)

Table 3.1: *$\Delta\varepsilon/\varepsilon(\%)$ is the approximate difference between the measured low-temperature value of ε and the corresponding extrapolated value according to the temperature dependence of the behavior above T_N, normalized by the magnetic ordering temperature.*

The magnetic contribution to the dielectric constant can be modeled using Ginzburg-Landau theory. The free energy contains magnetic and electric terms and also terms that couple the polarization P and the (sublattice) magnetization (L) M. The dielectric constant is obtained by differentiating the equilibrium polarization with respect to the electric field. The lowest-order symmetry-allowed coupling terms are P^2L^2 or P^2M^2 because they leave the free energy invariant with respect to the symmetry operations of the magnetic space group. If both L and M are finite, terms including PLM can also be symmetry allowed. For the multiferroics $YMnO_3$ (see Chapter 4 on hexagonal manganites) and $BaMnF_4$ the suppression of the dielectric constant below T_N is thus associated with the emergence of the sublattice magnetization L and is proportional to L^2 [41]. We show $\Delta\varepsilon_b$ as an inset in Fig. 3.8.

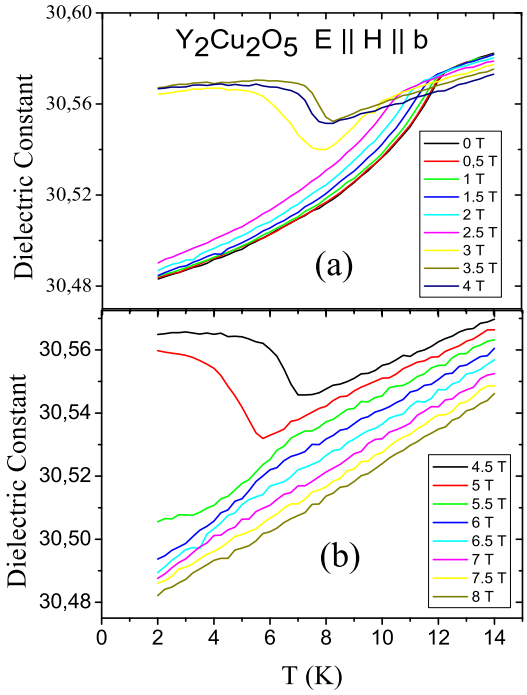

Figure 3.9: *Temperature dependence of the dielectric constant of $Y_2Cu_2O_5$ (a) between 0-4 T, (b) between 4.5-8 T, (c) between 2.7-4 T.*

It is revealing to look at both the temperature dependence of the dielectric constant under different magnetic fields and at the magnetic field dependence of the capacitance at different temperatures. For convenience, we abbreviate the former as ε_T(H) and the latter as ε_H(T). These measurements differ because ε_H(T) reflects both the temperature dependence and magnetic field dependence of the lattice polarizability. In contrast, ε_T(H) probes the change in the polarizability with magnetic field only.

In Fig. 3.9(a), ε_H(T) is plotted for various magnetic fields of up to 4 T. We observe that magnetic field shifts the dielectric anomaly at T_N to lower temperatures, consistent with the behavior of an antiferromagnet. For H $\geq$ 3 T, the dielectric constant first decreases at T_N before a second anomaly corresponding to an increase in the dielectric constant occurs at lower temperatures. This increase in dielectric constant coincides with the field-induced magnetic transition. In Fig. 3.9(b), data for fields up to 8 T are shown. We observe that above 5 T, the second anomaly in the dielectric constant vanishes, whereas the first anomaly corresponding to T_N is visible up to 7 T.

Magnetocapacitance measurements [Fig. 3.10(a)] at different temperatures better illustrate the relation between the field-induced magnetic transitions and the dielectric constant. At low fields (in the AF phase) and in the paramagnetic phase (not shown in detail), the dielectric constant varies quadratically with magnetic field, which can be explained by a P^2H^2 term in the Landau free energy

expression, a term that is allowed independent of the symmetry. The magnetocapacitance in this region is positive below T_N and negative at and above it. When the transition to the spin-flip phase occurs at 3 T, the dielectric constant increases abruptly. Close to 5 T the dielectric constant suddenly decreases as the transition from the spin-flip phase to the spin-flop phase takes place. We stress that because there are two net spins pointing along the *b* direction in the intermediate, spin-flip phase, a net magnetization is present. In contrast, extrapolation of the magnetization versus field curve in the spin-flop phase intersects the origin [Fig. 3.5(b)]. Above 6 T, the dielectric constant decreases with field in approximately linear fashion. From the unnormalized capacitance versus field curves of Fig. 3.10(b), it is possible to observe a change in slope at approximately 6 T corresponding to a further transition from the spin-flop phase to the paramagnetic phase. For example, the 5 K data clearly show the presence of four phases along a single curve.

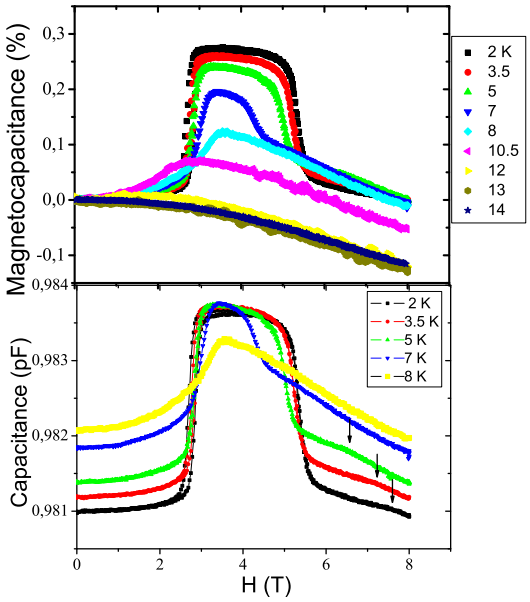

Figure 3.10: *(a) Magnetocapacitance of $Y_2Cu_2O_5$ and (b) unnormalized capacitance versus magnetic field, for $E \parallel b$ and $H \parallel b$. Arrows indicate the phase transitions from the spin-flop phase into the paramagnetic phase.*

By using the anomalies in the ε_H(T) and ε_T(H) measurements, we have constructed a magnetic phase diagram (Fig. 3.11) that is in agreement with the phase diagram obtained from the magnetization measurements. In Fig. 3.12, we show a 2D projection of the 3D phase diagram, which clearly reveals the phase boundary between the AF phase and the spin flip phase. The color scale represents the changes in the dielectric constant with field and temperature, which enables the phase boundaries to be observed.

The phase diagram contains four different magnetic phases. In the ground state, the magnetic ordering is AF in nature. As the field is increased, a transition to the spin-flip phase occurs. The

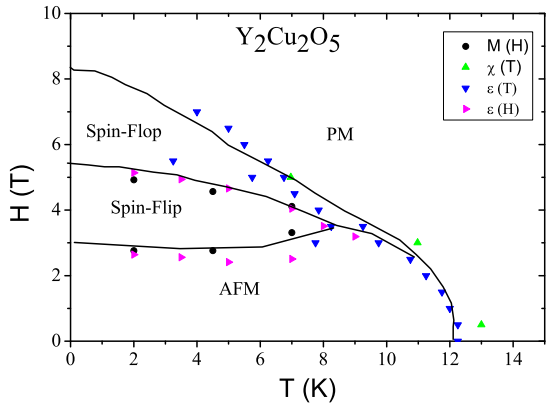

Figure 3.11: *Magnetic phase diagram of $Y_2Cu_2O_5$ obtained using datapoints of different measurements.*

spins then flop with further increasing field, and finally the spins rotate and saturate at high fields, where the material is paramagnetic. With the magnetic phase diagram at hand, it is revealing to look once again at the magnetocapacitance data. One striking point worth emphasizing is the nature of the dielectric anomalies in the different magnetic phases. In the AF phase, a decrease in the dielectric constant at T_N occurs. At 3 T, when the sample is cooled down from 14 K, a decrease in ε(T) occurs as the AF phase is entered, followed by an increase in ε(T) at approximately 8 K where the transition to the spin-flip phase occurs. At higher fields, such as 5 T, the sample first enters the spin-flop phase when cooling from 14 K, but no clear anomaly can be seen. When the temperature is further decreased, a transition to the spin-flip phase occurs, which is coincident with an increase in ε(T). When the sample is cooled from 14 K in a field of 6 T, the spin-flop phase is entered directly and ε decreases. Summarizing these observations, transitions to ground AF state and the spin-flop state involve a decrease in ε(T). In the spin-flip phase, there is net magnetization and the dielectric constant increases when the transition to this phase occurs. This increase in ε(T) is consistent with the field-dependence of the dielectric constant. The dielectric constant is significantly larger in the spin-flip phase than in the other magnetic phases.

It is very unusual to observe an increase in ε(T) with decreasing temperature. To the best of our knowledge, theoretically there is no prediction for the sign of the dielectric anomalies due to magnetic ordering [36]. One of the rare examples for which such a feature occurs is hexagonal $HoMnO_3$, where the increase in ε(T) is very sharp, associated with a magnetic phase transition. Magnetocapacitance measurements on this compound also showed an abrupt increase in the dielectric constant when the phase transition was induced. The symmetry of the high-dielectric constant phase in $HoMnO_3$ and the spin-flip phase in $Y_2Cu_2O_5$ have one property in common: the $P6_3$ space

group in $HoMnO_3$ allows spin canting and therefore a ferromagnetic component is present [42], just like the spin-flip phase in $Y_2Cu_2O_5$. However, we note that a more recent publication establishes a different magnetic symmetry for the high-dielectric constant phase of $HoMnO_3$, which does not allow spin canting [43]. One could use our results to propose that whenever there is net magnetization, the dielectric constant will increase below the magnetic ordering temperature. However, this proposition would be incorrect; for example, the dielectric anomaly in ferromagnetic $BiMnO_3$ is negative [44].

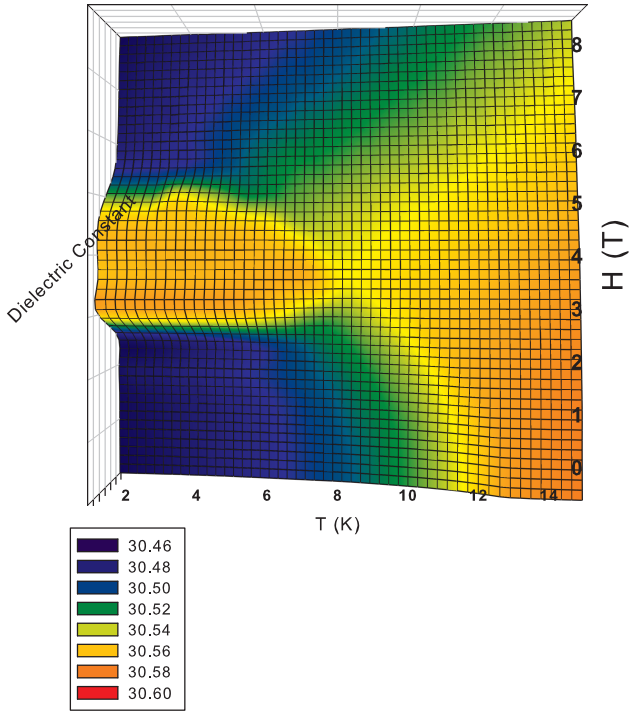

Figure 3.12: *A 2D projection of the 3D magnetic phase diagram of $Y_2Cu_2O_5$.*

We can attempt to use the spin-pair correlation model of Katsufuji *et al.* [38] in order to describe the behavior of ε_T(H) in the different phases. This model considers a simple perturbation to the dielectric constant by magnetic ordering. The formula is ε(T,H) = ε_0(T)(1+$\alpha\langle S_i.S_j \rangle$). Here, ε_0(T) is the dielectric constant in the absence of spin correlation and α is the coupling constant of the spin correlation and dielectric constant [38]. Assuming a positive value for α, if the spins are antiferromagnetically ordered then the spin correlation will be negative and the dielectric constant will decrease upon magnetic ordering. Under certain magnetic fields, the spins flip, as in our spin-flip phase, and this time the spin correlation will be positive and the dielectric constant will increase. This also seems to hold for our spin-flip phase. In the spin-flop phase, the spin correlation will be negative again and ε will decrease. This is also in agreement with our measurements. However, in

the paramagnetic phase the spins will be parallel to each other, making the correlation positive and maximum, and ε should increase. We do not observe any increase in ε in this phase. Therefore, such a simple spin correlation function cannot account for the behavior of our system.

The origin of the dielectric anomaly and magnetocapacitance in $Y_2Cu_2O_5$ is not clear. The dielectric anomaly at T_N is observed along *b* axis, and we were unable to perform measurements along the polar *c* axis. Since along the *b* direction the material is not polar, the possibility of direct coupling of polar phonons to magnons can be ruled out. Moreover, even though the magnetic symmetry permits the existence of the linear magnetoelectric effect, we were unable to observe any magnetoelectric effect within experimental error. Therefore, it is unlikely that the magnetocapacitance we measure is due to the linear magnetoelectric effect. Thus, we propose that spin-phonon coupling is the origin of the magnetodielectric phenomena, causing shifts in the phonon frequencies at T_N or at the phase boundaries between different magnetic phases. Additionally, exchange striction changes the dimensions of the sample and causes shifts in the optical phonon frequencies which affects the dielectric constant via the Lyddane-Sachs-Teller (LST) relation (See equation 1.7 in Chapter 1). We note that such a general mechanism was used recently to explain the "magnetization-induced changes in dielectric constant" in magnetodielectric Mn_3O_4 [45].

In conclusion, we have measured the (magneto)capacitance of $Y_2Cu_2O_5$ single crystals and observed different types of anomalies at the different magnetic phase transitions. The magnetic field dependence mainly originates from an abrupt increase of the dielectric constant when the spin-flip phase is entered. Significant magnetodielectric coupling is demonstrated by anomalies in the field and temperature dependence of the dielectric constant, which allows the construction of a magnetic phase diagram with higher resolution than using magnetization measurements alone. We stress that even though experimentally we were unable to observe the linear magnetoelectric effect, it is symmetrically allowed. However, our initial expectation of obtaining large magnetocapacitance due to the allowance of the linear magnetoelectric effect and the polar nature of the material was not fulfilled. The magnetocapacitance that we measured for $Y_2Cu_2O_5$ remained comparable to that of the hexagonal manganites (see Chapter 4 of this thesis). Hexagonal manganites are multiferroic, but their magnetic symmetry does not allow the linear magnetoelectric effect. This shows once again that the magnetoelectric coupling mechanism determines the magnitude of the coupling rather than symmetry conditions alone.

Before closing this section, it should be noted that we also observe a poorly-defined dielectric anomaly at T_N for polycrystalline $Y_2Cu_2O_5$ (see Fig. 3.13).

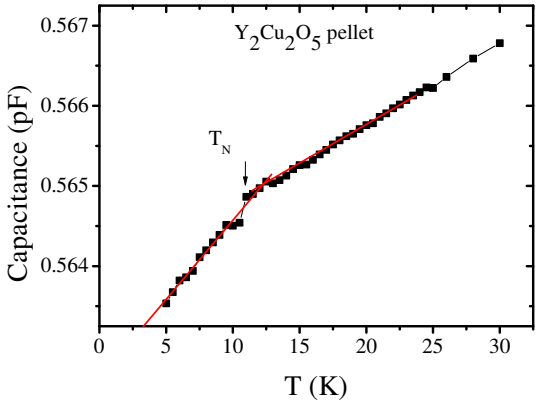

Figure 3.13: *Temperature dependence of the dielectric constant of polycrystalline $Y_2Cu_2O_5$.*

3.3. Polycrystalline $Er_2Cu_2O_5$

3.3.1. Introduction

In comparison to $Y_2Cu_2O_5$, the properties of $Er_2Cu_2O_5$ have been much less studied. Neutron diffraction has shown that the Cu and Er spins order simultaneously in antiferromagnetic fashion at 28 K [15]. The Cu spin ordering is analogous to that in $Y_2Cu_2O_5$, where ferromagnetic Cu dimers in the *ab* plane are coupled antiferromagnetically along *c*. The main components of both the Cu and Er spins point along [010]. The antiferromagnetically coupled Cu layers are separated by two Er layers along *c*, the spins in each Er layer being ordered antiparallel to the neighboring Cu layer; thus, there is antiferromagnetic superexchange between the Er and Cu spins [15]. A sketch of the magnetic unit cell from Ref. [15] is provided in Fig. 3.14.

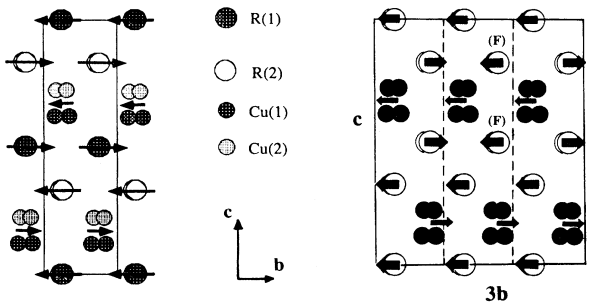

Figure 3.14: *Magnetic unit cell of $Er_2Cu_2O_5$ before (left) and after (right) the field-induced magnetic transition, taken from [15].*

3.3.2. Synthesis

$Er_2Cu_2O_5$ powder was synthesized from the pre-dried oxide precursors Er_2O_3 and CuO. After grinding in acetone, the powder was sintered at 950 °C for 12 h in air. The resulting sample contained a trace of unreacted Er_2O_3, which disappeared after repeated regrinding, pelletizing and sintering at the same temperature. The X-ray diffraction pattern of the sample showed good quality $Er_2Cu_2O_5$ (Fig. 3.15) Refined lattice parameters were a = 10.7755(4) Å, b = 3.4714(1) Å, and c = 12.4397(5) Å.

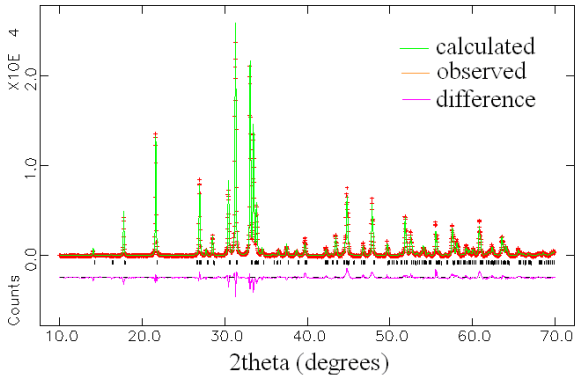

Figure 3.15: *Refinement results at RT for polycrystalline* $Yb_2Cu_2O_5$.

3.3.3. Results and Discussion

The magnetic susceptibility of polycrystalline $Er_2Cu_2O_5$ measured as a function of temperature is shown in Fig. 3.16. Two cusps are observed at 26.5 K and 12.7 K, consistent with previous reports [13, 18]. The 26.5 K anomaly is due to the simultaneous ordering of Er and Cu spins as evidenced by neutron diffraction [15], but the origin of the second anomaly remains unclear [18]; no transition has been reported here on the basis of neutron diffraction data [15]. A Curie-Weiss fit of the inverse susceptibility above 200 K yielded a Weiss temperature of -4.4 K and an effective magnetic moment of 13.2 μ_B. These two parameters are in agreement with previous reports [13, 18].

The magnetization of $Er_2Cu_2O_5$ is plotted as a function of field in Fig. 3.17. Changes in slope are apparent at all temperatures below T_N, being more pronounced at lower temperatures. The critical field necessary to induce the change in slope increases with temperature. In contrast to $Y_2Cu_2O_5$ and in accordance with previous measurements [18], the magnetization curves show hysteresis below 10 K. We have constructed a magnetic phase diagram using the temperature evolution of the critical field in Fig. 3.18, which is in agreement with the one reported in [18]. This metamagnetic transition has been studied by Rodriguez-Carvajal *et al.* [15]. Based on the increase in magnetization involved,

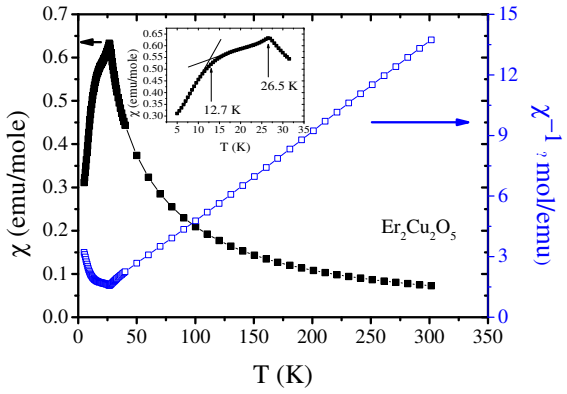

Figure 3.16: *Temperature dependence of magnetic susceptibility of $Er_2Cu_2O_5$ and its inverse, showing the Curie-Weiss fit; the inset shows the low-temperature susceptibility in more detail, with the magnetic ordering temperatures indicated.*

a new magnetic unit cell was proposed for the field-induced phase, illustrated in Fig. 3.14. The unit cell is tripled along *b* and according to Ref. [15], the jump in magnetization is caused by a flipping of the Er spins marked by F in Fig. 14. We are unaware of any other studies addressing the nature of the metamagnetic transition.

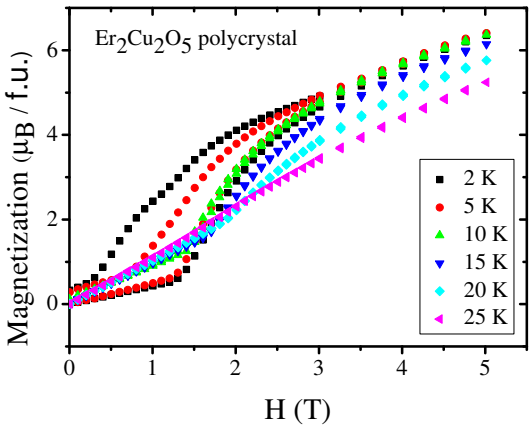

Figure 3.17: *Magnetization of $Er_2Cu_2O_5$ vs magnetic field at different temperatures.*

Fig. 3.19 shows the temperature dependence of the dielectric constant measured at 100 kHz. The value of the dielectric constant is approximately 13 at low temperatures, where the extrinsic contribution to the dielectric constant is negligible. This is comparable to the value of 9 measured by

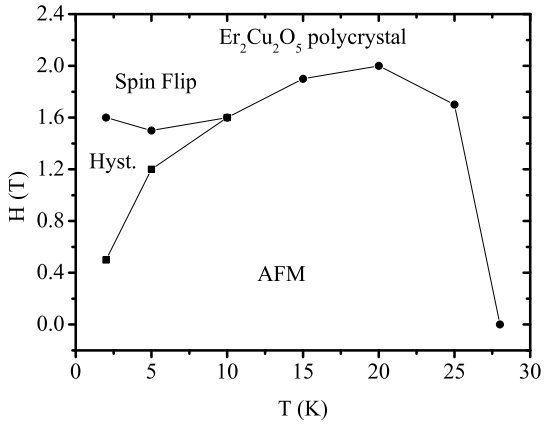

Figure 3.18: *Magnetic phase diagram of polycrystalline $Er_2Cu_2O_5$.*

Knebel *et al.* at room temperature and GHz frequencies in order to eliminate any extrinsic contributions [32]. There is a clear anomaly below T_N, where the Cu and Er sublattices order simultaneously. However, despite the observation of a second anomaly in the magnetic susceptibility at 12.5 K, no corresponding anomaly in the dielectric constant was visible.

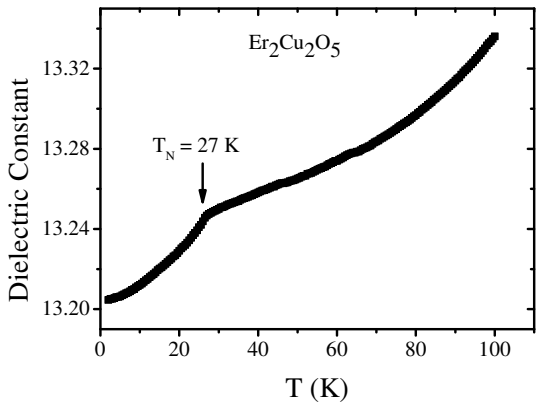

Figure 3.19: *Temperature dependence of the dielectric constant of $Y_2Cu_2O_5$ pellet measured at 100 kHz.*

The magnetocapacitance of polycrystalline $Er_2Cu_2O_5$ is plotted in Fig. 3.20 for temperatures above 15 K; at lower temperatures the noise level is high. At 15 K, the magnetocapacitance is positive up to 1.6 T, where a change in slope takes place. The capacitance of the sample then starts to decrease with further increasing magnetic field, before saturation is reached above 4 T. The magnetocapacitance at 20 K is similar to that at 15 K, although the critical field is higher. At 25 K,

a change in slope of the magnetocapacitance is still observed, but the critical field remains the same as at 20 K. There is no saturation of the magnetocapacitance up to the maximum field applied. At 27 K and 30 K, the magnetocapacitance is negative and linear at high fields.

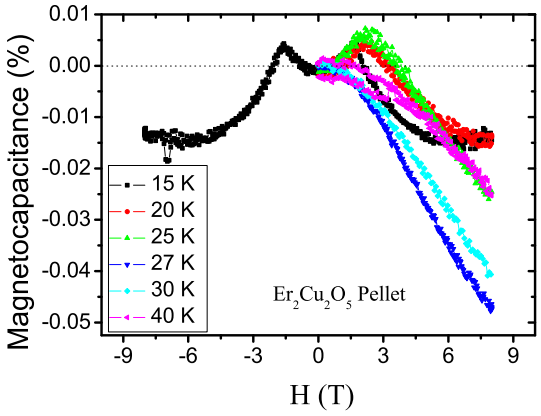

Figure 3.20: *Magnetocapacitance of polycrystalline $Er_2Cu_2O_5$ at different temperatures.*

3.4. Polycrystalline $Yb_2Cu_2O_5$

3.4.1. Introduction

Neutron diffraction has previously been used to solve the magnetic structure of $Yb_2Cu_2O_5$. Unlike $Y_2Cu_2O_5$ and $Er_2Cu_2O_5$, the **k** vector is not (0, 0, 0) but (0, 1/2, 1/2) at 1.5 K; this means that the magnetic unit cell is doubled along *b* and *c*, as shown in Fig. 3.21 [46]. In similar fashion to the Y and Er compounds, the Cu spins lie parallel to *b* in ferromagnetic pseudolayers. Adjacent pseudolayers are coupled antiferromagnetically along *c*. The Yb spins are also aligned parallel to *b*. When a magnetic field is applied, five successive metamagnetic transitions have been reported for $Yb_2Cu_2O_5$, the highest at 12 T [18].

3.4.2. Synthesis

$Yb_2Cu_2O_5$ powder was synthesized from the pre-dried oxide precursors Yb_2O_3 and CuO. The sintering process was similar to that of $Er_2Cu_2O_5$. After grinding in acetone, the powder was sintered at 950 °C for 12 h in air. The resulting sample contained a trace (approximately 0.1 %) of unreacted Yb_2O_3; the sample was then repeatedly reground and sintered at the same temperature until no Yb_2O_3 could be detected in the X-ray diffraction pattern (see Fig. 3.22). The lattice parameters

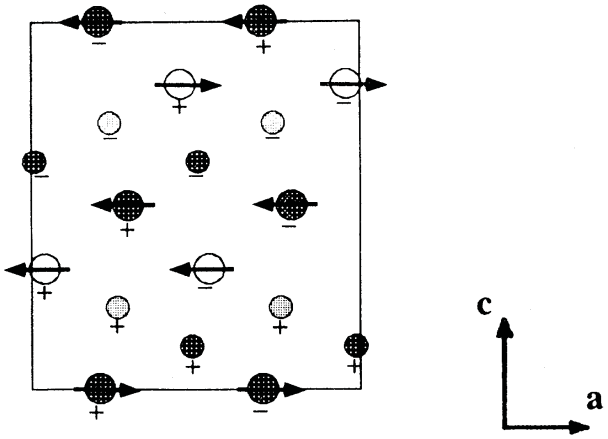

Figure 3.21: *Sketch of the magnetic unit cell of $Yb_2Cu_2O_5$ from [15], where R1 and R2 represent the Yb1 and Yb2 cations, respectively.*

obtained from the refinement are a = 10.7289(11) Å, b = 3.4355 (3) Å, and c = 12.3539(13) Å, which are close to the previously reported values [14].

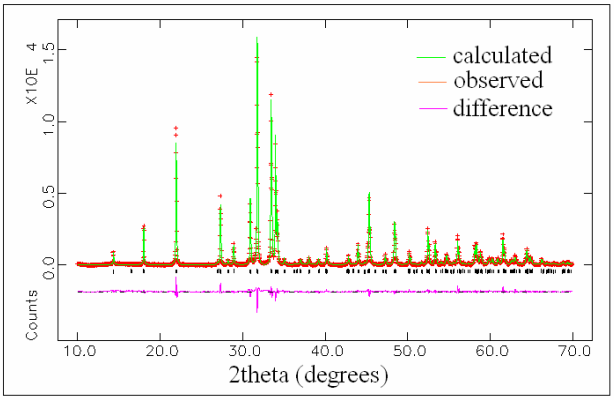

Figure 3.22: *Refinement results at RT for polycrystalline $Yb_2Cu_2O_5$.*

3.4.3. Results and Discussion

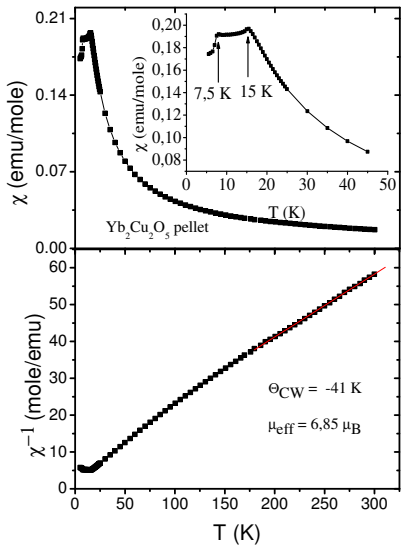

Figure 3.23: *Temperature dependence of magnetic susceptibility of $Yb_2Cu_2O_5$ and its inverse, showing the Curie-Weiss fit; the inset shows the low-temperature susceptibility data in more detail, with the magnetic ordering temperatures indicated.*

The temperature dependence of the magnetic susceptibility is shown in Fig. 3.23. We observe a cusp at 15 K and an anomaly at 7.5 K, in agreement with previous reports [**?**, 18]. Unlike $Er_2Cu_2O_5$, neutron diffraction has shown that the Cu and Yb sublattices order separately [25]. The cusp in susceptibility at 15 K is associated with ordering of the Cu sublattice, and the second anomaly is associated with ordering of the Yb sublattice. It has been suggested that the latter transition is first-order because neutron diffraction experiments showed that the ordered Yb moment became saturated within 1 K of the ordering temperature [25]; furthermore, the corresponding peak in specific heat is λ-like in shape [47]. The Curie-Weiss temperature calculated from a fit to the inverse susceptibility between 200 and 300 K was -41K, which is different to the value of 7.5 K reported in two previous studies [13, 18]. However, only one of these papers shows the inverse susceptibility fit [13], and fitting has apparently been attempted on the nonlinear part of the inverse susceptibility below 100 K. We calculated an effective magnetic moment of 6.85 μB from our data, which is close to the value that is calculated by assuming a moment of 1.95 μB for Cu^{2+} and the free ion value for Yb^{3+} (4.54

μB). Another feature unique to $Yb_2Cu_2O_5$ is that the Cu spins order in incommensurate fashion in the temperature region between T_N (15 K) and the ordering temperature of the Yb sublattice (assumed to be 7.5 K from the second anomaly in the magnetization). The Cu spin ordering then becomes commensurate at lower temperatures. Frustrated Yb-Cu interactions are believed to be responsible for this behavior [48].

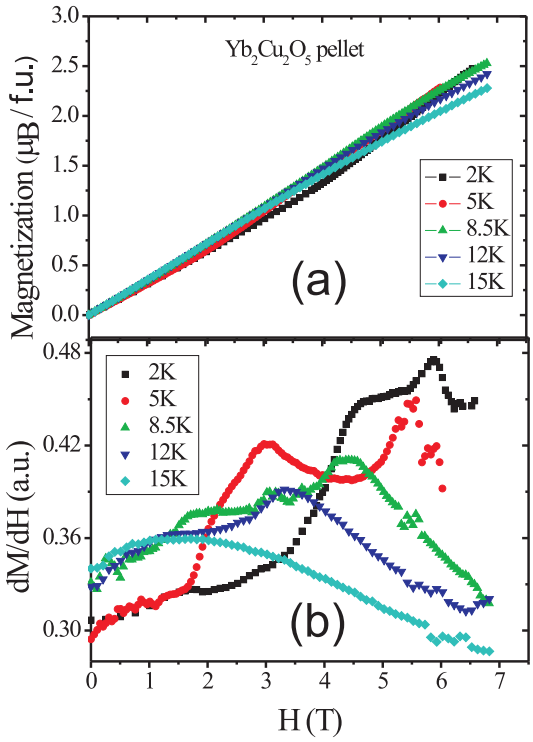

Figure 3.24: *(a) Magnetic field dependence of magnetization of polycrystalline $Yb_2Cu_2O_5$ at different temperatures. (b) Derivative of (a).*

We show the field dependence of the magnetization of $Yb_2Cu_2O_5$ in Fig. 3.24(a). The field-induced transitions are only visible when the derivative of the magnetization is plotted, as shown in Fig. 3.24(b) for different temperatures. At 2 K and 5 K three field-induced transitions are apparent. At 8.5 K, two transitions are clearly present at 1.66 T and 4.36 T, while another less pronounced anomaly is visible close to 3 T. Above 8.5 K two clear anomalies are still observed, whereas there is no indication of any transition at 15 K. We have constructed a magnetic phase diagram from these data in Fig. 3.25. The critical fields are taken at the maxima in the derivative plots. The first field-induced phase transition takes place at approximately 1.7 T, a critical field that is not affected significantly by temperature. For temperatures $\leq$ 8.5 K, there are two more field-induced transitions

at higher fields. Among members of the orthorhombic $R_2Cu_2O_5$ family, $Yb_2Cu_2O_5$ appears to exhibit the greatest number of metamagnetic transitions; at 4.2 K, three transitions were reported for polycrystalline samples below 6 T, and two more transitions above 6 T [18]. However, only one transition below 5 T was observed in magnetization measurements on single crystals [49]. Our measurements agree with those of Kazei *et al.*, where there are three field-induced phase transitions below 6 T [18]. However, the nature and origin of these transitions remains unknown. No neutron diffraction studies under magnetic field have yet been reported.

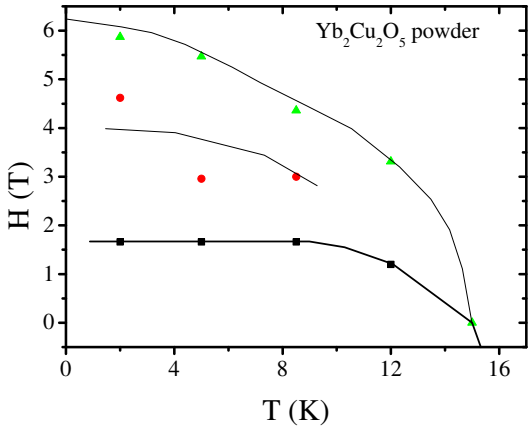

Figure 3.25: *Magnetic phase diagram of $Yb_2Cu_2O_5$ constructed from transitions observed in magnetization measurements.*

The temperature dependence of the capacitance is shown in Fig. 3.26. There is a slight change in slope in the vicinity of T_N (T_N was determined as 15 K from magnetic susceptibility measurements, whereas the anomaly in the capacitance is observed at 12 K); this is in contrast to the sharp anomaly observed at T_N for polycrystalline $Er_2Cu_2O_5$ and single crystal $Y_2Cu_2O_5$. There is another slight change in slope at the ordering temperature of the Yb spins, which is 7.5 K from magnetic susceptibility measurements.

The magnetocapacitance measurements shown in Figs. 3.27 and 3.28 are consistent with the magnetization measurements in terms of the number of anomalies. This is illustrated by the 2 K measurement in Fig. 3.27. At low fields, the capacitance of the sample decreases slowly with increasing magnetic field until a change in slope takes place at 1.7 T. Further changes in slope are observed at 4.5 T and 6 T, above which the slope deviates from linearity.

For clarity, the magnetocapacitance data in Fig. 3.28 have been plotted only for increasing magnetic fields. However, at low temperatures we observe hysteresis between data collected for increasing and decreasing fields, examples of which are shown in Fig. 3.29(a) and (c) for 3 K

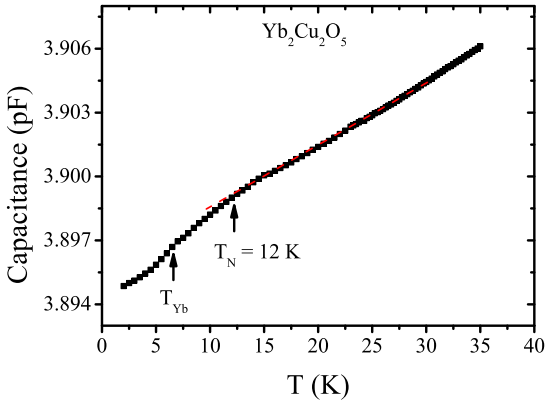

Figure 3.26: *Temperature dependence of capacitance of $Yb_2Cu_2O_5$, the thin line is a guide to the eye to pinpoint T_N.*

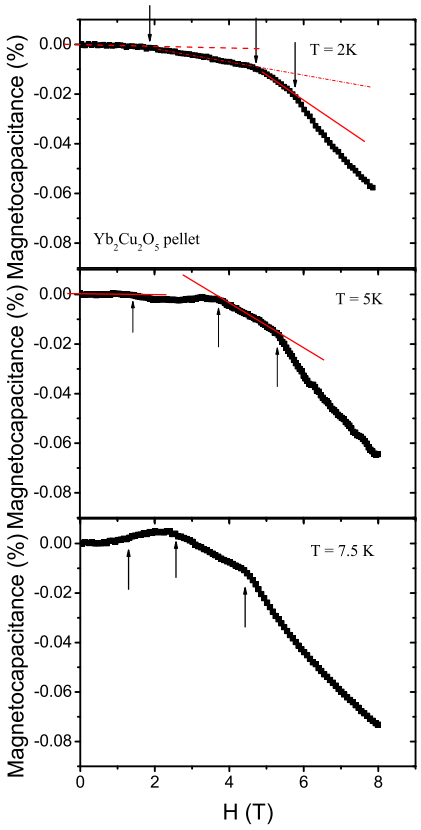

Figure 3.27: *Magnetocapacitance of $Yb_2Cu_2O_5$ at 2 K, 5 K and 7.5 K. Arrows indicate the positions of three phase transitions, and the lines are guides to the eye.*

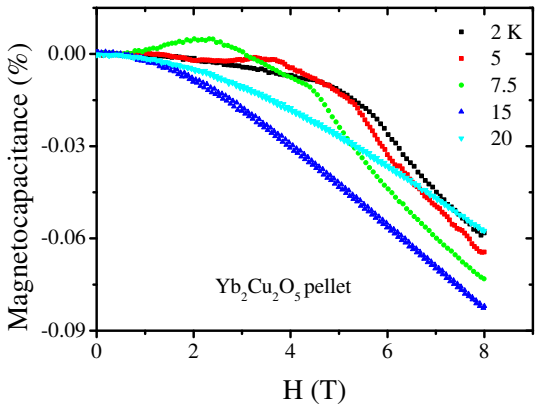

Figure 3.28: *Magnetocapacitance measurements of $Yb_2Cu_2O_5$ at selected temperatures.*

and 7.5 K, respectively. In the 7.5 K data, on decreasing the field from 8 T, the transition close to 5 T remains unaffected but the transition that was observed close to 3 T for increasing field seems to have disappeared. Unfortunately, we have not carried out magnetization measurements for decreasing field. There are conflicting reports in the literature regarding hysteresis in magnetization measurements on $R_2Cu_2O_5$ materials. Kazei *et al.* argue that among this cuprate family, magnetic hysteresis is observed only in $Er_2Cu_2O_5$ (both single crystals and polycrystalline samples) [18]. On the contrary, Szymczak *et al.* have reported magnetic hysteresis below the ordering temperature of the Yb spins in single crystal $Yb_2Cu_2O_5$ [49]; the data measured at 3 K are reproduced in Fig. 3.29(b). Comparing with our magnetocapacitance measurements in Fig. 3.29(a), it is clear that the metamagnetic transition that occurs at 4 T for measurements in increasing field is shifted to lower fields when the measurements are performed in decreasing field. We present magnetocapacitance measurements performed at 3 K for increasing and decreasing fields on single crystal $Yb_2Cu_2O_5$ in Fig. 28(a). The metamagnetic transition that occurs at 4 T for measurements in increasing field is shifted to lower fields when the measurements are performed in decreasing field, both in the magnetization and MC measurements.

We have used the values of the critical fields obtained from the MC data to add to the magnetic phase diagram that was constructed from the magnetization measurements. We have used only the critical fields determined from measurements performed while increasing the field. The updated magnetic phase diagram is presented in Fig. 3.30. There are no reports in the literature on the nature of these field-induced phases.

In conclusion, we have demonstrated that magnetodielectric coupling is present in polycrystalline $Yb_2Cu_2O_5$. We have observed a small anomaly in the capacitance at T_N. Another sharp but

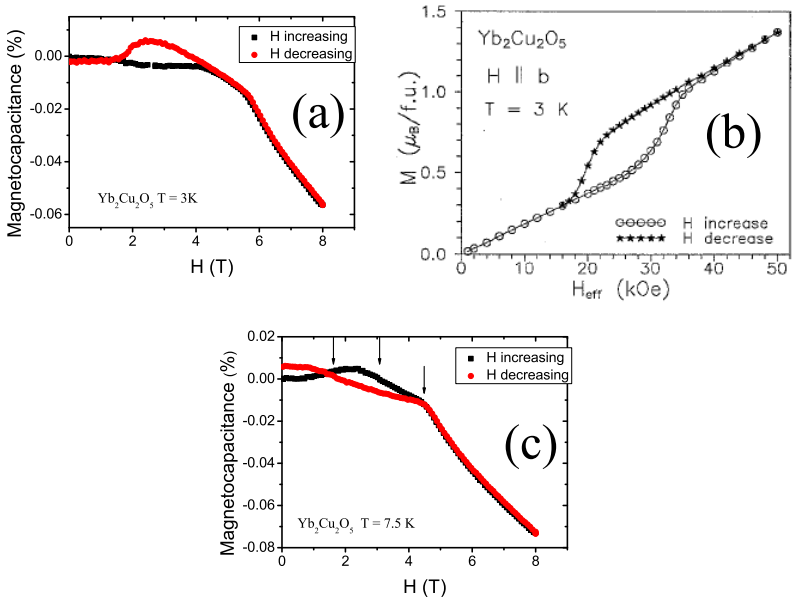

Figure 3.29: *Magnetocapacitance measurements at 3 and 7.5 K are replotted in (a) and (c) also including data collected in decreasing field, where hysteresis is apparent. (b) The corresponding magnetization measurement performed on a single crystal sample at 3 K, taken from ref. [49].*

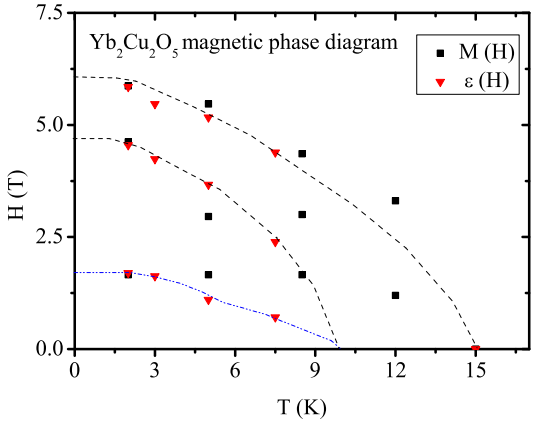

Figure 3.30: *Magnetic phase diagram constructed from transitions observed in magnetization and magnetocapacitance measurements.*

less pronounced anomaly in the capacitance was observed at the ordering temperature of the Yb spins. The magnetocapacitance of $Yb_2Cu_2O_5$ is negative, and three anomalies were observed in measurements carried out up to 8 T. Hysteresis was present in measurements carried out in increasing and decreasing magnetic field below 7.5 K. We have used the anomalies in the magnetization and MC data to construct a magnetic phase diagram.

3.5. General Conclusions

We have successfully synthesized single crystals of the incongruent melting compound $Y_2Cu_2O_5$, and have studied magnetic properties, the dielectric response and the magneto-dielectric coupling. Measurements of ε(T) reflect the temperature dependence of the bare lattice contribution, superimposed on the contributions reflecting the magnetic order parameters. ε(T) is thus a good gauge for the emergence of order and reflects the temperature dependence of the order parameter. The magnetocapacitance is sensitive to various field induced phase transitions. Neither the general form nor the sign of the magnetocapacitance in $R_2Cu_2O_5$ has yet been predicted from theory. Nevertheless, the magnetocapacitance can be effectively used to map magnetic phase diagrams, providing more detail than that available from magnetization data and neutron scattering data alone.

Bibliography

[1] S.-W. Cheong, and M. Mostovoy, Nature, 6, 13-20, (2007).

[2] N. A. Hill , Journal of Phys. Chem. B, 104 (29), 6694-6709, (2000).

[3] J.F. Scott, Rep. Prog. Phys. 12, 1055, (1979).

[4] B. B. van Aken, T. T. M. Palstra, A. Filippetti, and N. A. Spaldin, Nature Materials, 3, 164, (2004).

[5] N. Ikeda, H. Ohsumi, K. Ohwada, K. Ishii, T. Inami, K. Kakurai, Y. Murakami, K. Yoshii, S. Mori, Y. Horibe, and H. Kito, Nature, 436, 1136, (2005).

[6] T. Kimura, T. Goto, H. Shintani, K. Ishizaka, T. Arima, and Y. Tokura, Nature (London), 426, 55 (2003).

[7] M . Eibschtz, H. J. Guggenheim, S. H. Wemple, I. Camlibel and M. DiDomenico, Jr., Physics Letters A, 29, 409-410, (1969).

[8] E. T. Keve, S.C. Abrahams, and J.L. Bernstein, The Journal of Chemical Physics, 51, 4928-4936, (1969).

[9] U. Adem, M.Mostovoy, N. Bellido, A. A. Nugroho, C. Simon and T. T. M. Palstra, unpublished, (2007).

[10] T. Katsufuji and H. Takagi, Phys. Rev.B, 64, 054415, (2001).

[11] N. Bellido, Ch. Simon, and A. Maignan, Phys. Rev.B, 77, 054430, (2008).

[12] S. -W. Cheong, J. D. Thompson, Z. Fisk, K. A. Kubat-Martin, and E. Garcia, Phys. Rev.B, 38, 7013, (1988).

[13] R. Troc, J. Klamut, Z. Bukowski, R. Horyn, and J. Stepien-Damm, Physica B, 154, 189-196, (1989).

[14] J. L. Garcia-Munoz and J. Rodriguez-Carvajal, Journal of Solid State Chemistry, 115, 324, (1994)

[15] J. L. Garcia-Munoz, J. Rodriguez-Carvajal, X. Obradors, M. Vallet-Regi, J. Gonzales-Calbet, and M. Parras, Phys. Rev.B, 44, 4716, (1991).

[16] J. Aride, S. Flandrois, M. Taibi, A. Boukhari, M. Drillon and J. L. Soubeyroux, Solid State Communications, 72, 459, (1989).

[17] Y. Matsuoka, Y. Nishimura, S. Mitsudo, H. Nojiri *et al.* Journal of Magnetism and Magnetic Materials, 177-181, 729-730, (1998).

[18] Z.A. Kazei *et al.*, Journal of Magnetism and Magnetic Materials, 86, 124-134, (1990).

[19] Y. Nishimura *et al.*, Journal of Crystal Growth, 207, 206-213, (1999).

[20] N. Imanaka, G. Adachi. H. Dabrowska, A. Dabkowski and J. E. Greedan, Journal of Crystal Growth, 141, 150-152, (1994).

[21] A. Revcolevschi and J. Jegoudez, Progress in Materials Science, 42, 321-339, (1997).

[22] X. L. Chen, Y. Y. Ji, J. K. Liang, X. R. Cheng, J. Li and S. S. Xie. J. Alloys Compd., 191, 297, (1993).

[23] B. L. Ramakrishna, E.W. Ong and Z. Iqbal, Solid State Communications, 68, 775-779, (1988).

[24] R. Troc, Z. Bukowski, R. Horyn, and J. Klamut, Phys. Letters A, 125, 222, (1987).

[25] J. L. Garcia-Munoz, X. Obradors, and, J. Rodriguez-Carvajal, Phys. Rev.B, 51, 6594, (1995).

[26] S. Kimura, H. Ohta, S. Mitsudo, M. Motokawa, W. L. Jang, M. Hasegawa and H. Takei, J.Phys.:Condens. Matter, 8, 5461-5473, (1996).

[27] B. Lebech, Y. Matsuoka, K. Kakurai and M. Motokowa, Progress of the Theoretical Physics Supplement, 150, 222, (2005).

[28] E. Stryjewski and N. Giordano, Advances in Physics, 26, 487, (1977).

[29] M. Motokawa, K. Kita, H. Shibazaki, H. Ohta, W.J. Jang, M. Hasegawa, and H. Takei, Physica B, 211, 165, (1995).

[30] International Tables for Crystallography, Vol. D, Physical Properties of Crystals, Edited by A. Authier, Kluwer Academic Publishers, (2003).

[31] T. Arima *et al.*, Phys. Rev. B, 70, 064426, (1980).

[32] G. Knebel, P. Lunkenheimer, A. Loidl, G. Wltschek, and H. Fuess, Journal of Alloys and Compounds, 216, 99-103, (1994).

[33] G. A. Samara, and J. F. Scott, Solid State Communications, 21, 167-170, (1977).

[34] A.P. Litvinchuk, M.N. Iliev, V.N. Popov and M.M. Gospodinov, J. Phys.: Condens. Matter, 16, 809, (2004).

[35] D. Fausti, A. A. Nugroho, P. H. M. van Loosdrecht, S. A. Klimin, M. N. Popova, and L. N. Bezmaternykh, Phys. Rev. B 74, 024403 (2006).

[36] D.L.Fox, D.R. Tilley, J.F.Scott and H.J. Guggenheim, Phys. Rev.B, 21, 2926, (1980).

[37] Z.V. Popovic, C. Thomsen, M. Cardona, R. Liu, G. Stanisic, and W. Konig, Z. Phys. B-Condensed Matter 72, 13, (1988).

[38] T. Katsufuji and H. Takagi, Phys. Rev.B, 64, 054415, (2001).

[39] A. A. Nugroho, N. Bellido, U. Adem, G. Nenert, Ch. Simon, M. O. Tija, M. Mostovoy, and T. T. M. Palstra, Phys. Rev. B, 75, 174435, (2007).

[40] M. S. Seehra and R. E. Helmick, J. Appl Phys. 55, 2330, (1984).

[41] D. L. Fox, D. R. Tilley, J. F. Scott, and H. J. Guggenheim, Phys. Rev. B 21, 2926, (1980).

[42] B. Lorenz, A. P. Litvinchuk, M. M. Gospodinov, and C. W. Chu, Phys. Rev. Lett. 92, 087204, (2004).

[43] O. P. Vajk, M. Kenzelmann, J. W. Lynn, S. B. Kim, and S.-W. Cheong, Phys. Rev. Lett. 94, 087601 (2005).

[44] T. Kimura, S. Kawamoto, I. Yamada, M. Azuma, M. Takano, and Y. Tokura, Phys. Rev.B, 67, 180401, (2003).

[45] R. Tackett, G. Lawes, B. C. Melot, M. Grossman, E. S. Toberer, and R. Seshadri, Phys. Rev.B, 76, 024409, (2007).

[46] J. L. Garcia-Munoz, J. Rodriguez-Carvajal, and X. Obradors, Journal of Magnetism and Magnetic Materials, 104-107, 617, (1992).

[47] V. V. Moshchalkov, N. A. Samarin, Y. Zoubkova and B. V. Mill, Physica B, 163, 237, (1990).

[48] J. L. Garcia-Munoz, X. Obradors, and, J. Rodriguez-Carvajal, Physica B, 194-196, 277, (1994).

[49] R. Szymczak, H. Szymczak, M. Baran, R. Z. Levitin, and B. V. Mill, Journal of Magnetism and Magnetic Materials, 157-158, 667, (1996).

CHAPTER 4

Magnetodielectric coupling in Hexagonal Manganites

4.1. Introduction to Hexagonal Manganites: Crystal Structure

$YMnO_3$ is a member of the multiferroic hexagonal manganites family $RMnO_3$ (R = rare-earth or Y) that exhibits both magnetic order ($T_N \sim 75$ K) and a spontaneous, reversible electric polarization ($T_C \sim 1000$ K). The ferroelectric properties of $YMnO_3$ were first studied in the 1960's in the pioneering work of Bertaut *et al*. [1]. Soon afterwards, Smolenskii and Bokov reported the magnitude of the spontaneous polarization as 5 μC/cm^2 [2]. The existence of coupling between the ferroelectric and magnetic ordering was first suggested by the presence of an anomaly in the dielectric constant at T_N measured on polycrystalline $YMnO_3$ [3]. Recently, the interaction between the magnetic and ferroelectric states has been convincingly demonstrated by optical measurements [4], and a number of other studies have subsequently addressed the same topic [5–8]. The magnetoelectric coupling in $RMnO_3$ also forms the core of this chapter. However, we will first focus on the structural changes that occur when Y is replaced by different rare-earth cations and when Mn is replaced by Ga.

Little is known about the mechanism of the onset of the ferroelectric state in $YMnO_3$. A number of high temperature structural studies have been performed but these were unable to resolve the atomic displacements that occur below T_C [9–11]. Nevertheless, recent room temperature (RT) crystallographic studies coupled with band structure calculations have shown that the ferroelectric state is stabilized by buckling and tilting of the MnO_5 bipyramids [11–13]. The ferroelectric state is also associated with displacements of the Y^{3+} cations, which formally have a d^0-state, and the

oxygen ions that coordinate them. The two capping O^{2-} ions of the YO_8 capped trigonal antiprisms are displaced, yielding long and short Y-O bonds. The crystal structure of $YMnO_3$ is shown in Fig. 4.1.

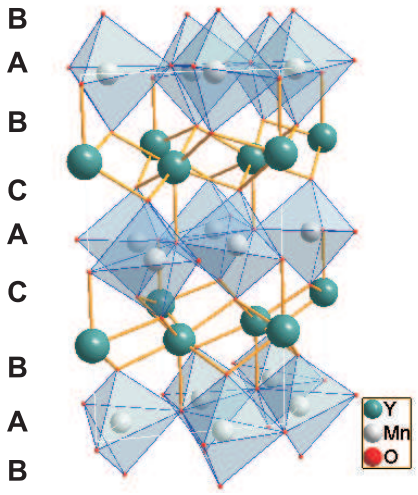

Figure 4.1: *Crystal structure of $YMnO_3$.*

The structure can be envisaged in several different ways. It can be considered as layers of MnO_5 trigonal bipyramids that are separated by layers of Y^{3+}. Alternatively, it can be constructed from chains of YO_8 bicapped trigonal antiprisms along c, where the Mn^{3+} cations are located between the capping oxygens. The apical oxygens of the MnO_5 bipyramids also construct the YO_6 antiprisms, and the axial oxygens of the MnO_5 bipyramids also constitute the caps of the YO_6 antiprisms. The crystal structure can also be pictured in terms of alternating hexagonal and cubic closed-packed oxygen layers in a BABCACBAB sequence. The Mn^{3+} ions are located in the "A" layer of a "hexagonal" BAB unit, yielding the bipyramidal coordination. The Y^{3+} ions occupy the octahedral holes in a "cubic" ABCA unit, where the B and C layers provide the antiprismatic coordination and the A layer provides the capping oxygens.

4.2. Structural Changes related to Ferroelectricity in Hexagonal Manganites

The changes in the crystal structure of RMnO$_3$ that occur with temperature, both in the high and low-temperature regions, have been studied in Refs. [9, 11, 12, 14, 15]. In this section, we will refer to previous crystallographic work on materials with R = Y, Yb and Lu, and we will use the crystallographic data to study trends in the structural parameters that are related to ferroelectricity. We will also use our own crystallographic data for $Yb_{0.5}Y_{0.5}MnO_3$, which has an average rare-earth

ionic radius close to that of Er. (A $Yb_{0.5}Y_{0.5}MnO_3$ single crystal was grown using the method as described in section 2.1). For conventional perovskite ferroelectrics, the electric dipoles originate in part from the cooperative, off-center displacement of transition metal cations. This displacement requires formally empty d-orbitals [16]. However, in $RMnO_3$ the d-orbitals of Mn^{3+} are partially occupied and the conventional mechanism for ferroelectricity does not apply. It has been shown by Van Aken *et al.* [12]. that the ferroelectricity is associated with the tilting of the MnO_5 bipyramids, resulting in oxygen displacements along the *c*-axis. These displacements also affect the coordination in the YO_8 polyhedra, as one of the capping oxygen ions is shifted "up" and the other is shifted "down" along the *c*-axis [See Fig. 4.2(a)].

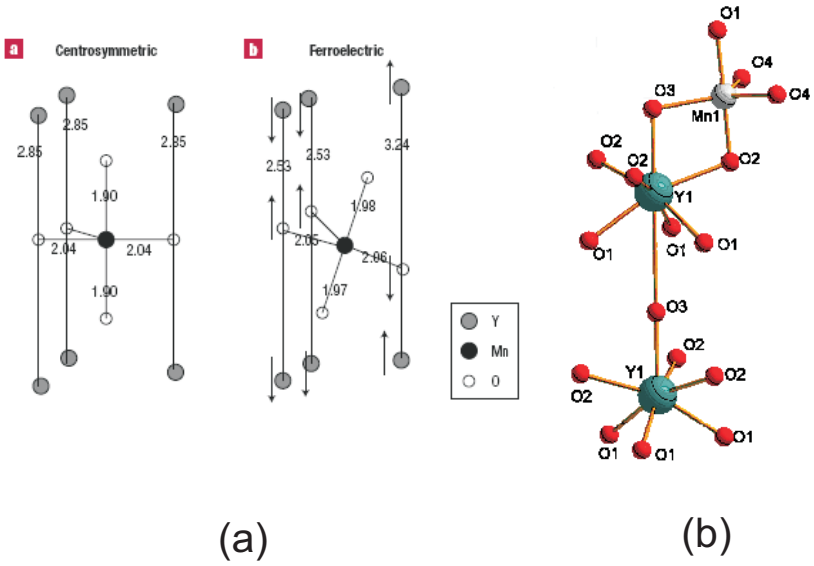

Figure 4.2: *(a) Displacements in the coordination of Y and O ions, resulting in a dipole moment (reproduced from [12]). (b) A view of Mn and Y coordinations, showing the different oxygen atoms.*

We will first focus on the structural changes that occur as the *R* cation is varied. As the ionic radius of *R* decreases from Y to Lu, the lattice parameters *a* and *c* both decrease accordingly (Fig. 4.3). The in-plane Mn-O bond distances also decrease slightly from Y to Lu, which gives rise to stronger magnetic exchange interactions and higher magnetic ordering temperatures [9]. The decrease in the *a* parameter is reflected more in the Mn-O4 bond length than in Mn-O3 [For a view of Mn and Y coordinations, see Fig. 4.2(b)]. The Mn-O bond distances are listed in Table 4.1 for different *R*.

The ferroelectricity largely originates from the relative shifts of *R* and O atoms due to the buckling and tilting of the MnO_5 polyhedra.The buckling is defined by the angle β between the plane formed by the base of the MnO_5 bipyramid, the O4-O4-O3 plane, and the *c*-axis. In Fig. 4.4 we

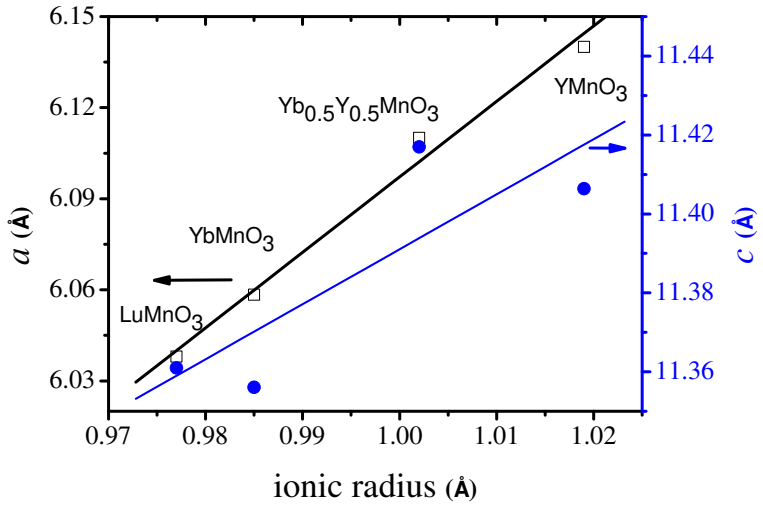

Figure 4.3: *Lattice parameters vs. ionic radius for $RMnO_3$ (R = Y, $Y_{0.5}Yb_{0.5}$, Yb and Lu).*

R	Y	Y,Yb	Yb	Lu
Mn-O1	1.858(7)	1.887(10)	1.867(7)	1.862(7)
Mn-O2	1.876(7)	1.883(10)	1.868(7)	1.859(7)
Mn-O3	2.054(3)	2.073(3)	2.039(4)	2.050(5)
Mn-O4	2.062(2)	2.043(2)	2.034(3)	2.019(3)

Table 4.1: *Mn-O bond distances (Å) for $RMnO_3$ at 293 K obtained from single crystal X-ray diffraction.*

show that β increases as the ionic radius of R decreases.

Therefore, one may expect that the displacements of the R cations increase as their ionic radius decreases, giving a larger ferroelectric distortion. This means that the short R1-O3 and R2-O4 bonds should decrease while the long bonds increase (changes in the c-axis are small [17]). The long and short R1-O3 bond lengths calculated from the published data follow the expected trend (Fig. 5).

The changes in the R-O bond lengths with ionic radius should also be reflected in the dipole moments associated with the displacements of the rare-earth ions. The dipole moments can be quantified by the distance from R to the center of gravity of the coordinating oxygens. All eight oxygens coordinating each R cation were taken into account. The general trend is that the dipole moments associated with both R1 and R2 increase as the ionic radius decreases (Fig. 4.6). The multiplicity of the R2 site is twice that of the R1 site and the local dipole moments of R1 and R2 have opposite sign. The z-coordinates of R1 and O3 are plotted in Fig. 4.7. We observe that the O3 ions shift to a greater extent as the ionic radius changes and are largely responsible for the change in the R1-O3 bond lengths. This provides further evidence that the ferroelectric distortion is mainly linked with the buckling and tilting of the trigonal bipyramid.

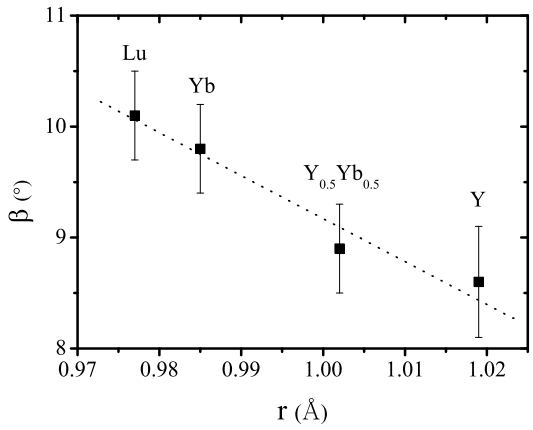

Figure 4.4: *Change of bipyramidal buckling angle with ionic radius of rare-earth ion; the line is guide to the eye.*

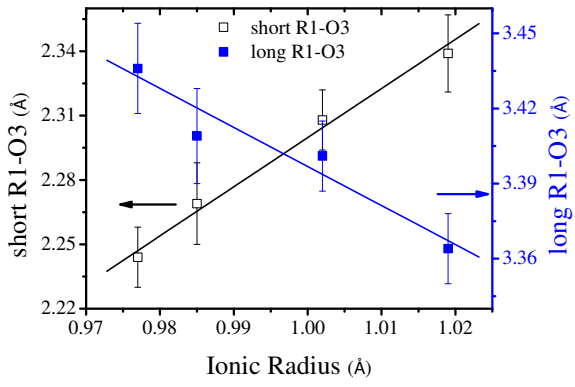

Figure 4.5: *Change of long and short R1-O3 bond lengths with ionic radius of R.*

We note that it is difficult to compare these predictions from our structural study with the experimental ferroelectric transition temperatures within the hexagonal manganites family since a systematical study of T_C's has not been done.

4.3. Ferroelectric displacements in multiferroic Y(Mn,Ga)O_3

4.3.1. Introduction

Isostructural compounds with the same space group as $YMnO_3$, $P6_3cm$, are also predicted and reported to be ferroelectric (for an overview, see for example Ref. [18]). Y can be replaced by small rare-earth ions and Mn can be substituted by Ga and In. $YGaO_3$ is one of these isostructural ferroelectric compounds [19]. The replacement of Mn by Ga results both in a change of the orbital occupation (from d^4 to d^{10}) and ionic radius at the bipyramidal site. The evolution of the structural parameters from $YMnO_3$ to $YGaO_3$ provides a better understanding of the origin of ferroelectricity in these hexagonal systems.

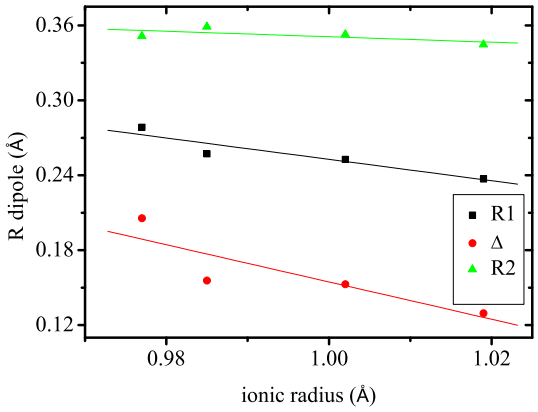

Figure 4.6: *Change of dipole moments associated with R1 and R2 with ionic radius of R, as well as the net dipole moment, Δ defined as 2R2-R1.*

Moreover, while theoretical analysis predicts that both the largest local dipole moment and T_C should decrease with Ga substitution [18], recent experimental work has shown that T_C increases [20]. Therefore, it is of interest to study the crystallographic response of $YMnO_3$ to Ga substitution.

The substitution of Mn by Ga is expected to have two effects. First, the fully occupied d_{z^2} orbital of Ga is expected to lengthen the apical Mn-O bond, which should decrease the tilt angle and thus the local dipole moments. Second, the smaller ionic radius of Ga^{3+} compared to Mn^{3+} increases the

relative radius of the *R* cation and should also result in a smaller degree of tilting. Furthermore, the *c*/*a* lattice parameter ratio is known to increase with Ga substitution; by analogy with the changes that occur on varying *R*, one may also expect this to be associated with decreased buckling and tilting of the bipyramids. However, we will show that this is not the case; rather, the coordination of Y^{3+} by the antiprismatic oxygens contributes significantly to the structural changes. We have obtained structural data for $YMn_{1-x}Ga_xO_3$ with x=0, 0.1, 0.3, and 0.5 at 100 K. We use the literature data for $YMnO_3$ [21] and $YGaO_3$ [19] at RT as reference.

4.3.2. Experimental

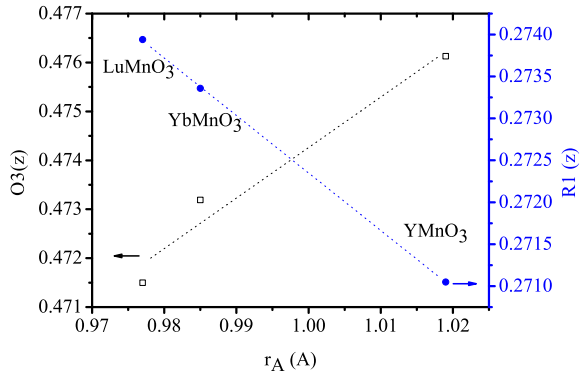

Figure 4.7: *Change of z fractional coordinates of R1 and O3 with ionic radius of R.*

$YMn_{1-x}Ga_xO_3$ (x = 0, 0.1, 0.3, 0.5) crystals were grown using a floating zone furnace (Crystal Systems Inc.). The oxygen partial pressure was increased with increasing Ga concentration in order to stabilize the molten zone. The crystals had a diameter of 5 mm and lengths of a few cm. Single crystal X-ray diffraction (SXRD) experiments were carried out on small chipped off crystal pieces at 100 K. Structural refinements included not only the atomic positions and displacement factors but also the site occupancies. Full occupation of the Y and O sites was observed, but small deviations from the nominal values of the (Mn,Ga) occupation were obtained. Nevertheless, we use the nominal compositions in our subsequent analysis. The room-temperature structural data for $YMnO_3$ were obtained on Bi_2O_3 flux-grown crystals [21]. The room-temperature structural parameters of $YGaO_3$ were taken from the work of Geller *et al*. [19], in which polycrystalline $YGaO_3$ was synthesized by inductive melting. The lattice parameters of the Ga-doped samples were obtained from powder X-ray diffraction (PXRD) on crushed single crystals.

4.3.3. Results and Discussion

In the previous section, we investigated the influence of the rare-earth ion on the structural parameters by summarizing previously reported work [17, 22]. We showed that for smaller R^{3+} ionic radii, the tilting and buckling of the bipyramids increases, leading to larger local dipole moments. Here, we focus on the role of the bipyramidal-site cation. First, Ga^{3+} has a smaller ionic radius than Mn^{3+} due to its larger nuclear charge. Second, Ga^{3+} has a d^{10} configuration, in contrast to the d^4 configuration of Mn^{3+}. We note that Mn^{3+} is not Jahn-Teller active in trigonal bipyramidal coordination, because the highest-energy d_{z^2} level is non-degenerate [23]. The lowest-energy orbitals are d_{xz} and d_{yz}, followed by degenerate d_{xy} and $d_{x^2-y^2}$ orbitals, while the d_{z^2} orbital is unoccupied.

Fig. 4.8 shows the lattice parameters as a function of doping for $YMn_{1-x}Ga_xO_3$. The change in lattice parameters is approximately linear from $YMnO_3$ to $YGaO_3$, obeying Vegard's law. The decrease in the a parameter can be explained by the smaller ionic radius of Ga. One may expect that the increase in the c parameter is due to the filling of the d_{z^2} antibonding orbital. However, we will show below that the Y-coordination is mainly responsible for the structural changes.

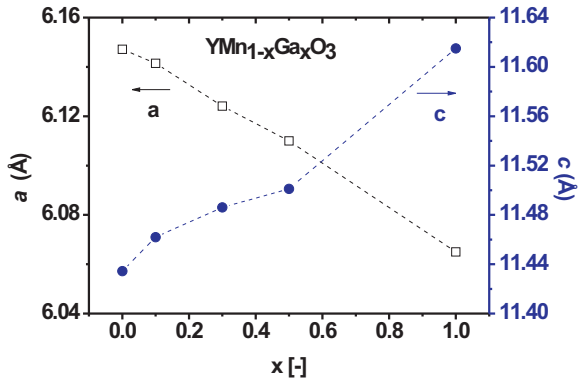

Figure 4.8: *Lattice parameters, a and c, of $YMn_{1-x}Ga_xO_3$ at RT from PXRD data.*

We list the Mn-O bond lengths in Table 4.2. The apical Mn-O bond lengths (Mn-O1 and Mn-O2) are significantly shorter than the planar Mn-O3 and Mn-O4 bond lengths. Our structural data indicate that the apical Mn-O distances do not change upon Ga substitution, at least not proportionally with the lattice parameter c. Therefore, the occupation of the antibonding d_{z^2} orbital has no noticeable effect on the apical Mn-O bond length.

In contrast, the Y-coordination does change with doping. In Fig. 4.9 we show the average distance between Y and the planes containing the coordinating O1 and O2 ions. The O1 ions all have the same z-coordinate by symmetry and the same is true for the O2 ions. The O1 (O2) ions are thus located in a plane perpendicular to the c-axis. The average distance of Y1 (Y2) to the

x	0 (from Ref. [21])	0	0.1	0.3	0.5	1 (from Ref. [19])
Mn-O1	1.858(7)	1.8610(7)	1.915(16)	1.866(12)	1.851 (9)	1.8403(17)
Mn-O2	1.876(7)	1.8950(7)	1.852(17)	1.875(12)	1.903 (12)	1.8416 (17)
Mn-O3	2.054(3)	2.0790(2)	2.086(5)	2.060(4)	2.062 (4)	2.0563 (11)
Mn-O4	2.062(2)	2.0494(12)	2.053(3)	2.047(3)	2.0406(18)	2.0172(9)

Table 4.2: *Mn-O bond distances (Å) in $YMn_{1-x}Ga_xO_3$ at 100 K obtained from SXRD data and at 293 K for x = 0 (SXRD) and 1.0 (PXRD).*

O1 and O2 planes increases by 6 % upon substitution of Mn^{3+} by Ga^{3+}. This indicates that a significant elongation of the YO_6 antiprism occurs with doping. Therefore, the increase in the *c* lattice parameter with Ga^{3+} content is not caused by the change in coordination of Mn^{3+}, but by the change in coordination of Y^{3+}. Likewise, the substitution does not significantly change the planar Mn-O3 and Mn-O4 distances, nor the O1-O1 and O2-O2 distances. This suggests that the changes in crystal structure are mainly associated with changes in the coordination of Y^{3+}.

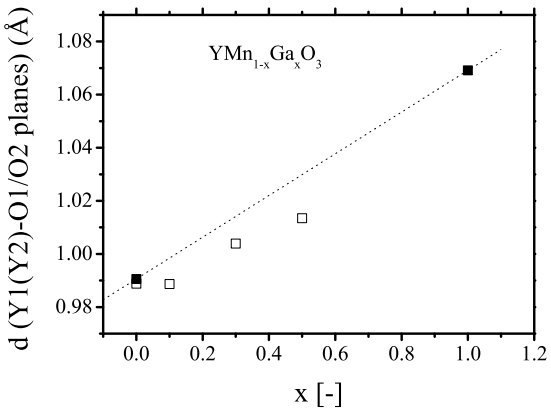

Figure 4.9: *Average distance between Y1 (Y2) and O1 (O2) planes as a function of Ga concentration. Filled squares denote data at 293 K, open squares denote data at 100 K. The line is a guide to the eye.*

We define the pyramidal tilt angle, α, as the angle between the apical O1-O2 axis of the MnO_5 bipyramid and the *c*-axis. The buckling is defined as the angle β between the plane formed by the base of the MnO_5 bipyramid, the O4-O4-O3 plane, and the *c*-axis. The changes in α and β as a function of doping are shown in Fig. 4.10. While the error bars are substantial, the data indicate that the tilting and buckling of the MnO_5 bipyramids do not change significantly upon Ga-substitution. This is in contrast to the effect of substitution on the A-site, where the tilting angle α decreases by 17 % for an increase in ionic radius of approximately 4 % (based on data for R=Y,Yb and Lu).

We can now relate these changes in the crystal structure to the changes that occur in the local dipole moments. As is the case for Mn in undoped $YMnO_3$, the substituted Ga remains in the

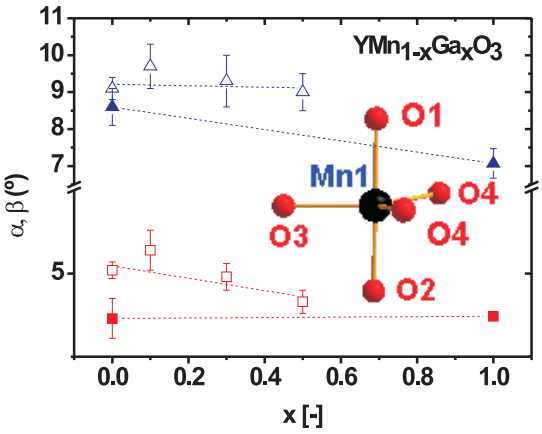

Figure 4.10: *Tilting angle α (squares) and buckling angle β (triangles) as a function of Ga concentration. Filled symbols denote values at 293 K, and unfilled symbols denote values at 100 K.*

barycenter of the bipyramids. Previously, we emphasized that the local dipoles associated with Y originate from the unequal displacements of the capping oxygen ions of the YO_6 antiprisms. One capping oxygen, O3 (O4), is almost the same distance from Y1 (Y2) as the antiprism oxygens ($\sim$ 2.3 Å), which corresponds approximately to the sum of the ionic radii of Y^{3+} and O^{2-}. However, the other capping oxygen lies approximately 1 Å further away. We note that the local dipole largely originates from the non-centered antiprismatic coordination of Y^{3+} and only to a lesser extent from the capping oxygens. In Fig. 4.11 we show the local dipoles associated with Y1, resulting firstly from the $Y1O_6$ antiprism only and secondly from the $Y1O_8$ capped antiprism, as a function of doping. The local dipole moments were defined as the distance from Y1 to the center of gravity of the 6 (8) oxygen ions. The local Y1 dipole clearly decreases upon Ga-substitution. The small difference between the local dipoles resulting from the $Y1O_6$ and $Y1O_8$ coordinations indicates that the antiprismatic oxygens contribute most to the local dipole moment.

While our structural studies indicate that Ga substitution decreases the local dipole moments associated with Y, the effect on the net polarization is less clear, given that the multiplicity of the Y2-site is twice that of the Y1-site and that the local dipole moments have opposite sign. Subtraction of the antiparallel displacements with appropriate multiplicity reveals that no significant change of the total dipole should occur upon Ga substitution (Fig. 4.12). Abrahams associates the ferroelectric transition temperature with the magnitude of the largest local dipole [18]. This approach predicts a reduction of the ferroelectric transition temperature with Ga substitution from 1220 K for $x = 0$ to 1020 K for $x = 1$. In contrast, Zhou *et al.* report an increase of the ferroelectric transition temperature from 900 K for $YMnO_3$ to 925 K for $YMn_{0.8}Ga_{0.2}O_3$ [20]. This indicates that understanding

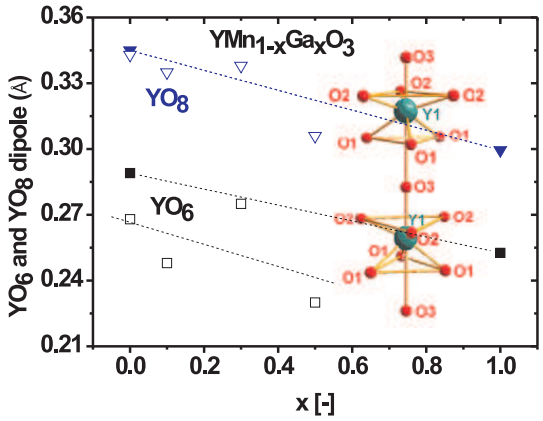

Figure 4.11: *Local dipoles associated with Y1, arising from the $Y1O_6$ antiprisms (squares) and $Y1O_8$ capped antiprisms (triangles), for $YMn_{1-x}Ga_xO_3$. Filled symbols denote values at 293 K and unfilled symbols denote values at 100 K.*

the coupling between the local dipoles is also important in order to explain the structural effects associated with Ga substitution. The relatively small changes in the crystal structure that occur with Ga substitution are in contrast to the very large changes in magnetoelectric coupling (see section 4.7.1).

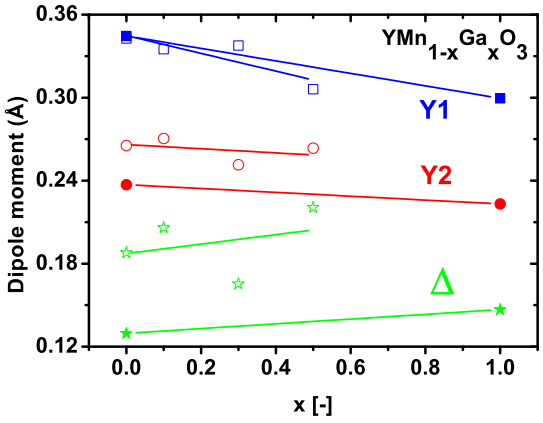

Figure 4.12: *Local dipole moments associated with Y1 (squares), Y2 (circles), and Δ (2Y2-Y1) (stars) for $YMn_{1-x}Ga_xO_3$, as defined in the text. Filled symbols denote values at 293 K and unfilled symbols denote values at 100 K.*

4.3.4. Conclusions

We have studied the structural response of single crystal $YMnO_3$ upon substitution of Mn^{3+} by Ga^{3+}. Substitution decreases the lattice parameter a and increases c. The smaller ionic radius and filled d_{z^2} orbital of Ga^{3+} were expected to change the local coordination of the Mn-site. This was not the case. Instead, we observed a much larger effect on the coordination of the Y-sites. Ga substitution results in an elongation of the YO_6 antiprisms, in which the Y-ions become located closer to the barycenter. Despite the decrease in local dipoles with doping, the net polarization does not decrease markedly because of the opposite signs of the $Y1O_6$ and $Y2O_6$ local dipoles. These results are in contrast to the substitution of Y by smaller*R*-cations, where increased tilting and buckling of the MnO_5 bipyramids occurs. The substitution of Mn^{3+} by Ga^{3+} does not increase the tilting and buckling of the bipyramids.

4.4. Coupling of Electric and Magnetic Ordering in $YMnO_3$

4.4.1. Introduction

The main aim of much of the research presented in this thesis is to understand the magneto(di)electric coupling in hexagonal manganites. We have used magnetocapacitance measurements as a tool to achieve this aim.

At the time that our work was undertaken, there were four notable papers addressing the magnetoelectric coupling in hexagonal manganites. It was shown by Huang *et al.* [3] that there is a dielectric anomaly at the antiferromagnetic (AF) ordering temperature (T_N) in polycrystalline $YMnO_3$, which was interpreted as evidence of the indirect coupling of electric and magnetic order parameters, mediated by strain. We note that for $YMnO_3$ the linear magnetoelectric effect is not allowed by symmetry. The dielectric constant below T_N was shown to be little affected by the application of magnetic field. This can be explained by the large difference between the ferroelectric and magnetic ordering temperatures. Katsufuji *et al.* [22] have reported dielectric anomalies at T_N for $YMnO_3$, $YbMnO_3$ and $ScMnO_3$ single crystals; significant anisotropy in the dielectric behavior was observed. Sugie *et al.* [24] reported dielectric anomalies at T_N for crystals of other hexagonal manganites, and they also carried out pyroelectric current measurements under magnetic field. Another important observation was the presence of a sharp dielectric constant anomaly at the spin-reorientation temperature for $HoMnO_3$ single crystals. Lorenz *et al.* obtained the magnetic phase diagram of $HoMnO_3$ from magnetocapacitance measurements [6].

The magnetic interactions in $RMnO_3$ are frustrated due to the triangular spin structure formed by the Mn spins lying in the ab basal plane (See Fig. 4.13). Evidence for magnetic frustration is given

by the ratio of the Weiss temperature (obtained by performing a Curie-Weiss (CW) fit to the inverse susceptibility) to T_N [25], which is approximately 10 when *R* is diamagnetic. The ratio is smaller for magnetic *R* cations due to the masking effect of the *R* magnetic moment [26]. The magnetic frustration gives rise to various possible Mn spin configurations, which cannot be distinguished by conventional neutron diffraction because the magnetic symmetries are homometric. However, the magnetic configurations have been determined using second harmonic generation experiments. Due to the interactions between the Mn 3d and *R* 4f spins, the magnetic phase diagrams are complex and differ significantly within the $RMnO_3$ family, as we discuss in Section 4.4 of this chapter.

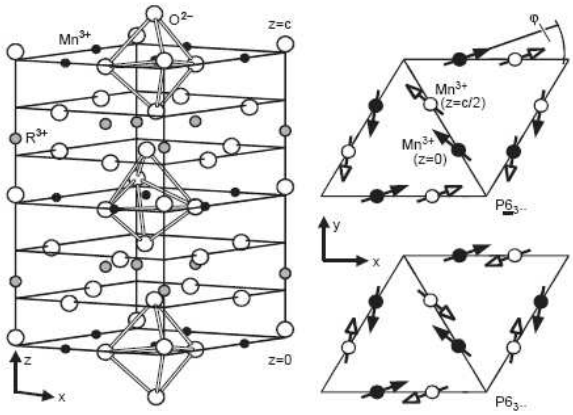

Figure 4.13: *Crystallographic and magnetic unit cell of $RMnO_3$ from Ref. [27].*

We have followed different lines of approach to study the magnetodielectric coupling in hexagonal manganites. We first established the nature of the magnetodielectric coupling in $YMnO_3$ and used Landau theory to model it (this section). We then studied $YbMnO_3$ (section 4.5) and $ErMnO_3$ (section 4.6) to see how different phases in the complex magnetic phase diagrams are reflected in the dielectric constant. Finally, we investigated the effects of substituting Ga for Mn on the frustrated spin lattice and the magnetodielectric coupling (section 4.7).

For the sake of clarity, we will summarize that will be used in the rest of the chapter; for more details, see Chapter 1. Throughout this thesis, we apply magnetic field to our samples and measure the capacitance in order to study the magnetoelectric coupling between the electric and magnetic order parameters. To the best of our knowledge, it was first suggested by Lawes *et al.* [28], who refer to the book by Landau and Lifshitz [29], that the term "magnetoelectric" should be reserved for materials of particular symmetries where a free energy invariant proportional to PM is allowed (P and M are order parameters for electrical polarization and magnetization, respectively). Lawes *et al.* introduced the term "magnetodielectric effects" to describe cases in which "more general coupling" occurs. Indeed, this terminology has been applied to many systems, especially for those for which the linear magnetoelectric coupling is forbidden by symmetry. Accordingly, we will use the term

"magnetodielectric coupling" instead of "magnetoelectric coupling" for systems that do not allow the linear magnetoelectric effect by symmetry. This is the case for the hexagonal manganites, in which only non-linear coupling mediated by strain can be considered.

4.4.2. Temperature-dependent Capacitance and Magnetization Measurements for $YMnO_3$

Fig. 4.14 shows the temperature dependence of the magnetic susceptibility of a $YMnO_3$ crystal oriented in the *ab*-plane and along the *c*-axis. We observe a clear cusp in χ_c at T_N = 73 K, while χ_{ab} presents only a broad anomaly. This unusual anisotropy around T_N, departing from normal 2D antiferromagnet behavior, was reported earlier [22]. We note that for polycrystalline samples, it is difficult to define the magnetic ordering temperature from magnetization measurements [3]. The Weiss temperatures parallel and perpendicular to *c* were -542 K and -620 K, respectively showing that the anisotropy at temperatures other than close to T_N is negligible [3].

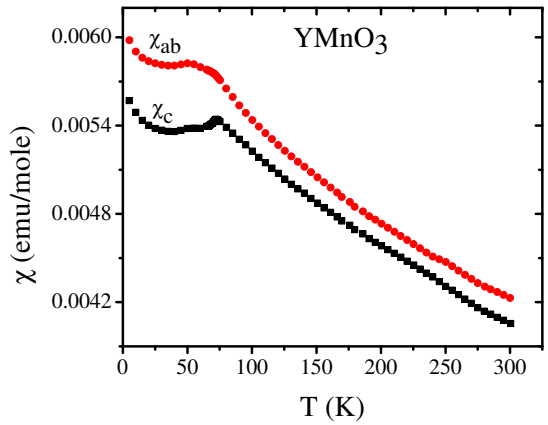

Figure 4.14: *Temperature dependence of magnetic susceptibility of $YMnO_3$ single crystal oriented in the ab-plane (circles) and along c (squares).*

In Fig. 4.15 the temperature dependence of the capacitance of $YMnO_3$ is shown. When the electric field was applied in the *ab* plane, a clear anomaly was observed at 72 K where AF ordering takes place. A smaller anomaly in the capacitance was also observed when the electric field was applied along the *c*-axis. The difference between the measured ab plane capacitance and the corresponding values extrapolated from the temperature dependence of the capacitance above T_N, fitted using a quadratic function, is proportional to L^2, where L is the antiferromagnetic order parameter. This is explained in section 4.4.3.

The existence of a dielectric anomaly at T_N has been known since the publication of Huang *et al.*

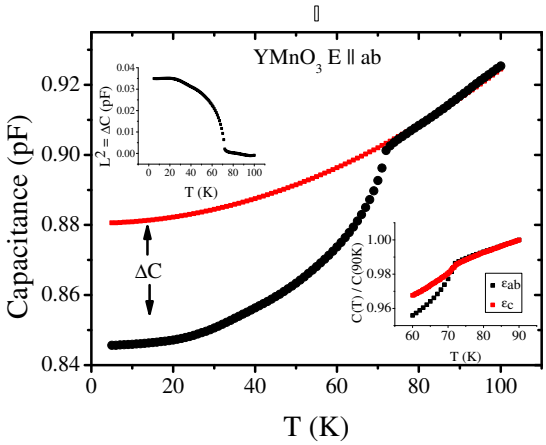

Figure 4.15: *Temperature dependence of capacitance of $YMnO_3$ when $E \parallel ab$ plane. The red line shows the extrapolated high-temperature behavior, obtained by fitting the data above T_N with a quadratic function. The left-hand inset shows the difference between the extrapolated and the measured capacitance, while the right-hand inset shows the anisotropic behavior of the capacitance.*

appeared in 1997 [3]. As explained in the cuprates chapter, this decrease of ε below T_N shows that magnetic ordering is coupled to a low-lying optical phonon, hardening it. However, since the magnetodielectric coupling is apparently small, the temperature-dependent capacitance measurements did not differ when a magnetic field was applied and it was concluded that the capacitance of $YMnO_3$ is not field-dependent.

However, measurement of the magnetic field dependence of the capacitance of $YMnO_3$ single crystals at constant temperatures gives a different conclusion. In this way, we eliminate the contribution from the temperature dependence of the capacitance itself, which allows us to measure the effect of the magnetic field only. We show magnetocapacitance (MC) (defined as $\frac{C(H)-C(0)}{C(0)}$) measurements at 5K for electric fields applied parallel and perpendicular to the easy plane (the *ab* plane) in Fig. 4.16. The magnetic field was applied parallel to *c* in both measurements. We observe that there is some dependence on field when the electrical contacts are placed along the *ab* plane, but not when they are placed along *c*. In the former case, the magnetic field dependence is quadratic.

MC measurements performed close to T_N are shown in Fig. 4.17. If the quadratic curves are fitted using the expression $y = a+bH^2$, the coefficient *b* first increases slowly from 69 K to 70.5 K, decreases abruptly at 71 K and then remains at a similar value at 72K. We will discuss similar behavior of MC around T_N for $YbMnO_3$ in section 4.5.3.

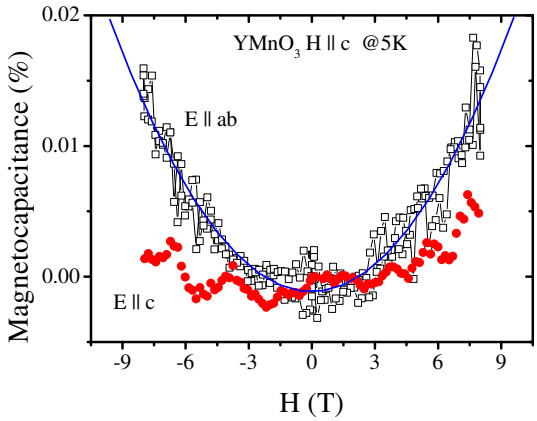

Figure 4.16: *Magnetocapacitance measurements at 5K for E ∥ ab plane (open squares) and E ⊥ ab plane (filled circles). H is ∥ c for both measurements. The thin line is a quadratic fit.*

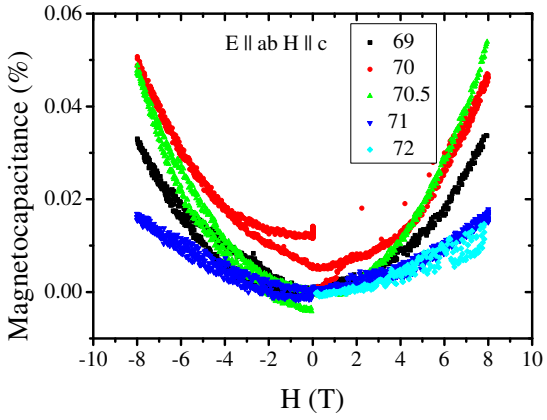

Figure 4.17: *Magnetocapacitance measurements for temperatures close to T_N = 74 K, E ∥ ab, H ∥ c.*

4.4.3. Discussion of Results and Landau Theory Description of Dielectric Anisotropy

The anisotropy in the dielectric anomaly, that is, the observation that the anomaly in ε_{ab}(T) is much more pronounced than that in ε_c(T), was first reported by Katsufuji *et al.* for $YMnO_3$ and $LuMnO_3$ single crystals [22]. This anisotropy was further evidenced by optical conductivity measurements, in which the low-frequency vibrational modes for light polarized perpendicular to c (E $\perp$ to c) display shifts (hardening) at T_N, showing that they are coupled to the spin system; for E $\parallel$ to c, the phonon spectrum shows only a thermal shift [5].

This large difference between the in-plane and out-of-plane magnetodielectric response is to a large extent the consequence of the anisotropy of ε itself, which can be understood by considering the thermodynamic potential of a ferroelectric antiferromagnet given by [30]:

$$\begin{aligned}\Phi &= \Phi_{\mathrm{FE}}(\mathbf{P})+\Phi_{\mathrm{AFM}}(\mathbf{L})-\mathbf{E}\cdot\mathbf{P}\\ &\quad+\frac{1}{2}[g_\perp(P_a^2+P_b^2)+g_\parallel P_c^2]L^2\\ &\quad+\frac{1}{2}[\gamma_\perp(P_a^2+P_b^2)+\gamma_\parallel P_c^2]H^2\\ &\quad+\frac{1}{2}[-\chi_m^{(0)}H^2+c_1L^2H^2+c_2\,(\mathbf{L}\cdot\mathbf{H})^2]. \qquad (4.1)\end{aligned}$$

In this equation the first two terms describe the ferroelectric and magnetic subsystems, the third term describes the coupling to the electric field, and the fourth term describes the coupling between the ferroelectric order parameter **P** and the AF order parameter **L** with in-plane and out-of-plane magnetodielectric coupling strengths $g_\perp$ and $g_\parallel$, respectively. The fifth term represents the coupling between **P** and a uniform magnetic field **H**, and the last term describes the isotropic magnetic energy as well as the magnetic anisotropy due to the AF ordering. The ferroelectric subsystem, described by Eq.(4.1), has uniaxial anisotropy, while the magnetic anistropy is weak, as shown in Fig. 4.14 [30].

To first-order approximation in the coupling constants, the changes of the longitudinal and transversal dielectric susceptibilities $\chi_\parallel$ and $\chi_\perp$ in the presence of AF ordering and an applied magnetic field can be written as $\Delta\chi_\parallel=\chi_\parallel(L,H)-\chi_\parallel(0,0)\approx-\chi_\parallel^2(0,0)\left(g_\parallel L^2+\gamma_\parallel H^2\right)$ and $\Delta\chi_\perp\approx-\chi_\perp^2(0,0)\left(g_\perp L^2+\gamma_\perp H^2\right)$, respectively. From these expressions, we show that when H = 0, the change we observe in Fig. 4.15 in the dielectric constant upon magnetic ordering is proportional to the term gL^2, i.e. the capacitance measurements allow us to access the antiferromagnetic order parameter, L. Moreover, the quadratic behavior of the MC shown in Figs. 4.16 and 4.17 originates from the term γH^2.

Thus, the ratio of the changes in the in-plane and out-of-plane dielectric constants that take place on magnetic ordering can be expressed as:

$$R=\frac{\Delta\varepsilon_\perp}{\Delta\varepsilon_\parallel}\approx\left(\frac{\varepsilon_\perp-1}{\varepsilon_\parallel-1}\right)^2\left(\frac{g_\perp L^2+\gamma_\perp H^2}{g_\parallel L^2+\gamma_\parallel H^2}\right). \qquad (4.2)$$

Because for $YMnO_3$ the dielectric constant $\varepsilon_\perp \simeq 21$ (transverse to the direction of the spontaneous polarization) is significantly larger than the longitudinal dielectric constant [30] $\varepsilon_\parallel \simeq 5$, the ratio of the anomalies at T_N is $R \approx 25 g_\perp / g_\parallel$, while the ratio of the MC values is $R \approx 25\gamma_\perp/\gamma_\parallel$. Furthermore, one expects that $g_\perp > g_\parallel$ and $\gamma_\perp > \gamma_\parallel$, because these coupling constants scale with the spin-exchange couplings in the corresponding directions (that is, the quasi-two-dimensional magnetic structure of $YMnO_3$ is an additional source of anisotropy in its magnetodielectric response). Thus, the anisotropy in the dielectric anomaly is a result of the anisotropy in the magnetic exchange interactions and the dielectric susceptibilities.

In summary, we have demonstrated that the previously reported anomaly in the dielectric constant at T_N is anisotropic; it is more pronounced when the electric field is applied parallel to the easy plane (the *ab* plane). This anisotropy can be accounted for using Landau theory, taking into account the magnetic anisotropy and the anisotropy in the dielectric constant itself. We have shown that the MC in $YMnO_3$, although small, is non-zero and behaves quadratically with respect to field. In order to measure this small MC, constant-temperature measurements must be performed in order to eliminate the dependence of the capacitance on the lattice and the magnetic order parameter. We have observed that the MC is also anisotropic, being larger when the electric field was applied in-plane. This was also explained using Landau theory, taking into account the anisotropy in the dielectric constant itself. We note that the coupling of the polarization P to the magnetic order parameter L must be differentiated from its coupling to the magnetic field H. The anomaly at T_N in the dielectric constant of $YMnO_3$ is rather strong, and when compared to other systems as shown in Table 4.3, this shows that the coupling to the AF order parameter is significant.

Compound	$\Delta\varepsilon/\varepsilon(\%)$	T_N
$YMnO_3$	0.085	74 [30]
MnF_2	0.025	67 [31]
$EuTiO_3$	1	5.5 [32]
$Y_2Cu_2O_5$	0.012	12 (this thesis)
$Er_2Cu_2O_5$	0.0062	28 (this thesis)

Table 4.3: *Comparision of the change of dielectric constant, $\Delta\varepsilon/\varepsilon$, upon magnetic ordering for various materials. $\Delta\varepsilon/\varepsilon$ is the approximate difference between the measured low-temperature value of ε and the corresponding extrapolated value according to the temperature dependence of the behavior above T_N, normalized by the magnetic ordering temperature.*

In contrast, the magnetic field dependence of the capacitance is so weak that it is difficult to measure. In conclusion, the magnitude of the magnetodielectric coupling is significant if we consider the coupling of L to P, that is, the dielectric anomaly below T_N. However, it is very small if we consider the coupling of P to H. We also note that the temperature dependence of the AF order parameter can be obtained from the temperature dependence of the capacitance. The fact that the magnetic contribution to the dielectric constant is proportional to the square of the sublattice magnetization

has been shown using a similar free energy approach for $BaMnF_4$ [33], as well as for MnO [34] and MnF_2 [31].

4.4.4. High magnetic field measurements

We have used high magnetic fields of up to 30 T to measure the MC of $YMnO_3$, which is shown at selected temperatures in Fig. 4.18. Broad peaks are present in all of the curves except for the measurement at 74 K. The intensity and width of the peaks decreases with heating, after remaining constant up to 26 K. For the 4.2 K and 10 K data only, the behavior at low fields is different from our previous lab measurements.

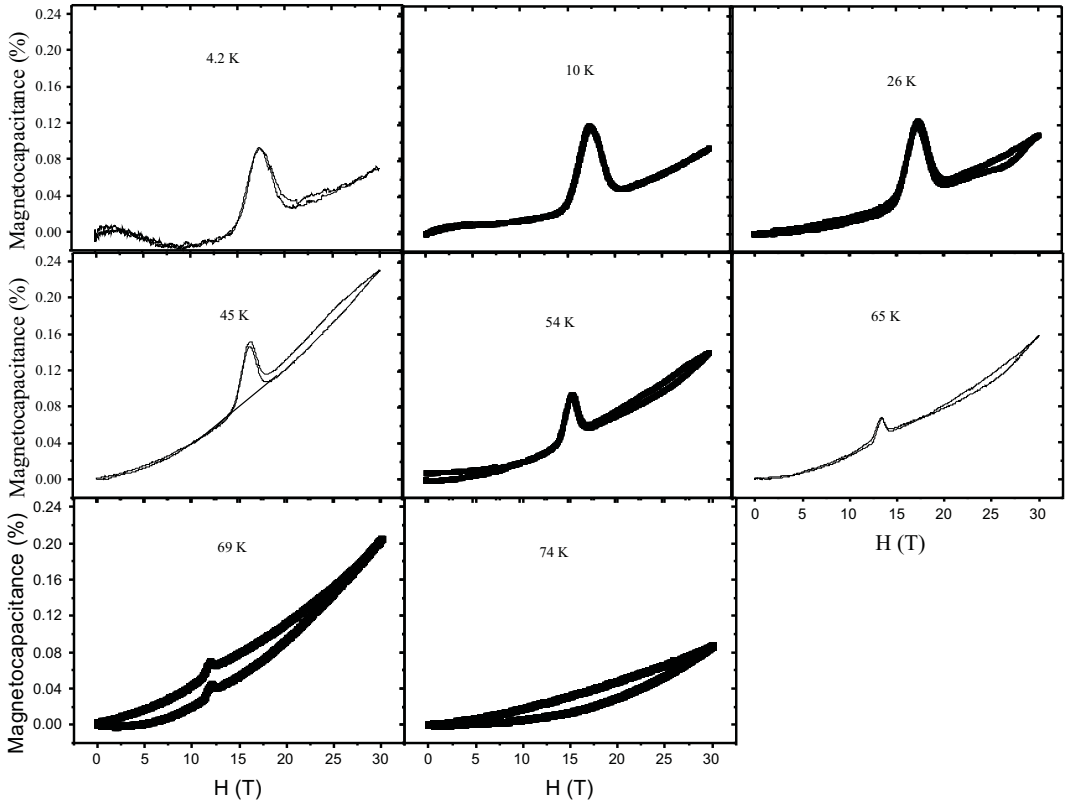

Figure 4.18: *Magnetocapacitance measurements of $YMnO_3$ up to 30 T at different temperatures, $E \parallel ab$, $H \parallel c$.*

From the anomalies in our MC measurements we were able to construct the following phase diagram (Fig. 4.19).

Fiebig *et al.* have mapped the magnetic phase diagrams for many members of the hexagonal RMnO$_3$ series, where R is a magnetic rare earth [35]. The magnetic phase diagram for $YMnO_3$ has not previously been reported. Fig. 4.20 shows the different magnetic symmetries that are possible for $RMnO_3$. It is reported that the ground-state symmetry of pure $YMnO_3$ is $P\underline{6}_3c\underline{m}$ (the so-called B1

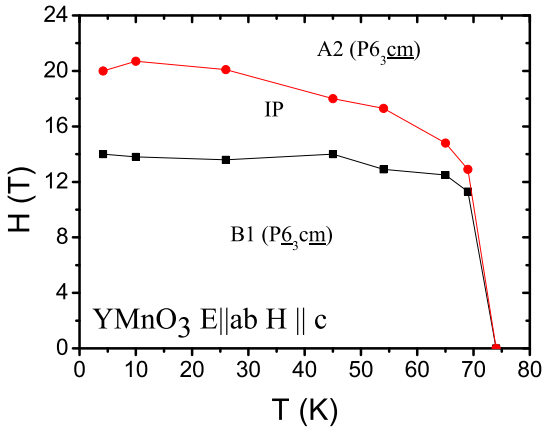

Figure 4.19: *Magnetic phase diagram of $YMnO_3$, $E \parallel ab$, $H \parallel c$.*

phase) [36]. Among the possible magnetic symmetries listed in the figure, only one allows a canting of the Mn-spins along the *c*-direction [37]. Because we apply the magnetic field along *c* in the MC measurements, it is very likely that the field stabilizes the phase with the weak FM component along *c*, which is the so-called A2 ($P6_3\underline{cm}$) phase. Thus, we suggest that the MC anomaly corresponds to a phase transition from the B1 to A2 phases. However, the anomalies in magnetocapacitance shown in Fig. 4.18 are quite broad, which suggests that the transition from B1 phase to the A2 phase occurs via an intermediate phase. Similar broad MC anomalies have previously been reported for $HoMnO_3$, and were also explained in terms of a phase transition that proceeded via an intermediate phase [6].

4.5. Magnetodielectric coupling in $YbMnO_3$

At the time that this investigation was started, in similar fashion to $YMnO_3$ little had been reported on $YbMnO_3$ regarding magnetodielectric coupling. It was shown by Sugie *et al.* that there is an anomaly in the dielectric constant at T_N [24]. Fiebig *et al.* determined the complex magnetic phase diagram of $YbMnO_3$ using optical techniques [35]; the magnetodielectric coupling strength is determined by the magnetic symmetry. We have explored the magnetodielectric coupling in $YbMnO_3$ using magnetocapacitance measurements, focusing in particular on the coupling close to T_N.

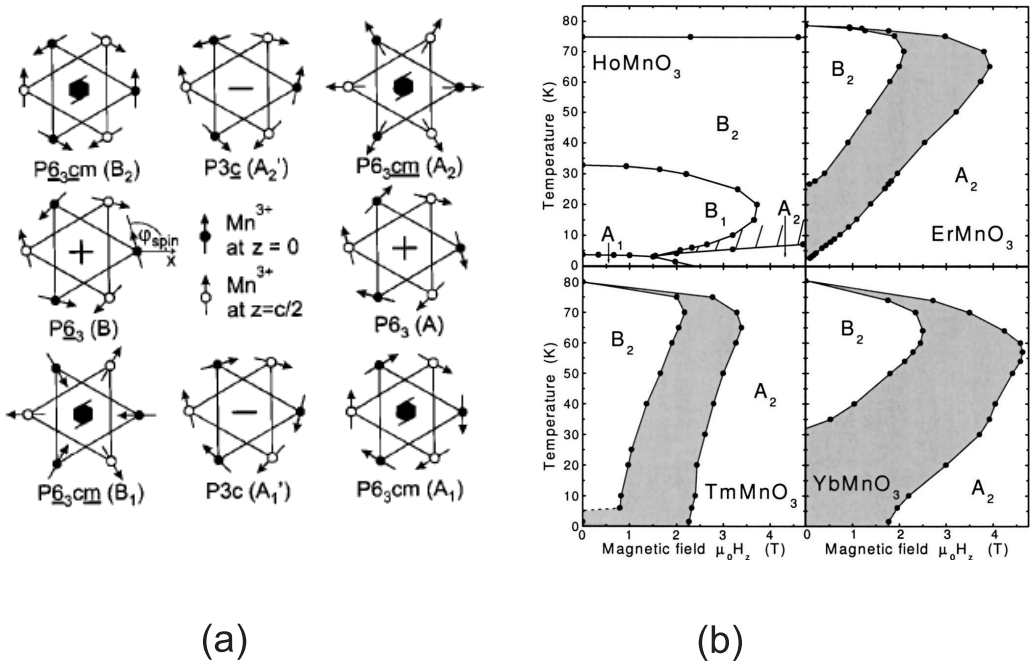

Figure 4.20: *Magnetic symmetries (a) and phase diagrams (b) of $RMnO_3$ from Fiebig* et al. *[35].*

4.5.1. Magnetic Structure

The magnetic structure of $YbMnO_3$ has been studied in detail by Tomuta using a combination of neutron diffraction, muon spin rotation, specific heat, and pulsed high-field magnetization techniques [38]. In addition to the Mn spins, which order in the *ab* plane at a temperature of 84 K determined by specific heat measurements, the presence of two magnetic Yb sublattices was shown. The Yb^{3+} cations occupy two different crystallographic sites, with Wyckoff positions 4(b) and 2(a). It was proposed that the Yb^{3+} spins on the 2(a) site order in ferromagnetic (FM) fashion while those on the 4(b) site order in AF fashion. Both of the Yb^{3+} spins lie parallel to the *z*-direction. The ordering temperature of the Yb spins on the 2(a) site was determined from specific heat measurements to be 3.8 K, while the Yb spins on the 4(b) start to order below 30 K [38].

4.5.2. Magnetization Measurements on $YbMnO_3$

It is difficult to detect any anomaly in the temperature-dependent magnetic susceptibility at T_N because the Yb paramagnetic moment masks the anomaly corresponding to the ordering of the Mn spins. Therefore, in Fig. 4.21 we have plotted χT vs T for a crystal oriented in the *ab* plane and parallel to *c*. A well-defined maximum is present at 84 K when the field is applied parallel to the *ab* plane. From the CW fit of the inverse susceptibility between 200 and 300 K, an effective moment of 6.86 μ_B is obtained, which is close to the theoretical value of 6.72 μ_B. The Weiss temperature

obtained from the fit was -203 K.

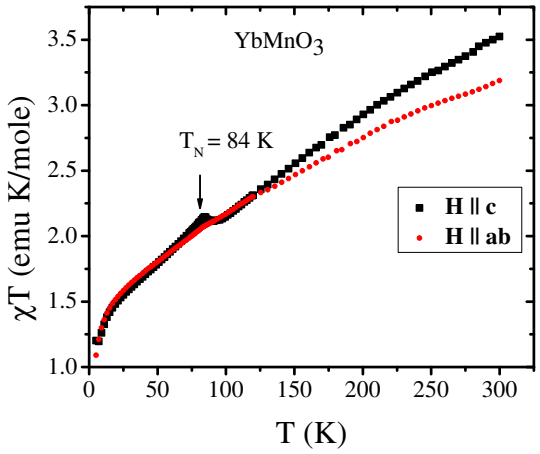

Figure 4.21: *Temperature dependence of magnetic susceptibility of $YbMnO_3$, circles denote measurements ∥ ab, squares ⊥ ab.*

The magnetic field dependence of the magnetization and the magnetic phase diagram will be discussed in the following sections.

4.5.3. Capacitance and Magnetocapacitance Measurements on $YbMnO_3$

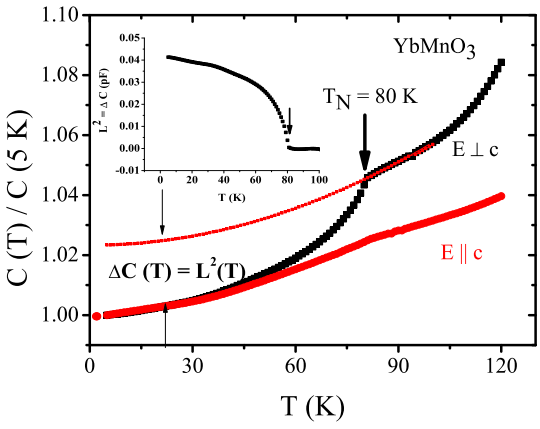

Figure 4.22: *Temperature dependence of the capacitance for E parallel and perpendicular to ab plane. The inset shows the square of the antiferromagnetic order parameter L^2, obtained from ΔC.*

Fig. 4.22 shows the temperature dependence of the capacitance measured parallel and perpendicular to the *c*-axis. The data are normalized to the 5K values for easier comparison. An anomaly below T_N is apparent for both crystal directions; however, it is more pronounced for ε_{ab}, similar to the case of $YMnO_3$. The magnetic contribution to the capacitance is reflected in the inset.

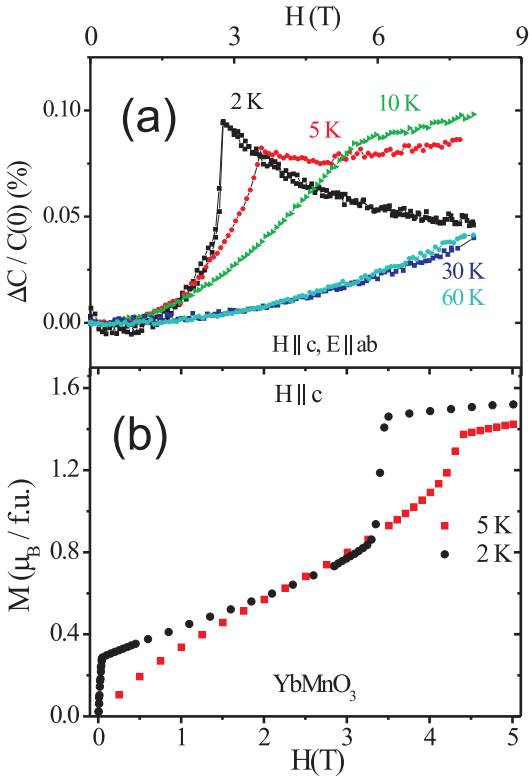

Figure 4.23: *(a) Magnetocapacitance of $YbMnO_3$ at $T < T_N$ for $E \| ab$-plane and $H \| c$; (b) Field dependence of magnetization at 2 and 5 K.*

Fig. 4.23(b) shows the magnetization as a function of field for H parallel to *c* at 2 K and 5 K. When the field is increased from zero at 2 K an abrupt change in the magnetization occurs at very low values of H. The magnetization then increases linearly with field, before another stepwise increase in the magnetization occurs at approximately 3T. At 5K, the first magnetization step is no longer present while the second step shifts to higher fields. The same behavior was previously reported by Tomuta [38] and Sugie *et al.* [24]. The first step was ascribed to the FM ordering of Yb 2(a) spins whereas the second step was suggested to result from a flip of the AF-ordered Yb 4(b) spins. Because the Yb 2(a) spins order only below 3.8 K from neutron diffraction [38], the first magnetization step is missing at 5 K.

Fig. 4.23(a) shows the magnetocapacitance. The magnetic field was applied along the *c*-axis

and the electrical field was applied in the *ab* plane. At 2 K, the MC initially increases with field before a rapid, almost discontinuous increase takes place at 3 T, which corresponds to the spin-flip transition observed in the magnetization measurements. At higher fields, the MC decreases steadily. At higher temperatures the transition becomes broader and the critical field for the transition increases. Between 30 K and 60 K, the magnitude of the MC follows the same field dependence, and we observe no anomaly up to 8 T.

We observed anomalous behavior in the MC close to T_N, as shown in Fig. 4.24(a). At 78 K, the MC is positive and quadratic up to approximately 7 T, where a downturn occurs. The onset of this downturn is shifted to lower fields as the temperature is increased towards T_N. Finally, at 80 K the MC becomes negative and large over the whole range of fields measured. When the temperature is further increased, the magnitude of the MC starts to decrease and it becomes positive again at 95 K. If vertical cuts at constant field are taken through Fig. 4.24(a) and $\frac{C(H)-C(0)}{C(0)H^2}$ is plotted as a function of temperature, it is remarkable that the data all lie on a single curve [see Fig. 4.24(b)]. At temperatures far from T_N the MC is rather small. As T_N is approached from below, the slope of the MC with respect to temperature becomes large and positive, before the MC exhibits a sharp, almost discontinuous jump from positive to negative values.

In the following discussion we show that the MC anomaly close to T_N is a result of competition between two antiferromagnetic states, one of which is weakly ferromagnetic. Hexagonal manganites are known to have a number of competing ordered magnetic phases [35]. In all of these phases the Mn spins are arranged in a 120°-structure on the triangular lattice in the *ab* planes. The orientation of the spins with respect to the crystallographic axes and with respect to the spins in neighboring layers varies from phase to phase, as does the configuration of the rare-earth spins [39–42]. The magnetic phase diagram of $YbMnO_3$, studied by a variety of different experimental techniques, contains the low-field B_2 phase (magnetic space group $P6_3\underline{c}m$) and the high-field A_2-phase (magnetic space group $P6_3\underline{cm}$) [26, 35]. The symmetry of the latter phase allows the presence of a net magnetization in the *c* direction (largely due to the rare-earth spins and therefore small near T_N), which is why the A_2 phase is stabilized by $H\|c$.

The competition between the A_2 and B_2 phases has been discussed in Ref. [43] using a phenomenological free energy expansion in two order parameters:

$$\begin{aligned} f &= \sum_{\gamma=\mathrm{A,B}} \left[\frac{\alpha_\gamma}{2} \left(T - T_\gamma^{(0)} + \lambda_\gamma H^2 \right) L_\gamma^2 + \frac{b_\gamma}{4} L_\gamma^4 \right] \\ &+ \frac{d}{2} L_\mathrm{A}^2 L_B^2 - H \left(\phi L_\mathrm{A} + \frac{\phi'}{3} L_\mathrm{A}^3 + \frac{\phi''}{2} L_\mathrm{A} L_\mathrm{B}^2 \right) \end{aligned} \tag{4.3}$$

Here, $L_\mathrm{A}(L_\mathrm{B})$ is the order parameter of the sublattice magnetization characterizing the $A_2(B_2)$ phase, H is the magnetic field along the *c* axis, and $T_\gamma^{(0)}$ is the temperature limit of stability for each phase.

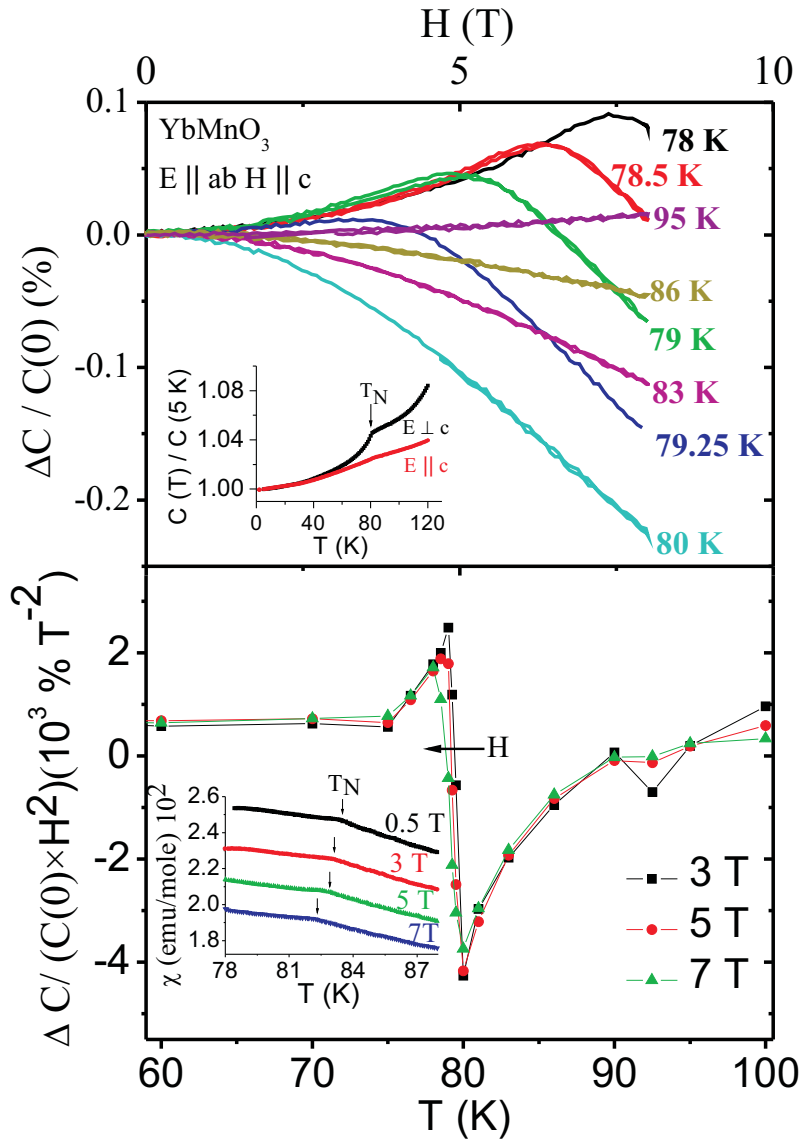

Figure 4.24: *(a) Magnetic field dependence of magnetocapacitance of $YbMnO_3$ single crystal at constant temperatures near T_N. The temperature dependence of capacitance is added as an inset. (b) Temperature dependence of magnetocapacitance at constant magnetic fields. The inset shows the shift of T_N in magnetic field obtained from magnetic susceptibility measurements. Electric field is parallel to the ab plane, while $H \| c$.*

The linear coupling of L_A to H corresponds to the spontaneous magnetization present in the A_2 phase.

A typical phase diagram for this model for $T_B^{(0)} > T_A^{(0)}$ (when the B2 phase is energetically more favorable than the A2 phase at zero field) is shown in Fig. 4.25 . Due to the linear coupling between H and L_A, the latter order parameter is non-zero for an arbitrarily weak magnetic field, so that for $H \neq 0$ a transition from the B_2 to A_2 phase occurs, resulting in some admixture of the A_2 phase always being present.

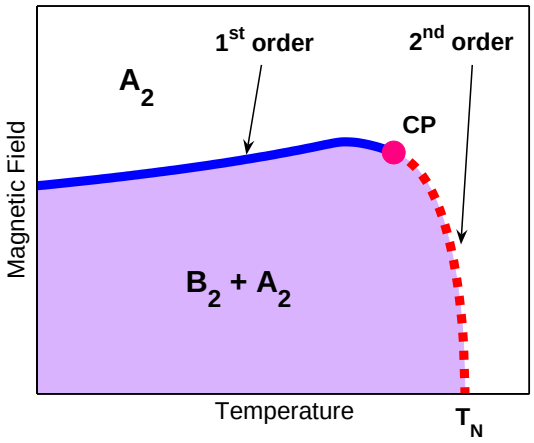

Figure 4.25: *The magnetic phase diagram described by Eq. 4.3 for $T_B^{(0)} > T_A^{(0)}$. The gray region is the B_2 phase with some admixture of the A_2 phase. The critical point (CP) separates the first-order transition (solid) line from the second-order transition (dashed) line [44].*

To describe the observed MC anomaly, we add to the free energy in Eq.(4.3) the coupling of the magnetic order parameters to the electric polarization P in the *ab* plane:

$$f_{me} = \frac{P^2}{2}\left(\sum_{\gamma=A,B} g_\gamma L_\gamma^2 + g'_A L_A H\right) \tag{4.4}$$

We also add the terms $\frac{P^2}{2\chi_e^{(0)}} - PE$ describing the dielectric response of the paramagnetic state. The MC anomaly obtained using this model [(see Fig. 4.26(a)] has the same shape as that observed for $YbMnO_3$ and obeys the observed scaling for weak fields. This behavior can be understood by noting that the main contribution to the magnetic field dependence of the dielectric susceptibility comes from L_A, which is linearly coupled to the magnetic field and which has an anomaly at T_N: $\Delta\chi_e \propto -L_A^2$. In the weak-field regime $L_A \propto H$ such that $\frac{\chi_e(T,H)-\chi_e(T,0)}{H^2}$ is approximately field-independent, which explains the observed scaling [45]. We note that for weak fields $\frac{\chi_e(H)-\chi_e(0)}{H^2} \approx -\frac{1}{2}\frac{\partial^4 f}{\partial H^2 \partial E^2}$, so the observed anomaly is an anomaly in the nonlinear magnetoelectric susceptibility, which also gives rise to an electric-field dependence of the magnetic susceptibility.

As H increases, the character of the transition in the two-parameter model changes: in low

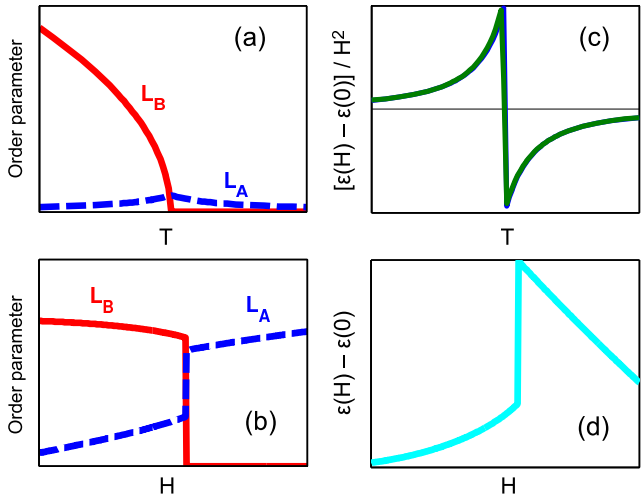

Figure 4.26: *The temperature dependence of order parameters L_A (dashed line) and L_B (solid line) near the second-order (a) and first-order (b) transitions. Panel (c) shows the anomaly in rescaled magnetocapacitance at the second-order transition temeprature; the two curves calculated for different values of magnetic field are almost indistinguishable. The magnetocapacitance anomaly at the first-order transition is shown in panel (d) [44].*

fields the transition is second-order (gray dashed line in Fig. 4.25), while in high fields and at low temperatures it becomes first-order (black line). The first- and second-order transition lines are separated by a critical point (CP). This change in the nature of the transition is also clearly seen in experiments by comparing the field-dependence of the MC at low and high temperatures (see, respectively, Fig. 4.23(a) and Fig. 4.24(a). The low-temperature MC is discontinuous at the first-order transition and its shape is well reproduced within the two-parameter Landau model [(see Fig. 4.26(d)]. The precise position of the CP on the magnetic phase diagram of $YbMnO_3$ is difficult to determine, because a clear-cut discontinuity in the MC is only observed at 2 K. Furthermore, changes in the character of the transition are influenced by the fact that at low temperatures and high magnetic fields the magnetic response is dominated by the Yb spins, which order ferrimagnetically below 3.8 K [26] [this behavior is not captured by the simple model in Eq.(4.3)]. This leads to a strong decrease of the critical magnetic field at low temperatures ($H_c \sim 3$T at 2 K) and gives rise to the sharp discontinuity in magnetization (see Fig. 4.23(b)), reflecting the spin-flip transition associated with the Yb(4b) sites [38].

In order to check for the possible role played by domain walls in the complex behavior that we observe, we repeated our MC measurements close to T_N (at two temperatures, 78.5 K and 80 K) at different frequencies: 1 kHz, 10 kHz, 100 kHz, 500 kHz, and 1 MHz. We observed that the measured MC does not depend on frequency, suggesting that the contribution of domain walls is negligible.

We note that we do not expect ferroelectric domains to be present in the *ab* plane (the direction along which we measured our magnetocapacitance) since the polar axis is *c*. Therefore, magnetic

domain walls are of prime importance in our case. Nevertheless, due to the multiferroic nature of the material, one may expect that coupling at the magnetic domain walls induces electrical domains.

For many ferroelectrics the contribution of ferroelectric domain walls only vanishes at frequencies above 10^9 Hz [46] . Therefore, in the range of frequencies where we measure MC (10^3-10^6 Hz), we cannot in theory rule out the presence of a contribution from the domain walls. In practice, however, the absence of a frequency dependence of the MC is a good indication that the contribution of domain walls to the MC is negligible.

In Fig. 4.27 we plot the MC measured for both E and H parallel to the *c*-axis. We observe qualitatively similar behavior to before; there are anomalies at low temperatures corresponding to the Yb spin-flip transition, and similar anomalous behavior is present close to T_N, which we have described in terms of competition between different magnetic phases, one of which allows a ferromagnetic component. One major difference is in the magnitude of the MC, which at low temperatures is comparable for both electric field directions, but close to T_N is an order of magnitude larger when E is parallel to *ab*. At present we are unable to explain this large anisotropy.

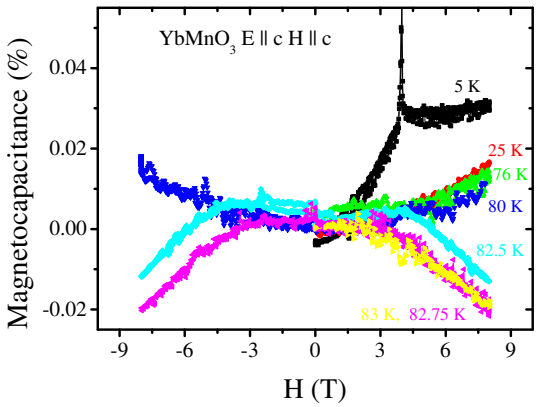

Figure 4.27: *Magnetocapacitance measurements of $YbMnO_3$ at different temperatures, $E \parallel c$, $H \parallel c$.*

4.5.4. High Field Magnetocapacitance Measurements on $YbMnO_3$ single crystal and Magnetic Phase Diagram

We present MC measurements on $YbMnO_3$ single crystals performed at different temperatures in fields of up to 30 T in Fig. 4.28. While the behavior up to H = 9 T is known from earlier measurements, we observe new anomalies close to 15 T for temperatures between 20K and 75 K. Another interesting observation at high fields is the behavior of magnetocapacitance at 78 K, where

we observe first an anomaly around 9 T, then a sharp decrease which saturates around 20 T and increases again. This saturation at high fields is also observed at 85 K.

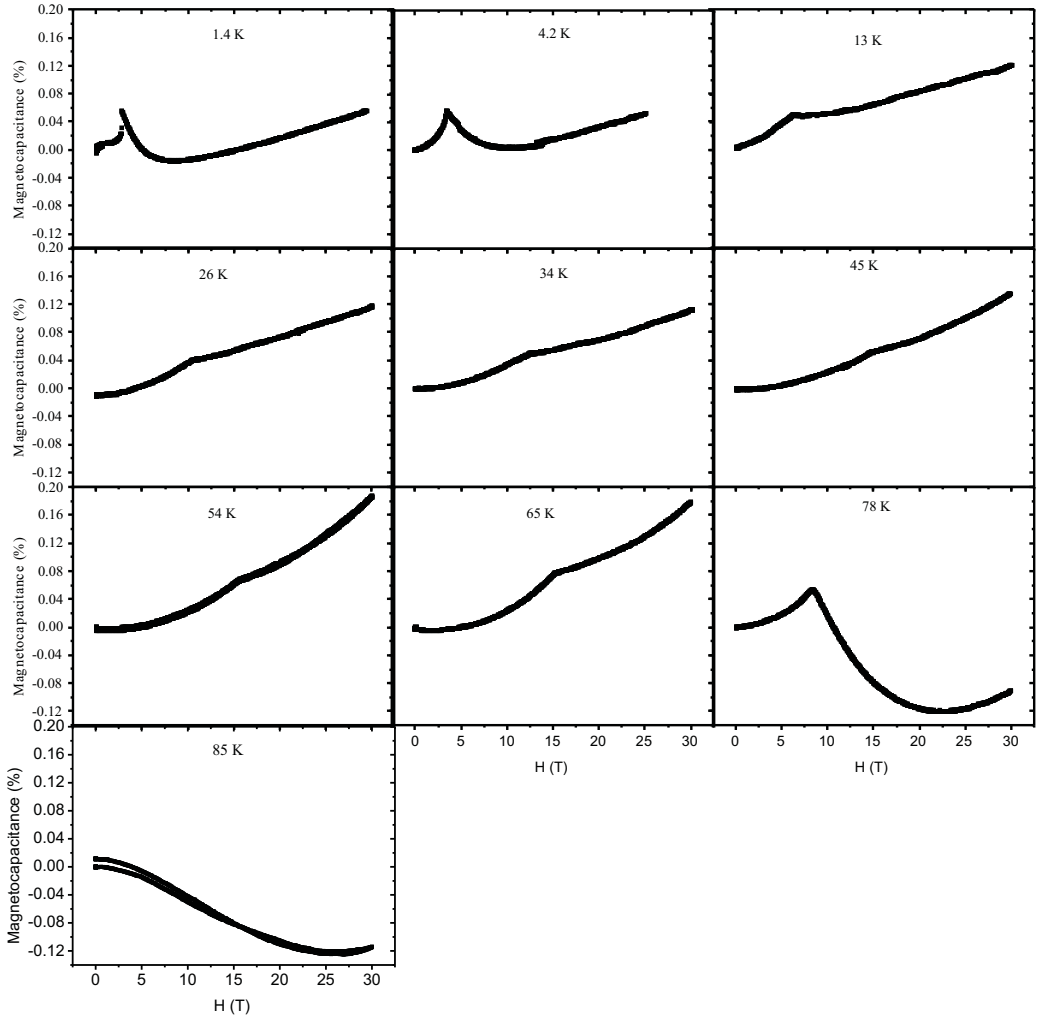

Figure 4.28: *Magnetocapacitance measurements of $YbMnO_3$ at high fields and different temperatures, $E \parallel ab$, $H \parallel c$.*

In Fig. 4.29 we present the magnetic phase diagram obtained from anomalies in our MC, magnetic susceptibility and magnetization versus field measurements (ε_T(H), χ_T(H), M(H)). We include datapoints corresponding to the high-field magnetization measurements of Tomuta [38], which agree well with our measurements. We note that the crystals studied by Tomuta were grown by the flux growth technique while ours was grown by the floating zone technique. Our theoretical interpretation of the MC anomaly close to T_N allows us to understand the phase diagram and to confirm the explanation offered by Tomuta. The A2 phase is stabilized by external magnetic fields along the c direction because this phase allows canting of the spins perpendicular to the triangular lattice in the

ab plane. The observed reentrant behavior of the A2 phase must be related to the ordering of spins on the Yb (4b) site at 30K. The ordered Yb spins are oriented parallel to *c* and the internal field that amplifies the effect of the external field below 30 K, which decreases the critical field necessary for a magnetic phase transition to occur from the B2 phase to the A2 phase. We note that our phase diagram differs from that determined by Fiebig *et al.* using optical techniques [35] (see Fig. 4.21). Although the magnetic phases are the same, the A2 phase is stabilized at much higher fields ($\sim$ 16 T) in our phase diagram than in the optically determined phase diagram: ($\sim$ 4 T). Also, there is a region of hysteresis in the phase diagram of Fiebig *et al.* while we observe no hysteresis in our magnetocapacitance measurements. Our magnetic phase diagram is in agreement with Yen *et al.*'s phase diagram up to the magnetic fields of 14 T, which is the largest field reached in their study [26]. Just before we submitted our manuscript [44] on the complex behavior of magnetocapacitance and magnetic phase diagram from magnetocapacitance measurements, we became aware of similar work carried out by Yen *et al.* [26]. Our magnetic phase diagram is in agreement with that reported by Yen *et al.* up to 14 T, the highest field reached in that study.

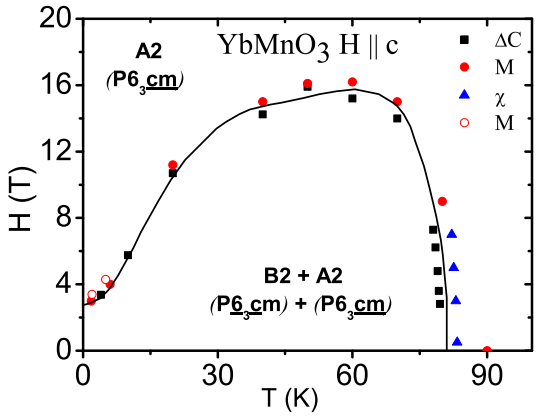

Figure 4.29: *Magnetic phase diagram of $YbMnO_3$ obtained from MC (filled squares) and magnetization (open circles) measurements at high fields; magnetization data from Ref. [38] are also included (filled circles). The solid line is a guide to the eye.*

4.6. Magnetodielectric coupling in $ErMnO_3$

It has been shown by Fiebig *et al.* that $YbMnO_3$ and $ErMnO_3$ have the same magnetic symmetries and similar magnetic phase diagrams. However, we have shown in the previous section that the phase diagram of $YbMnO_3$ is different to that determined by Fiebig *et al.* [35] using optical techniques. Furthermore, the difference in rare-earth cations might change the 3d-4f interactions

and hence the magnetodielectric coupling. Therefore, it was interesting to investigate the magnetodielectric coupling in $ErMnO_3$.

4.6.1. Magnetic Structure

The magnetic structure of $ErMnO_3$ has previously been determined by Tomuta using neutron diffraction [38]. The Mn spins order in AF fashion below 78 K. The spins on the Er(4b) site start to order in AF fashion below 15 K, whereas the spins on the Er(2b) site order at 2 K. Fiebig *et al.* have also studied the magnetic structure of $ErMnO_3$ [35], the symmetry of which is the same as that of $YbMnO_3$ and $TmMnO_3$, while the critical fields defining the phase boundaries are similar. The symmetry of the low-field phase is B2 and high fields applied along *c* stabilize the A2 phase, which allows spin canting along the direction of the applied field.

4.6.2. Magnetization Measurements on $ErMnO_3$

In Fig. 4.30 we present the magnetic susceptibility as a function of temperature for magnetic fields applied parallel and perpendicular to the *ab* plane. The anomaly in the χT curve for H $\parallel$ *c* indicates that T_N is 78 K. The Weiss temperatures parallel and perpendicular to the *ab* plane are -21 K and -122 K, respectively. The effective magnetic moments for these two magnetic field directions are 10.29 and 11.73 μ_B, comparable to the expected value of 10.68 μ_B. All of these magnetic parameters are in agreement with previously reported single crystal data [24, 26, 38]. It has been suggested that the magnetic anisotropy reflects the anistropic character of the magnetic interactions; the Mn spins lie in the *ab* plane whereas the rare-earth spins lie parallel to *c* [26, 47].

4.6.3. Capacitance and Magnetocapacitance Measurements on $ErMnO_3$

Similar to the other hexagonal manganites and in agreemeent with previous reports, we see an anomaly in the dielectric constant below T_N = 77 K for both ε_{ab} and ε_c (Fig. 4.31). As in the case of $YMnO_3$ and $YbMnO_3$, the decrease in ε_{ab} is more pronounced than that in ε_c. In addition to the anomaly at T_N, there is one more anomaly around 40 K, more pronounced for ε_{ab}. In the literature no magnetic transition has been reported around this temperature, and we suggest that this peak might be related to the presence of Mn_3O_4 as an impurity phase. The Mn spins in Mn_3O_4 order in ferromagnetic fashion at 41 K, coupling to and causing a decrease in the dielectric constant [48]. However, we do not observe any anomaly at 41 K in our magnetization measurements. Therefore, the possible Mn_3O_4 impurity might be due to local non-stoichoimetry in the crystal piece measured.

In Fig. 4.32 we show the MC and magnetization as a function of field. The magnetic field was applied parallel to *c* for both measurements. At 2 K, an abrupt increase in the magnetization

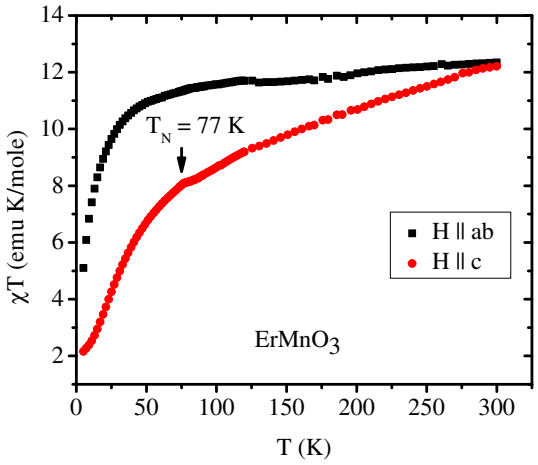

Figure 4.30: *Temperature dependence of magnetic susceptibility of $ErMnO_3$, circles denote measurements $\parallel$ c, squares $\perp$ c.*

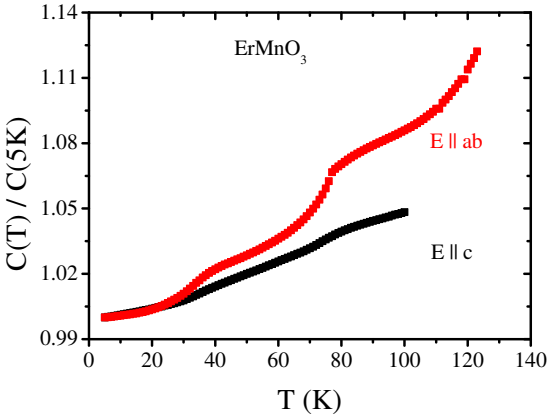

Figure 4.31: *Temperature dependence of capacitance of $ErMnO_3$, measured in two orientations.*

takes place at approximately 1 T, and at 5 K this abrupt increase shifts to higher critical fields. The capacitance at 2 K increases rapidly until 1 T, where an anomaly is apparent, coincident with the magnetic phase transition. The behavior of the capacitance is approximately quadratic at higher fields. As the temperature is increased, the capacitance increases less rapidly below the critical field, which is also shifted to higher values. This field-induced transition in the magnetization was discussed by Tomuta [38]. Similar to the case of $YbMnO_3$, at 2 K the field induced transition at $\sim$1 T is ascribed to a spin-flip transition of the Er spins occupying the 4(b) site.

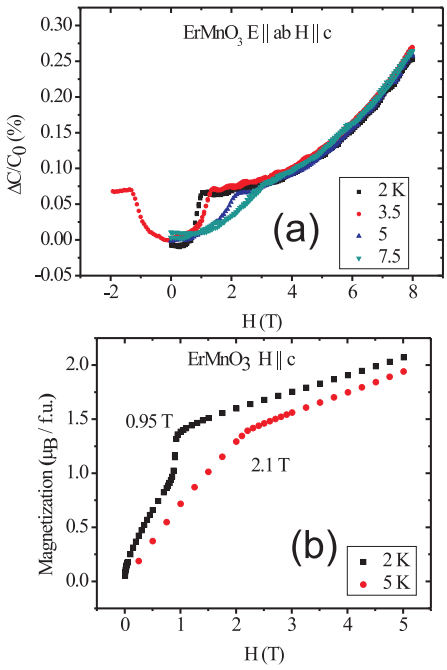

Figure 4.32: *Magnetic field dependence of (a) capacitance and (b) magnetization of $ErMnO_3$ at low temperatures; $H \parallel c$ in both cases and $E \parallel ab$ in (a).*

The behavior of the MC in $ErMnO_3$ close to T_N is also similar to that of $YbMnO_3$. We show MC curves at different temperatures in Fig. 4.33. The magnetic field was applied parallel to *c*, while the electric field was parallel to the *ab* plane. When T_N is approached from below, the MC is initially positive and approximately quadratic in shape; this can be seen for example at 75 K. At approximately 6 T there is a downturn in the MC, which decreases sharply on increasing the magnetic field further and becomes negative. As the temperature is increased this downturn occurs at lower fields, and at 77 K the negative component of the MC dominates at all fields. Upon increasing the temperature further, the MC remains negative

but its magnitude decreases. We suggest that the physics behind the behavior of the MC is the

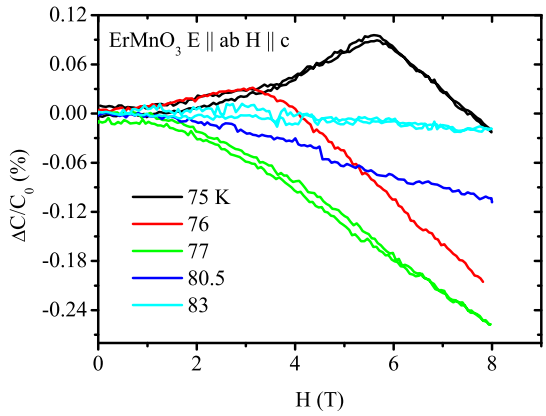

Figure 4.33: *MC measurements of $ErMnO_3$, at temperatures close to T_N; $E \parallel ab$, $H \parallel c$.*

same as that close to T_N in $YbMnO_3$, that is, it originates from competition between the B2 and A2 phases, where the latter allows a ferromagnetic moment along the applied field direction, *c*. However, the MC was measured at too few temperatures for constant-field cuts to be taken, as was carried out for $YbMnO_3$ in Fig. 4.24.

In order to investigate the anisotropy in the MC, we carried out measurements with both $E \parallel c$ and $H \parallel c$ (Fig. 4.34). We observed similar behavior at low temperatures to the case of $E \parallel ab$. However, close to T_N, the magnitude of the MC was 6 times smaller for $E \parallel c$, even though the shapes of the anomalies were similar.

4.6.4. High-Field Magnetization and Magnetocapacitance Measurements, Construction of Magnetic Phase Diagram

For $YbMnO_3$ we were able to use high-field MC measurements to map the magnetic phase diagram, which was in good agreement with the phase diagram constructed using magnetization data measured as a function of field. We have also attempted to use high-field magnetization measurements, shown in Fig. 4.35, to construct the magnetic phase diagram for $ErMnO_3$. At 6 K we observe an anomaly at approximately 2.5 T, consistent with our lab magnetization data. A second anomaly occurs at approximately 9 T in the form of a slight change in slope, and a third anomaly is clearly visible at approximately 15 T. From the derivative of the magnetization at 15 K, two anomalies at 5.5 T and 12 T are apparent. However, at higher temperatures, although the behavior is nonlinear, it is difficult to detect any transitions. Thus, magnetization measurements at high fields are insufficient to map the magnetic phase diagram.

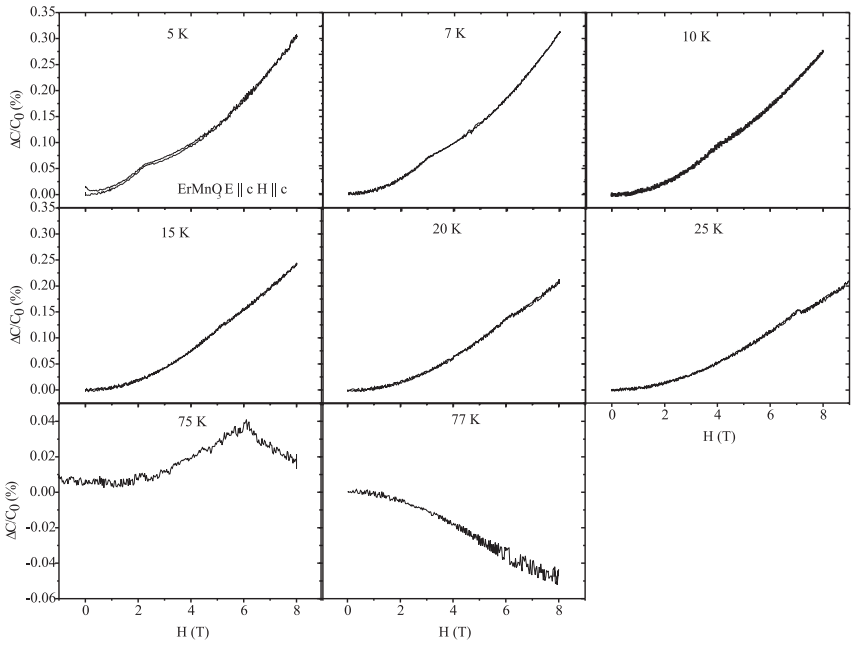

Figure 4.34: *MC measurements of $ErMnO_3$ at different temperatures; $E \parallel c$, $H \parallel c$.*

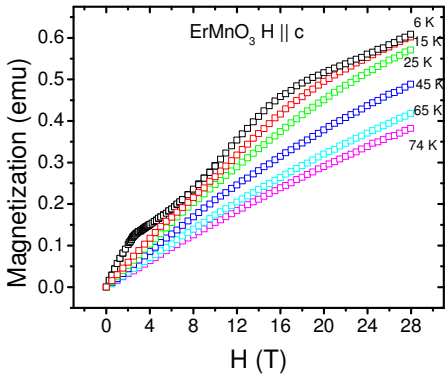

Figure 4.35: *Magnetization measurements of $ErMnO_3$ at high magnetic fields, $H \parallel c$.*

We have measured the MC for E $\parallel$ *ab* at high fields of up to 30 T (Fig. 4.36). The data collected at 1.4 K contain a sharp anomaly at 0.7 T, consistent with the field-induced transition observed in the magnetization measurements. The discontinuous character of this transition suggests that it is first-order in nature. With further increasing field, the MC starts to decrease and passes through a broad minimum at 4.4 T, then increases again. At approximately 15.5 T there is clear change in the slope. At 4.2 K, there is a sharp anomaly at approximately 1.8 T and a very broad anomaly at approximately 17 T. At 11.4 K these two anomalies are found at 3.9 T and 17 T. At all other temperatures below T_N, only one MC anomaly is apparent, occurring as a small change in the slope. We used these data to

construct the phase diagram shown in Fig. 4.37, which is in agreement with that recently reported by Yen *et al.* [26]. Although our high-field magnetization and MC measurements showed the presence of an additional phase transition at 15-17 T to that reported in Ref. [26], it could only be resolved for T $<$ 15 K, and thus a complete phase line cannot be drawn.

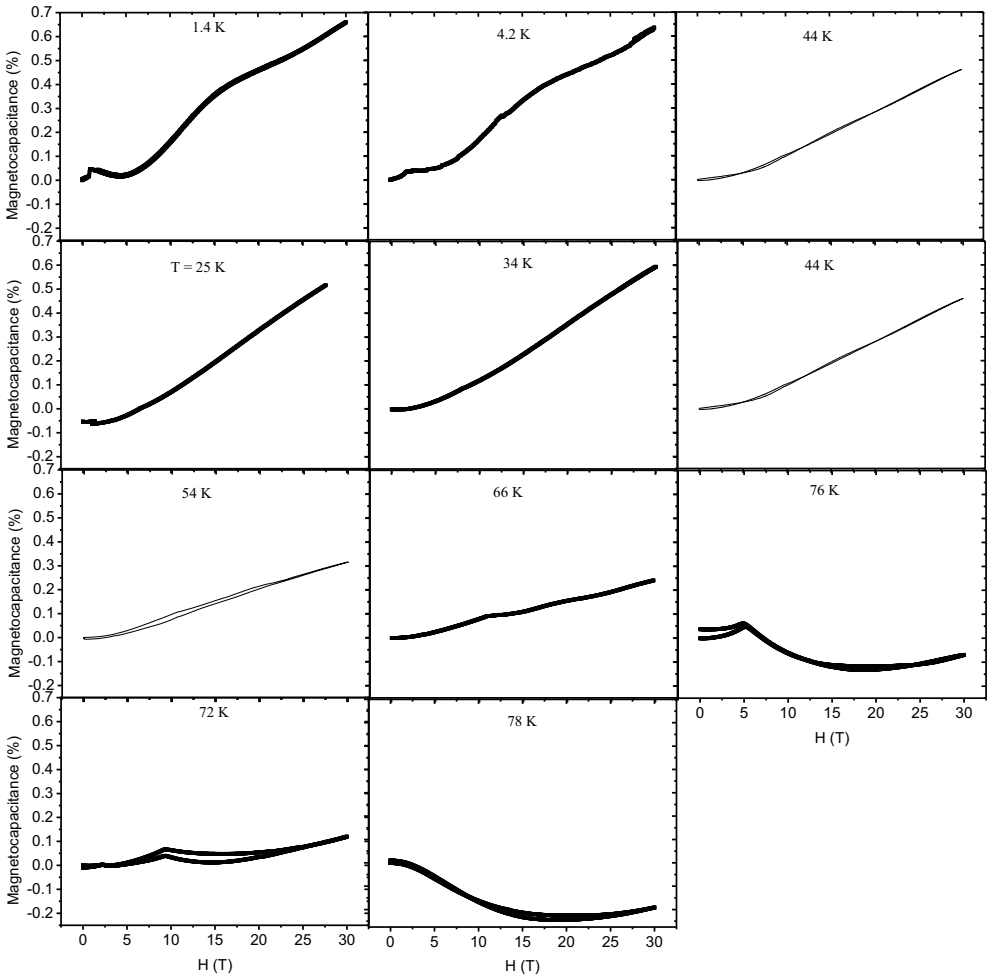

Figure 4.36: *Magnetocapacitance measurements of $ErMnO_3$ at high fields and different temperatures, $E \parallel ab$, $H \parallel c$.*

4.7. The case of Y(Mn,Ga)O_3 single crystals

Our magnetocapacitance measurements have shown that the magnetodielectric coupling in $YMnO_3$ is small. Due to the triangular Mn spin structure, the magnetic exchange interactions in $YMnO_3$ are frustrated. Frustrated systems are known to be very susceptible to small perturbations. Therefore,

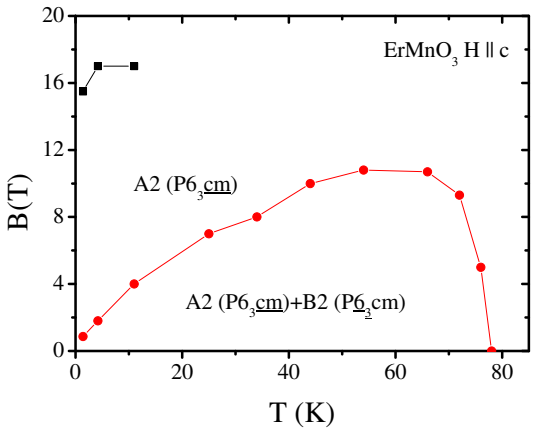

Figure 4.37: *Magnetic phase diagram of $ErMnO_3$ obtained from the MC measurements.*

it is of interest to study the effect of doping on the Mn site, which should affect the frustrated Mn spin ordering and hence the magnetodielectric coupling. We chose Ga^3 as the dopant cation. It is known that $YGaO_3$ is isostructural to $YMnO_3$ and thus is also ferroelectric [18]. We also know from our structural studies in section 4.3 that doping $YMnO_3$ with Ga increases the *c*-axis but does not significantly affect the dipole moments associated with the relative Y-O displacements.

4.7.1. Capacitance and Magnetocapacitance Measurements on $YMn_{1-x}Ga_xO_3$

Fig. 4.38 shows the magnetic susceptibility of $YMn_{1-x}Ga_xO_3$ measured as a function of temperature for H parallel and perpendicular to the *c*-axis. The anisotropy is small. For x = 0, 0.1 and 0.3, cusps are observed at 72 K, 65 K and 32 K, respectively, indicating the onset of AF ordering. No magnetic ordering is observed for x = 0.5. The corresponding effective moments per Mn^{3+} are $4.93\mu_B$ for $x = 0.0$, $4.82\mu_B$ for $x = 0.1$, $4.38\mu_B$ for $x = 0.3$, and $3.62\mu_B$ for $x = 0.5$. Thus, the ratio of the Weiss temperature to T_N, indicative of frustration in the magnetic structure, increases upon doping.

The capacitance measurements for the different crystal orientations shown in Fig. 4.39 also exhibit anomalies at T_N for all compositions except x = 0.5, similar to the magnetic susceptibility data. Similar to undoped $YMnO_3$, discussed in section 4.4, anomalies are only visible in ε_{ab} for the doped compounds. In the inset of Fig. 4.39(a), the order parameter L is shown; this is calculated from ΔC as explained in section 4.4.3.

For E $\parallel$ *ab* and H $\parallel$ *c* [Fig. 4.40(a)], the MC of undoped $YMnO_3$ is small, increasing slightly on doping. For E $\parallel$ *c* and H $\parallel$ *ab* [Fig. 4.40(b)], the MC of the undoped compound is smaller than the

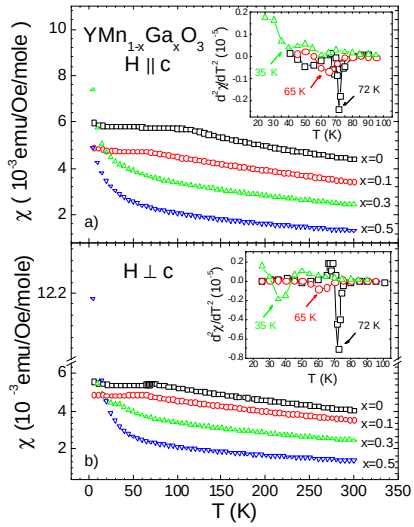

Figure 4.38: *Temperature dependence of magnetization measured in magnetic field of 1000 Oe on $YMn_{1-x}Ga_xO_3$ single crystals for (a) $H \perp c$ and (b) $H \parallel c$. The insets show the Néel temperatures obtained from the minimum of $d^2\chi/dT^2$.*

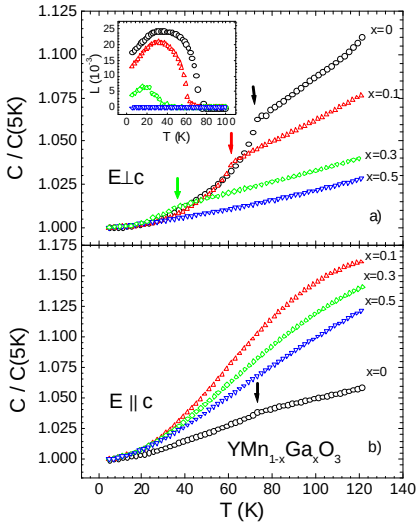

Figure 4.39: *Temperature dependence of the capacitance of $YMn_{1-x}Ga_xO_3$ single crystals normalized to the capacitance at 5 K for (a) $E \perp c$ and for (b) $E \parallel c$.*

sensitivity of our measurements. However, for x = 0.1 a positive MC is clearly observed. For x = 0.3, the MC becomes negative and even larger in magnitude. In both cases the behavior of the MC is quadratic until high fields, where it deviates.

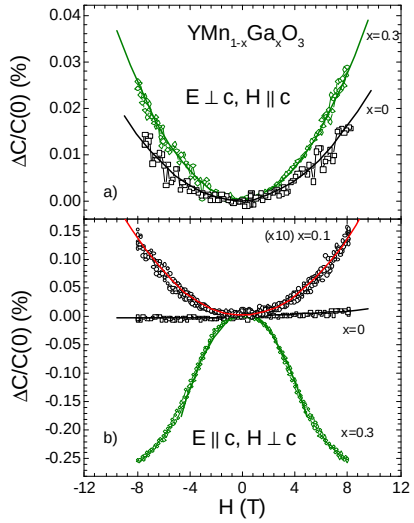

Figure 4.40: *Magnetocapacitance of $YMn_{1-x}Ga_xO_3$ at 5 K for (a) $E \perp c$ and $H \parallel c$, (b) $E \parallel c$ and $H \perp c$.*

We show in Fig. 4.41 that at 5 K, the MC response of the x = 0.3 sample is similar for both H $\parallel$ *ab* and H $\parallel$ *c* when E $\parallel$ *c*. Fig. 4.41(b) shows that the magnetization becomes non-linear at high fields.

Interestingly, the MC of $YMn_{1-x}Ga_xO_3$ shows a strong dependence on Ga-doping. On doping with 30 %, we observe an approximately two-fold increase in the transverse magnetodielectric coupling, which we have quantified using the Landau expressions discussed previously for the undoped compound in section 4.3 of this chapter. The MC originates from a term γP^2H^2, and increases from $\gamma_\perp = -31 \times 10^{-4}$ T^{-2} for $x = 0$ to $\gamma_\perp = -55 \times 10^{-4}$ T^{-2} for $x = 0.3$ [see Fig. 4.40(a)]. However, a much more pronounced increase of approximately two orders of magnitude is shown in Fig. 4.40(b) for the coupling along the *c* axis: an increase from $\gamma_\parallel = -11 \times 10^{-4}$ T^{-2} for $x = 0$ to $\gamma_\parallel = 14 \times 10^{-2}$ T^{-2} for $x = 0.3$ is accompanied by a sign reversal of the magnetodielectric coupling constant $\gamma_\parallel$. While in the undoped sample $\gamma_\parallel$ is comparable to $\gamma_\perp$ and the anisotropy of the MC largely reflects the anisotropy of the dielectric constant [see Eq.(4.2)], the coupling constant $\gamma_\parallel$ for $x = 0.3$ is two orders of magnitude larger than $\gamma_\perp$. Thus, the relative change of capacitance in magnetic field increases for $E \parallel c$ in the doped samples.

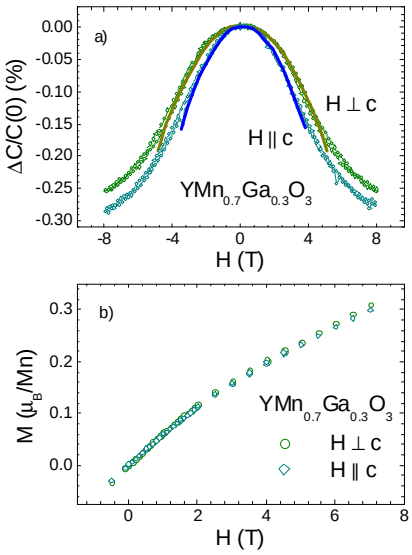

Figure 4.41: *(a) Magnetocapacitance of $YMn_{0.7}Ga_{0.3}O_3$ at 5 K with $E \parallel c$ measured for both $H \parallel c$ and $H \perp c$. (b) Field dependence of magnetization of $YMn_{0.7}Ga_{0.3}O_3$ at 5 K for both $H \parallel c$ and $H \perp c$.*

4.7.2. Local canting in a dilute triangular XY antiferromagnet

The coupling of electric polarization to magnetic field can be mediated via a phonon or strain [49]. If, for example, P and H are coupled to a lattice distortion of amplitude u by $\Phi_{int} = -u\left(\alpha P^2 + \beta H^2\right)$, then minimization of the sum of Φ_{int} and the lattice energy $\frac{K}{2}u^2$ with respect to u gives (among other terms) an effective coupling $\frac{1}{2}\gamma P^2 H^2$ with $\gamma = -\frac{2\alpha\beta}{K}$. The increase of γ upon doping then reflects the increase of the coupling constants α and/or β. While our measurements do not allow us to make definite conclusions, the observed enhancement of the MC is most likely related to an increase in lattice distortion in an applied magnetic field, because the 120° spin state is suppressed by doping.

The magnetoelastic coupling in hexagonal $RMnO_3$ is known to be rather strong [6,50]. However, the interlayer spin exchange in the 120° state, sensitive to shifts of ions in the c -direction, is strongly frustrated, because each spin is coupled to three neighbors in the form of a triangle in the adjacent layers, which results in a total spin of zero. The similar temperature dependence of the dielectric and magnetic susceptibilities of the pure and doped samples shows that, at least up to $x = 0.3$, the spin dilution does not fully suppress the magnetic ordering and does not give rise to a spin-glass state, as observed in some other frustrated materials. Rather, the initial quasi-2D AF order becomes locally suppressed by Ga-doping. The dilution of the spin lattice by non-magnetic Ga ions induces magnetic moments in the triangular layers, as reported previously [51]. This increases the magnetic susceptibility of the Mn layers and destroys the spin cancellation in the triangles. Therefore, the local suppression of the 120° spin ordering relieves the frustration and increases the energy of the interlayer interactions, which can in turn lead to an enhancement of the magnetodielectric coupling

in the *c* direction. The proposed scenario is similar to the mechanism responsible for AF ordering induced by doping in the quasi-one-dimensional spin-Peierls material $CuGeO_3$ [52], where the substitution of magnetic Cu by non-magnetic Zn or Mg breaks spin singlets in the Cu chains and gives rise to a three-dimensional spin ordering [53, 54].

A similar enhancement of MC was found in Ti-doped $YMnO_3$ [55]. That material, however, shows a structural transition induced by Ti-doping, whereas $YMn_{1-x}Ga_xO_3$ remains hexagonal and ferroelectric for all doping concentrations considered, showing that the observed increase of MC in $YMn_{1-x}Ga_xO_3$ is largely due to the effect of Ga-substitution on the magnetic ordering.

In conclusion, Ga-substitution in $YMnO_3$ suppresses the AF ordering and leads to a strong enhancement of the MC, which we ascribe to increased magnetic coupling between layers.

4.8. General Conclusions

Our structural studies of hexagonal $RMnO_3$ (R = Y, $Yb_{0.5}Y_{0.5}$, Yb, Lu) show that the ferroelectric distortion, as evidenced by the local dipole moments associated with the R cations and by tilting and buckling of the MnO_5 trigonal bipyramid, increases with decreasing ionic radius of R. We have also studied the effect of changing the orbital occupation and ionic radius on the bipyramidal site by partially replacing Mn with Ga. We can identify two main conclusions from our structural investigations of $YMn_{1-x}Ga_xO_3$. 1) On Ga-substitution there is no significant change in the local coordination of the magnetic Mn ions; the tilting and buckling of the MnO_5 trigonal bipyramid remains essentially unchanged. 2) The local dipoles associated with the Y ions decrease with doping, but the net polarization does not markedly decrease.

We have studied the nature of the magnetodielectric coupling in hexagonal $RMnO_3$ in detail. Our measurements show that the capacitance of single crystal $YMnO_3$ is dependent of applied magnetic field, in contrast to the previous reports on polycrystalline samples [6]. We can use Landau theory to explain that the dielectric anomaly just below T_N originates from a coupling term P^2L^2 in the free energy. We observed anisotropy in the dielectric constant below T_N for all of the $RMnO_3$ samples investigated; the dielectric constant decreases more rapidly below T_N when the electric field is applied parallel to the plane of magnetic ordering (ab plane) than when it is applied parallel to the polar *c*-axis. The low-field magnetocapacitance of $YMnO_3$ follows quadratic behavior, which originates from a coupling term P^2H^2 in the free energy. Magnetocapacitance anomalies at magnetic fields of ~ 16 T show the presence of a magnetic phase transition (in agreement with an earlier report [56]) when the field is applied perpendicular to the magnetic ordering (ab) plane. This probably involves a transition from the B1 ($P\underline{6}_3c\underline{m}$) to the A2 ($P6_3\underline{cm}$) phase.

Magnetocapacitance measurements on $YbMnO_3$ revealed complex behavior close to T_N. We

have shown after appropriate rescaling, the data obtained at different fields and temperatures lie on a single critical curve that describes a sharp anomaly in the nonlinear dielectric response. We have explained the shape of the experimental curves using the phenomenological Landau theory and have shown that the anomalous behavior originates from competition between two antiferromagnetic phases, one of which allows a spontaneous uniform magnetization. Our high-field magnetocapacitance measurements have allowed us to construct a magnetic phase diagram in terms of these two phases.

The magnetic phases of $YbMnO_3$ and $ErMnO_3$ have previously been reported to be the same and we have confirmed using magnetocapacitance measurements that this is the case. $ErMnO_3$ appears to show the same complex behavior close to T_N as $YbMnO_3$. However, in contrast to $YbMnO_3$, high-field magnetization measurements were unable to map the magnetic phase diagram, which remains incomplete. Although an additional transition to an unknown phase appears to occur at $\sim$ 16 T, we were only able to detect the transition for temperatures below 15 K, and only a partial phase line could be drawn.

The substitution of Ga on the Mn site of $YMnO_3$ has a dramatic effect on the magnetodielectric coupling. Although T_N decreases as the proportion of Ga increases, the magnetocapacitance in$YMn_{0.7}Ga_{0.7}O_3$ is 70 times higher than that of undoped $YMnO_3$. This is probably due to an increased magnetic coupling between the layers of Mn sublattice by the substitution of non-magnetic Ga.

Bibliography

[1] E.F. Bertaut, F. Forrat, and P. Fang, C.R. Acad. Sci. Paris, 256. 1958, (1963).

[2] G. A. Smolenskii and B. A. Bokov, J. Appl. Phys. 35, 915, (1964).

[3] Z. J. Huang, Y. Cao, Y. Y. Sun, Y. Y. Xue, and C. W. Chu, Phys. Rev. B, 56, 2623 (1997).

[4] M. Fiebig, T. Lottermoser, D. Frohlich, A. V. Goitsev, and R. Pisarev, Nature 499, 6909, (2002).

[5] A.B. Souchkov, J. R. Simpson, M. Quijada, H. Ishibashi, N. Hur, J.S. Ahn, S. -W. Cheong, A. J. Millis, and H. D. Drew, Phys. Rev. Lett. 91, 027203, (2003).

[6] B. Lorenz, A. P. Litvinchuk, M. M. Gospodinov, and C. W. Chu, Phys. Rev. Lett. 92, 087204 (2004).

[7] F. Yen, C.R. dela Cruz, B. Lorenz, Y.Y. Sun, Y. Q. Wang, M.M. Gospodinov, and C.W. Chu, Phys. Rev. B, 71, 180407, (2005).

[8] P. A. Sharma *et al.*, Phys. Rev. Lett., 93, 177202, (2004).

[9] T. Katsufuji *et al.*, Phys. Rev.B, 66, 134434, (2002).

[10] T. Lonkai, D. G. Tomuta, U. Amann, J. Ihringer, R. W. Hendrikx, D. M. Tobbens, and J. A. Mydosh, Phys. Rev.B, 69, 134108, (2004).

[11] G. Nénert, M. Pollet, S. Marinel, G. R. Blake, A. Meetsma, and T. T. M. Palstra, J. Phys. Condens. Matter,19, 466212, (2007).

[12] B. B. van Aken, T. T. M. Palstra, A. Filippetti, and N. A. Spaldin, Nature Materials, 3, 164, (2004).

[13] C. J. Fennie, and K. M. Rabe, Phys. Rev.B, 72, 100103(R), (2005).

[14] Seongsu Lee, A. Pirogov, Jung Hoon Han, J.-G. Park, A. Hoshikawa, and T. Kamiyama, Phys. Rev. B, 71, 180413(R).

[15] S. Lee, *et al.*, Nature, 451, 805-U4, (2008).

[16] N. A. Hill , Journal of Phys. Chem. B, 104 (29), 6694-6709, (2000).

[17] B. B. Van Aken, and T. T. M. Palstra, Phys. Rev.B, 69, 134113, (2004).

[18] S. C. Abrahams, Acta Cryst B57, 485-490, (2001).

[19] S. Geller, J. B. Jeffries, and P.J. Curlander, Acta Cryst B31, 2770, (1975).

[20] H. D. Zhou, J. C. Denyszyn, and J. B. Goodenough, Phys. Rev.B, 72, 224401, (2005).

[21] B. B. van Aken, A. Meetsma, and T. T. M. Palstra, Acta Cryst. C57, 230-232, (2001).

[22] T. Katsufuji, S. Mori, M. Masaki, Y. Moritomo, N. Yamamoto, and, H. Takagi, Phys. Rev. B, 64, 104419, (2001).

[23] B. B. Van Aken, J. W. G Bos, R. A. de Groot, and T.T.M. Palstra, Phys. Rev. B. 63, 125127, (2001).

[24] H. Sugie, N. Iwata, and K. Kohn, J. Phys. Soc. Jpn., 71, 1558 (2002).

[25] A. P. Ramirez, Annu. Rev. Mater. Sci. 24, 453, (1994).

[26] F. Yen, C. dela Cruz, B. Lorenz, E. Galstyan, Y. Y. Sun, M. Gospodinov, and C.W., Chu, J. Mater. Res. **22(8)**, 2163, (2007).

[27] M. Fiebig, Th. Lottermoser, Th. Lonkai, A. V. Goltsev, and R. V. Pisarev, Journal of Magnetism and Magnetic Materials, 290, 883-890, (2005).

[28] G. Lawes, A. P. Ramirez, C. M. Varma, and M. A. Subramanian, Phys. Rev. Lett., 91, 257208, (2003).

[29] L. D. Landau, E. M. Lifshitz, and L. P. Pitaevskii, Electrodynamics of Continuous Media (Pergamon, NewYork, (1984).

[30] A. A. Nugroho, N. Bellido, U. Adem, G. Nenert, Ch. Simon, M. O. Tija, M. Mostovoy, and T. T. M. Palstra, Phys. Rev. B. 75, 174435, (2007).

[31] M. S. Seehra and R. E. Helmick, J. Appl Phys. 55, 2330, (1984).

[32] T. Katsufuji and H. Takagi, Phys. Rev.B, 64, 054415, (2001).

[33] D. L. Fox, D. R. Tilley, J. F. Scott, and H. J. Guggenheim, Phys. Rev. B 21, 2926 (1980).

[34] M. S. Seehra and R. E. Helmick, Phys. Rev.B, 24, 5068, (1981).

[35] A2 and B2 refer to the crystallographic magnetic point groups describing the spin symmetry, M. Fiebig et al., J. Appl. Phys., 93, 8194 (2003).

[36] H. D. Zhou, J. Lu, R. Vasic, B. W. Vogt, J. A. Janik, J. S. Brooks, and C. R. Wiebe, Phys. Rev. B 75, 132406 (2007.

[37] A. Munoz, J. A. Alonso, M. J. Martinez-Lope, M. T. Casais, J. L. Martinez, M. T. Fernandez-Diaz, Phys. Rev B, 62, 9498 (2000).

[38] D. Tomuta, PhD Thesis, Leiden University, (2003).

[39] T. Lonkai, D. Hohlwein, J. Ihringer, and W. Prandl, Appl. Phys. A, 74, S843 (2002).

[40] A. Muñoz, J. A. Alonso, M. J. Martinez-Lope, M. T. Casais, J. L. Martinez, and M. T. Fernandez-Diaz,, Phys. Rev. B, 62, 9498 (2000); Chem. Mater. 13, 1497 (2001); J. Phys. Condens. Matter, 14, 3285, (2002).

[41] M. Fiebig, C. Frohlich, K. Kohn, S. Leute, T. Lottermoser, V. V. Pavlov, and R. V. Pisarev, Phys. Rev. Lett., 84, 5620, (2000).

[42] M. Fiebig, C. Degenhardt, and R. V. Pisarev, J. Appl. Phys., 91, 8867 (2002).

[43] I. Munawar and S. H. Curnoe, J. Phys.: Condens. Matter, 18, 9575 (2006).

[44] U. Adem, M. Mostovoy, N. Bellido, A. A. Nugroho, Ch. Simon and T. T. M. Palstra, submitted to PRL (2008).

[45] Another contribution to the magnetocapacitance comes from an additional increase of L_{B} below T_N due to the suppression of L_{A}, which leads to the discontinuity and sign change of magnetocapacitance at T_N. This contribution is also proportional to H^2.

[46] D. A. Hall, Journal of Materials Science, 36, pp. 4575, (2001).

[47] T. J. Sato, S.-H. Lee, T. Katsufuji, M. Masaki, S. Park, J. R. D. Copley, and H. Takagi, Phys. Rev. B 68, 014432 (2003).

[48] R. Tackett, G. Lawes, B. C. Melot, M. Grossman, E. S. Toberer, and R. Seshadri, Phys. Rev.B, 76, 024409, (2007).

[49] C.-G. Zhong and Q. Jiang, J. Phys.: Condens. Matter, 14, 8605 (2002).

[50] C. delaCruz *et al.*, Phys. Rev. B, 71, 060407(R) (2005).

[51] A. Harrison, J. Phys. C: Solid State Phys. 20, 6287 (1987).

[52] M. Hase, I. Terasaki, and K. Uchinokura, Phys. Rev. Lett. 70, 3651 (1993).

[53] D. Khomskii, W. Geertsma, and M. Mostovoy, Czech. J. Phys. 46, Suppl. S6, 3229 (1996).

[54] M. Mostovoy and D. Khomskii, Z. Phys. B, 103, 209 (1997).

[55] Y. Aikawa, T. Katsufuji, T. Arima, and K. Kato, Phys. Rev. B, 71, 184418 (2005).

[56] N. Bellido, PhD Thesis, University of Caen, (2007).

CHAPTER 5

Origin of large and extrinsic dielectric constants in samples of this thesis

5.1. Introduction

Many new multiferroic and magnetoelectric materials have been discovered over the past few years and are actively being investigated. However, unusual and sometimes unreasonable dielectric and ferroelectric properties are reported due to a lack of knowledge of both the new samples being measured and aspects of the measurement techniques used. A few papers that address these important issues have been published [1–3], which state in summary that: (1) leaky samples may lead to cigar-shaped hysteresis loops in pyroelectric current measurements, which might be mistaken for real ferroelectric behavior; (2) extrinsic contributions to the dielectric constant might mask the intrinsic behavior of the sample and give rise to false reports of large, frequency-dependent dielectric constants and even magnetocapacitance.

All dielectric materials exhibit a frequency-dependent dielectric response. This is due to the frequency dependence of the different types of polarizabilities that they may possess. For inorganic materials, both the ionic and electronic polarizabilities contribute to the dielectric constant. All dielectric materials have electronic polarizability, which originates from shifting of the electron clouds relative to the nucleus in an electric field. Because the mass of electrons is low, they can respond to the electric signal up to optical frequencies. The time required for polarization to be established is directly related to the distance over which charge is being displaced. Although ions are much

heavier than electrons, they can also respond to frequency up to the infrared range. Polar molecules such as water orient in electric fields, giving rise to orientational polarization, a type not commonly found for inorganics. There is one more polarization mechanism that contributes to the dielectric constant: interfacial polarization (space-charge polarization). Space charges, continua of charge distributed over regions of space, are "heavy" since they result from macroscopic transfer of charge and therefore their response is already frozen at modest frequencies of the order of 1kHz [4].

Peter Debye considered that the response of an electrical dipole to an external electrical field is delayed because the dipole is embedded in the viscous medium of the molecule and therefore energy and time are consumed in order to orient the dipole. The orientation process is thus characterized by the dipole relaxation time, τ. The Debye equation considers a single relaxation time for all relaxing entities.

The Debye equation is written as

$$\varepsilon(\omega) = \varepsilon_\infty + \frac{\varepsilon_s - \varepsilon_\infty}{1 + i\omega\tau} \tag{5.1}$$

where ω is the frequency of the applied electric field, ε_∞ is the permittivity at optical frequencies, and ε_s is the static permittivity.

One can separate the real and imaginary parts of this equation to obtain,

$$\varepsilon'(\omega) = \varepsilon_\infty + \frac{\varepsilon_s - \varepsilon_\infty}{1 + (\omega\tau)^2} \tag{5.2}$$

and

$$\varepsilon''(\omega) = \frac{(\varepsilon_s - \varepsilon_\infty)\omega\tau}{1 + (\omega\tau)^2} \tag{5.3}$$

However, most dielectric materials depart from ideal Debye behavior [5]. Cole and Cole found that plots of ε'' vs ε' obtained from the Debye equation take the form of a semicircle and proposed that the data can be described by a modified Debye equation:

$$\varepsilon(\omega) = \varepsilon_\infty + \frac{\varepsilon_s - \varepsilon_\infty}{1 + (i\omega\tau)^{1-\alpha}} \tag{5.4}$$

Here, α characterizes the width of the distribution of relaxation times and ranges from 0 to 1.

The complex permittivity plots corresponding to the modified Debye equation are known as Cole-Cole plots and are used to detect relaxation phenomena. If more than one relaxation process occurs at the same time, they can be used to differentiate between the different processes. A schematic Cole-Cole plot is shown in Fig. 5.1. Here, ε_∞ is the dielectric permittivity at optical frequencies and ε_s is the static permittivity, that is, the permittivity at the lowest frequencies.

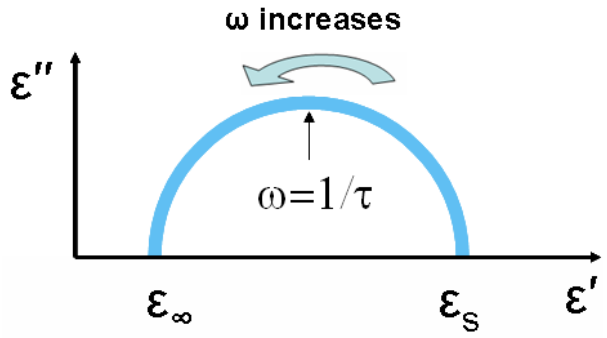

.

Figure 5.1: *Schematic picture of Cole-Cole plot*

In this chapter we focus on a special case of conventional Debye dielectric relaxation known as Maxwell-Wagner type relaxation. This occurs in electrically inhomogeneous materials, which have regions of different resistance and capacitance. At the interface of two electrically different regions, space charge (interfacial) polarization builds up in order to equilibrate the Fermi levels. Electrical inhomogeneity can be due to: (1) the formation of Schottky barriers at the electrode-sample interface; (2) more conducting/less conducting grain boundary interfaces in polycrystalline samples; (3) the presence of a depletion layer at oxygen deficient or rich surfaces; (4) a superlattice comprised of two different materials. Because Maxwell-Wagner relaxation involves the relaxation of space-charge dipoles, it takes place at low frequencies of the order of kHz. Therefore, if one measures at a frequency higher than the relaxation frequency of the sample, the contribution to the dielectric constant from the depletion layer must vanish.

The most prominent recent example to illustrate the importance of differentiating between extrinsic and intrinsic dielectric effects is $CdCr_2S_4$. This ferromagnetic compound was initially reported to be a multiferroic relaxor [6], but it was subsequently claimed that the measurements performed in this study were complicated by ordinary dielectric relaxation-type behavior [7]. The importance of this compound originates from a colossal magnetocapacitance of 3000 percent measured at 10 T; we note that a value of 10000 percent has been reported for the isostructural $HgCr_2S_4$, which is the largest magnetocapacitance ever reported in the literature [8]. However, the behavior of the capacitance in both $CdCr_2S_4$ and $HgCr_2S_4$ is extraordinary. The dielectric constant shows a sharp, step-like increase close to the ferromagnetic ordering temperature of 80 K, but the step is shifted to lower temperatures as the frequency is increased. The step in the capacitance can be considered as an indication of a relaxation process. The shift of the step to lower temperatures with increasing frequency is an unusual example of acceleration of relaxation dynamics with decreasing temperature [8]. Furthermore, the ferroelectric hysteresis loop is not saturated in fields of up to 0.4 MV/m.

Relaxor ferroelectrics constitute another class of materials that show a frequency-dependent response (dielectric constant and loss). However, they should not be confused with materials that exhibit dielectric relaxation. Relaxor ferroelectrics contain nanopolar regions; they generally have compositional disorder and are either doped ferroelectric or quantum paraelectrics (incipient ferroelectrics). The dielectric constant of these materials typically shows a broad peak. For a review of relaxor ferroelectrics, see [9].

Another recently studied material that has provoked discussion about different contributions to the dielectric constant is $CaCu_3Ti_4O_{12}$. This perovskite-like compound has a dielectric constant of the order of 10^4 at room temperature, staying almost constant over a wide temperature range, and decreasing to approximately 50 below 100 K when measured in an electric field of 100 Hz. When the frequency is increased, the temperature at which the dielectric constant decreases suddenly becomes higher than 200 K at 1 MHz. The topic of discussion regarding this material is the origin of the high room-temperature dielectric constant and the nature of the relaxation behavior [10, 11]. Lunkenheimer *et al.* have argued that the giant dielectric constant is due to the formation of a Schottky barrier and thus the presence of a depletion layer at the sample-electrode interface [12]. They have shown that although the capacitance is always large, it varies as the electrode material is changed due to the changing characteristics of the depletion layer. However, no voltage-dependent capacitance measurements have been reported; these can serve as evidence in favor of Schottky barrier formation. The lack of reported giant dielectric constants for other, isostructural members of this titanate family is also a concern. It should also be noted that the initial measurements on $CaCu_3Ti_4O_{12}$ were not carried out on single crystals. Sinclair *et al.* [13] have proposed that an internal boundary layer forms in the polycrystalline samples due to the presence of grain boundaries. They have used impedance spectroscopy to distinguish between two different regions of conductivity in the sample, corresponding to grains and grain boundaries. In similar fashion to the formation of Schottky barriers, regions of space charge are formed at the grain boundaries, which freeze out at low temperatures or high frequencies. However, depletion layers can form inside the grains as well as at the grain boundaries. In fact, a similar giant dielectric constant was later observed for single crystals [11], which questions the validity of the arguments concerning the formation of boundary layers in polycrystalline samples. Li *et al.* [14] have suggested that twin boundaries can also result in the formation of internal boundary layers. They have demonstrated the presence of two distinct types of conductivity in single crystals, corresponding to bulk and boundary regions. The number of different papers and views on this matter demonstrates the importance and complex nature of the problem.

The samples investigated in the previous chapters of this thesis are the hexagonal manganites ($YMnO_3$, $YbMnO_3$, and $ErMnO_3$) and the orthorhombic cuprates ($Y_2Cu_2O_5$, $Yb_2Cu_2O_5$, and

$Er_2Cu_2O_5$). We have focused on low temperature (magneto)capacitance measurements and on explaining the magnetoelectric coupling in these samples. Because the magnetic ordering temperatures in the hexagonal manganites (except for $ScMnO_3$) are below 100 K and in $R_2Cu_2O_5$ are below 30 K, our measurements have been concentrated on low temperatures. However, we observe that although the capacitance behavior at low temperatures is almost independent of the measurement frequency, this is not the case at room temperature. In addition, the dielectric constants of the hexagonal manganites measured at room temperature are very large.

5.2. Origin of the large dielectric constants in $YMnO_3$

5.2.1. Introduction

While measuring one of the most extensively studied multiferroics, $YMnO_3$, we observed an anomalously high dielectric constant ($\sim$ 1000) and dielectric loss at room temperature. The dielectric constants previously reported for $YMnO_3$ are of the order of 20 [15]. Being puzzled by this difference, we studied the dielectric properties of $YMnO_3$ single crystals to clarify the origin of this anomaly. An additional motivation for our study was the ongoing debate about the origin of the giant dielectric constant in $CaCu_3Ti_4O_{12}$, discussed above.

$YMnO_3$ belongs to the multiferroic $RMnO_3$ family, which exists for R = Y, Ho, Er, Tm, Yb, Lu, and Sc. The ferroelectric transition temperature of these materials lies around 1000 K, whereas magnetic order sets in below 70 K. The dielectric constant of $YMnO_3$ was measured to be approximately 20 by Smolenskii and Bokov at room temperature [15]. The same value was reported by Huang *et al.* at low temperatures [16]. However, in the vicinity of room temperature Huang *et al.* observed a rapid increase in the dielectric constant, which reached a value of 400 at 400 K. This increase in dielectric constant was strongly frequency dependent, becoming less significant at higher measurement frequencies. It was attributed to the approaching ferroelectric transition on heating [16]. However, the ferroelectric transition in $YMnO_3$ takes place at approximately 1100 K [17], far above room temperature. Furthermore, the signature of a ferroelectric transition is generally a sharp peak in the dielectric constant in close proximity to the transition temperature. Thus, it is unlikely that the observed increase in dielectric constant is due to the ferroelectric transition.

5.2.2. Results and Discussion

The temperature dependence of the capacitance and imaginary permittivity for a $YMnO_3$ single crystal with Ag electrodes is plotted in Fig. 5.2. At room temperature the capacitance is very high, whereas it relaxes to low values with decreasing temperature in the form of a step. A peak in the

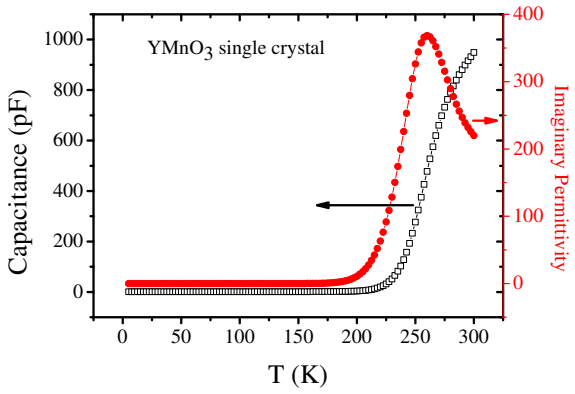

Figure 5.2: *Temperature dependence of capacitance of $YMnO_3$ single crystal, measured at 1kHz.*

dielectric loss accompanies the step in capacitance. Measurements as a function of frequency at fixed temperatures show a step-like decrease in the dielectric constant with increasing frequency, accompanied by a peak in the dielectric loss [Figs. 5.3(a) and 5.3(b)]. The frequency at which the step and peak are found is shifted to higher values with increasing temperature. The ac conductivity was calculated using the relation $\sigma_{ac} = \omega \times \varepsilon_0 \times \varepsilon$", and is shown in Fig. 5.3(c).

At 201 K and low frequencies, the ac conductivity increases linearly with a slope of 1.43. At approximately 10^4 Hz, the slope decreases to 0.12. As the temperature increases, the steeper slope is extended to higher frequencies. At 331 K and 373 K, another linear regime with a small slope emerges at low frequencies.

The time constants for different temperatures were obtained from the frequencies at which the imaginary permittivity is maximum. Thermally activated behavior was verified by fitting a plot of ln τ vs 1/T to the Arrhenius relation $\tau = \tau_0 \exp(E_a/kT)$ (Fig. 5.4). An activation energy of 0.211 eV and a characteristic time constant of $\tau_0 = 5.9 \times 10^{-10}$ s for this relaxation were obtained from the fit.

The activation energy of conduction for $YMnO_3$ is similar to the value of 0.36 eV reported by Moure *et al.* obtained from dc conductivity measurements [18], but smaller than the value of 0.63 eV reported by Rao *et al.* [19]. The electrical conduction in $RMnO_3$ (both hexagonal and orthorhombic) is due to the hopping of small polarons [19–21]. When a polarizable lattice is deformed, polarons are formed to compensate for the difference in electrical charge introduced. For manganites, polarons are formed when the oxidation state of the Mn cations is changed due to doping or non-stoichiometry. In the case of pure $YMnO_3$, the presence of polarons must result from non-stoichiometry.

Changing the electrode that was attached to the $YMnO_3$ single crystal from Ag (painted epoxy) to Au (sputtered) did not affect the frequency dispersion of the dielectric constant. Figure 5.5 shows the frequency dependence of the real and imaginary permittivity, as well as the ac conductivity, for

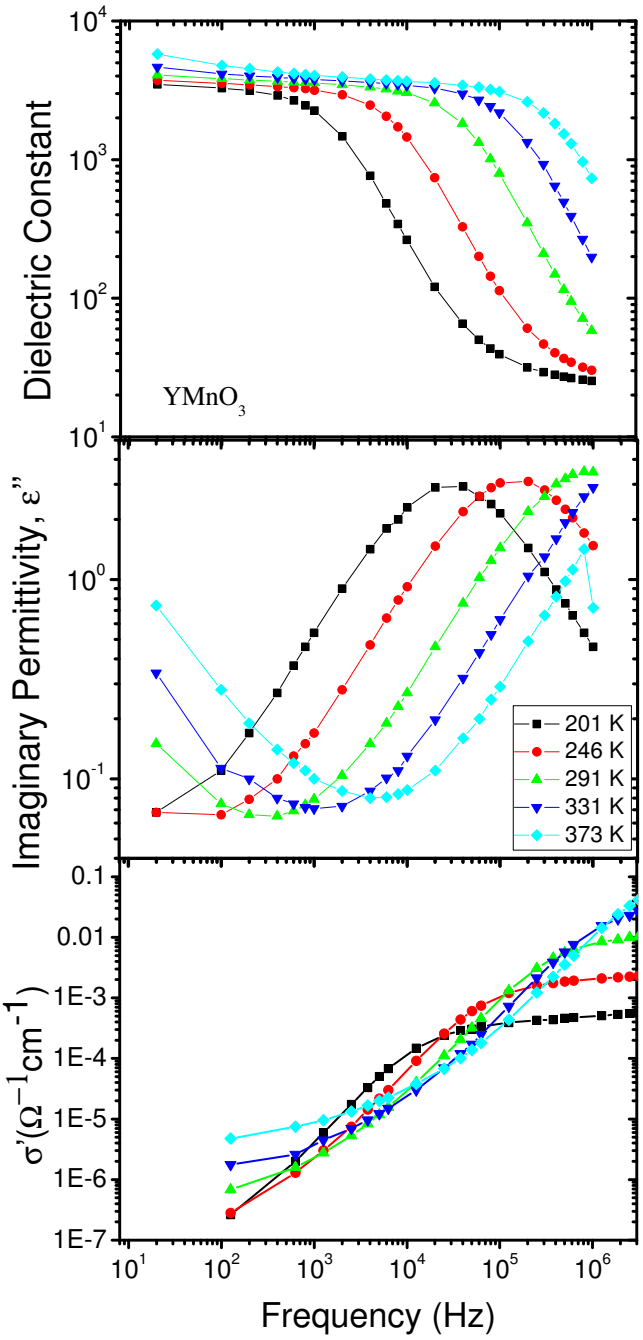

Figure 5.3: *Frequency dependence of (a) dielectric constant, (b) imaginary permittivity, and (c) ac conductivity of $YMnO_3$ single crystals with Ag contacts, at different temperatures.*

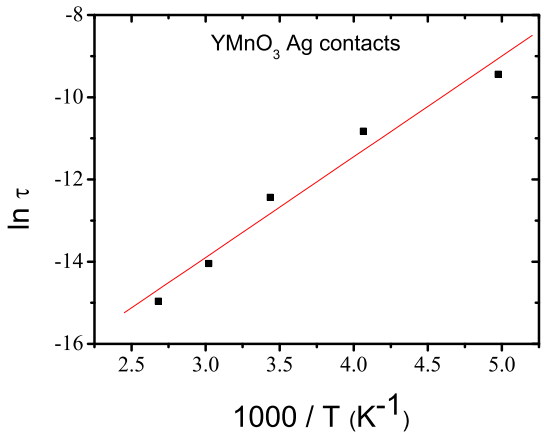

.

Figure 5.4: *ln (τ) vs. 1/T demonstrating Arrhenius behaviour*

$YMnO_3$ with Au contacts. The low-frequency dielectric constant was larger than that for samples with Ag contacts. The activation energy for the $YMnO_3$ with Au contacts was calculated as 0.36 eV.

The dielectric constants of $YMnO_3$ single crystals with Ag, (insert space here) Au and Pt electrodes at room temperature are plotted together in Fig. 5.6(a) by combining the measurements shown in Figs. 5.3 and 5.5. The dielectric constant plot of the sample with the Pt electrodes is introduced for the first time here. At low frequencies, the dielectric constant of $YMnO_3$ with Au electrodes is the largest; the sample with Ag electrodes exhibits the second largest dielectric constant while the sample with Pt electrodes has the smallest dielectric constant. The relaxation step occurs at approximately the same frequencies. The observation of the same high capacitance and the same relaxation behaviour for different electrodes suggests that the capacitance measured is not intrinsic to the sample. We also thinned down the sample to check if the capacitance scales down with thickness like a normal parallel plate capacitor obeying $C = \frac{\varepsilon_0 \varepsilon' A}{d}$. In Fig. 5.6(b) the room-temperature dielectric constant of the same crystal of $YMnO_3$ with two different thicknesses is shown. The capacitance remained almost unchanged. This indicates that the overall capacitance is not governed by the sample. It should be noted that the reproducibility of these measurements is an issue due to the difficulty of depositing the contacts in exactly the same manner each time. The deposition method used for the electrodes might also affect the dielectric behaviour of the samples [12].

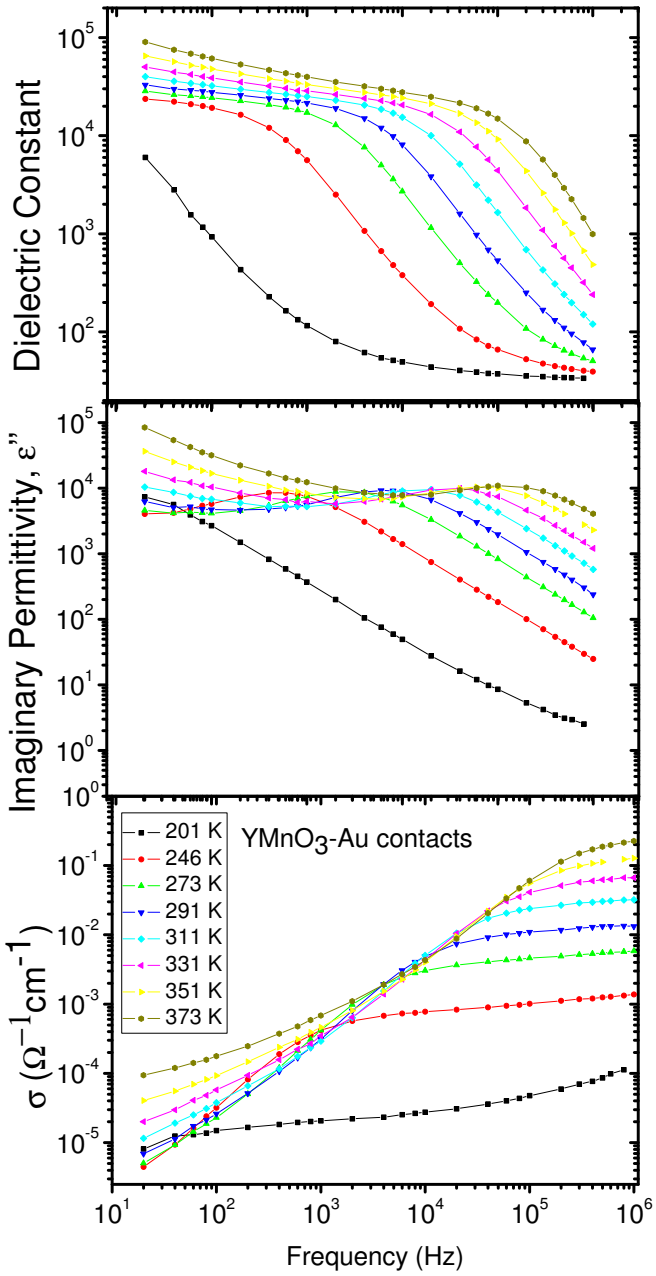

Figure 5.5: *Frequency dependence of (a) dielectric constant, (b) imaginary permittivity, and (c) ac conductivity of $YMnO_3$ single crystals with Au contacts, at different temperatures.*

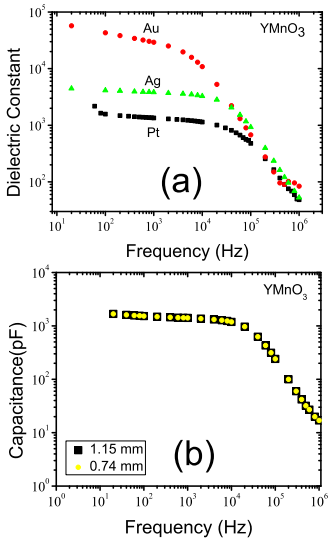

Figure 5.6: *Frequency dependence of (a) dielectric constant of $YMnO_3$ single crystals with Ag, Au and Pt contacts, (b) capacitance of the same crystal with Ag electrodes, having two different thicknesses.*

All of these observations signal the presence of relaxation phenomena. It is known that if a dielectric material is inhomogeneous, containing regions of different resistivity and capacitance, Maxwell-Wagner effects may arise and can lead to the formation of boundary layer (interfacial-depletion) regions. This is due to the different frequency response of different types of dipoles, in particular the space charge (interfacial) polarization associated with these depletion layers as explained in the first section of this chapter.

Cole-Cole plots at different temperatures for the $YMnO_3$ crystal with Ag contacts are shown in Fig. 5.7. The data lie on a single semicircle, which corresponds to the step in the real part and the peak in the imaginary part of the dielectric permittivity. For the two highest temperatures measured, a tail is present at the lowest frequencies. This feature is related to another relaxation mechanism which appears at high temperatures, and will not be discussed in this thesis.

The frequency dependence of the capacitance of the $YMnO_3$ single crystal with Ag contacts is shown again in Fig. 5.8. The solid lines are fits to the Cole-Cole equation (Eqn. 5.4) and reproduce the measurements exactly. The exponent α obtained from the fits, which represents the distribution of time constants, is between 0.185 and 0.325. The case where $\alpha = 0$ corresponds to the Debye Model, representing a single relaxation time. The small value of α indicates a strong correlation

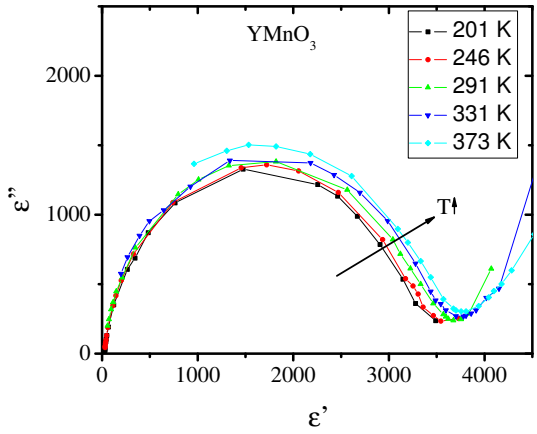

Figure 5.7: *Cole-Cole plots of $YMnO_3$ at different temperatures.*

between the relaxing entities [22]. The characteristic time constants can also be obtained from the fits (these were obtained earlier in this chapter as the inverse of the frequency at the maximum in imaginary permittivity). Using the time constants from the fits at different temperatures together with the Arrhenius-type relation $\tau = \tau_0 \exp(E_a/kT)$, the activation energy for the dispersion process was calculated as 0.248 eV, which is similar to the value calculated using time constants obtained from the maxima in the imaginary permittivity.

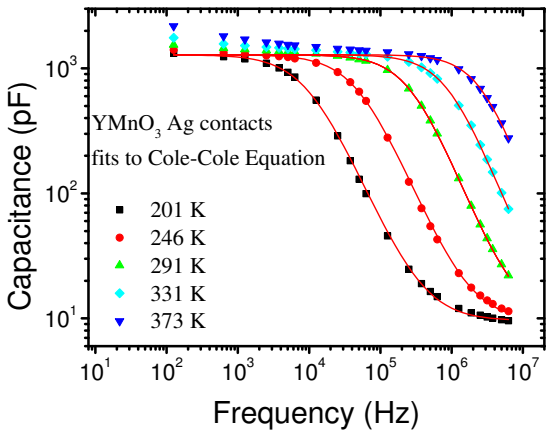

Figure 5.8: *Capacitance vs frequency reproduced from Fig. 5.2, thin lines are fits using the Cole-Cole equation as explained in the text.*

Returning to the origin of the large dielectric constants in these systems, one way of checking for the presence of Schottky barriers is to measure the effect of dc bias on the capacitance [23].

Schottky barriers form at electrode-semiconductor interfaces due to the difference in work functions of the metal and the semiconductor; electrons are injected either from the sample to the electrode or vice versa. Assuming a larger work function for the metal, electrons from a region of the sample close to the interface will be injected into the metal and a layer that is "depleted" of charge carriers will be formed. The width of this depletion layer depends on the voltage:

$$w = \sqrt{\frac{2\varepsilon}{qN_D}(V_b - V_a)} \tag{5.5}$$

Here, V_a is the external voltage, V_b is the internal junction voltage, q is the electron charge and N_D is the impurity concentration. Thus, the capacitance of the samples should change considerably with applied dc bias due to the change in width of the depletion layer. Although this statement is true for normal semiconductors, it is difficult to predict the behavior of a system containing two back-to-back Schottky barriers. Nevertheless, there are examples in the literature where the dc bias can indeed help to pinpoint the presence of interface polarization that results from depletion layers. For example, for hexagonal barium titanate crystals, the application of a small dc bias of the order of 1 V to a 0.3mm-thick single crystal affected the shape of the Cole-Cole plots appreciably [24]. For the perovskite $Pr_{0.6}Ca_{0.4}MnO_3$, an applied dc bias decreased the value of the capacitance significantly [23].

We have applied a dc bias of up to 1.5 V to our $YMnO_3$ single crystal with Ag contacts. The ac voltage applied during the measurements was fixed at 20 mV. Fig. 5.9 shows the frequency-dependent capacitance of $YMnO_3$ under dc bias. No change in the capacitance was observed at any frequency.

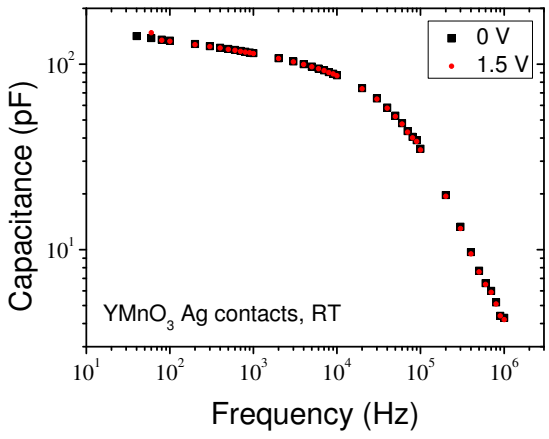

Figure 5.9: *Capacitance vs frequency measurements of $YMnO_3$ at zero bias and 1.5 V.*

After discussing the features of Schottky barriers, we can try to explain the larger dielectric constant that we observed for $YMnO_3$ with Au electrodes compared to that with Ag. This dierence might be ascribed to the different work functions of Ag (4.26 eV) and Au (5.1 eV). As the work function of Au is higher, the depletion layer formed will be thinner and therefore the capacitance of the depletion layer will be larger. However, the value measured for $YMnO_3$ with Pt electrodes does not obey the trend that follows from this discussion. Pt has an even larger work function (5.63 eV) than Au and the capacitance of $YMnO_3$ with Pt electrodes is expected to be largest. On the contrary, we measure the lowest values for the sample with Pt electrodes. We do not currently have an explanation for this observation.

Even though the dc bias experiments do not provide evidence for the presence of Schottky barriers, it is difficult to propose an alternative origin for the dielectric relaxation, as we discuss below. Maxwell-Wagner relaxation occurs for electrically inhomogeneous materials, at the interfaces between regions of different electrical conductivity. Inhomogeneity can arise from the presence of grains and grain boundaries in a polycrystalline material (internal boundary layer capacitors), or from a situation where the surface of the sample is electrically different to the bulk due to oxygen vacancies or to the presence of Schottky barriers at the electrode-sample interface. In our single crystal samples, there are no grain boundaries. The possible influence of oxygen vacancies was discounted by annealing the samples in oxygen and measuring the capacitance again, which showed no changes.

Another possible origin of the dielectric relaxation is polaron hopping. It has been reported for many different systems that the hopping of polarons not only contributes to the conductivity but also affects the dielectric constant [22, 25–27]. The hopping process is equivalent to the reorientation of an electrical dipole, which gives rise to frequency dependent dielectric behavior [25].

The frequency dependence of the ac conductivity for localized charge carriers is governed by Jonscher's power law, the "universal dielectric response" [5, 26, 28]:

$$\sigma' = \sigma_{dc} + \sigma_0 \omega^s \tag{5.6}$$

Here, w is the angular frequency given by $\omega = 2\pi f$, σ_0 and $s \leq 1$ are temperature dependent constants. Thus, a linear plot of logσ' vs logω gives the exponent s. If the ac conductivity obeys the universal dielectric response, one can argue that the same process (hopping of localized charge carriers) is also responsible for the behavior of the dielectric relaxation. As shown in Fig. 5.2, in the low-frequency range where the high dielectric constant is observed, the ac conductivity does not obey this universal behavior: the coefficient s extracted from Fig. 5.3 by fitting was approximately 1.4 at low frequencies, which is not consistent with the requirement of the universal dielectric response criteria: that is, $s \leq 1$. We note that a contribution from the electrode typically gives a shoulder in the

ac conductivity [28], as we observe for our $YMnO_3$ sample. In general, polaronic relaxation exists at low temperatures in crystals with defects [25], and is associated with small activation energies, of the order of 80 meV [25], and a small Arrhenius prefactor, $\tau_0 < 3\times10^{-13}$ s [28]. The activation energy that we obtained for $YMnO_3$ is three times larger than the typical value for polaronic relaxation, and we also obtained large prefactors (10^{-10} - 10^{-11}).

One more scenario can be suggested as the origin of interfacial polarization or Maxwell-Wagner relaxation. A single crystal is never perfect: on cooling from the growth temperature, many internal defects are induced, defining the mosaicity. The internal boundaries associated with the mosaicity may be responsible for the formation of interfacial regions between the semiconducting sample grains. However, the thickness independence of the capacitance at low temperatures [see Fig. 5.6(b)] suggests that such internal boundaries have negligible effect in this case.

In conclusion, although dc bias dependence experiments do not prove the presence of Schottky barriers, it is very unlikely that the dielectric behavior we observe is due to polaron hopping. Therefore, the large dielectric constant and the dielectric relaxation in $YMnO_3$ is more likely to arise from the formation of Schottky barriers. More experiments are necessary to support this conclusion.

5.3. Dielectric relaxation in $Tb_{1-x}Ca_xMnO_3$ ($0 \leq x \leq 0.1$) single crystals

5.3.1. Introduction

Giant dielectric constants that relax to low values have also been previously reported for the orthorhombic $RMnO_3$ perovskite: examples include $LaMnO_3$ [29, 30], $Pr_{0.7}Ca_{0.3}MnO_3$ [22], and $Pr_{0.6}Ca_{0.4}MnO_3$ [23]. However, different origins for the relaxation have been proposed in these studies. Neumeier *et al.* investigated $La_{1-x}Ca_xMnO_3$ ($0 \leq x \leq 1$) [29] and claimed not to observe "contact resistance" effects. The large capacitance measured was independent of applied dc bias from 0 to 2 V, and was attributed to the hopping of polarons. Lunkenheimer *et al.* also observed the same type of relaxation from "giant" to "normal" capacitance for $LaMnO_3$, but associated it with the space charge that was formed due to Schottky barriers at the electrode-sample interface [30]. Likewise, the origin of the large dielectric constant measured for $Pr_{0.7}Ca_{0.3}MnO_3$ was claimed to be polaron hopping [22], whereas for $Pr_{0.6}Ca_{0.4}MnO_3$ it was suggested that Schottky barriers are instead responsible [23].

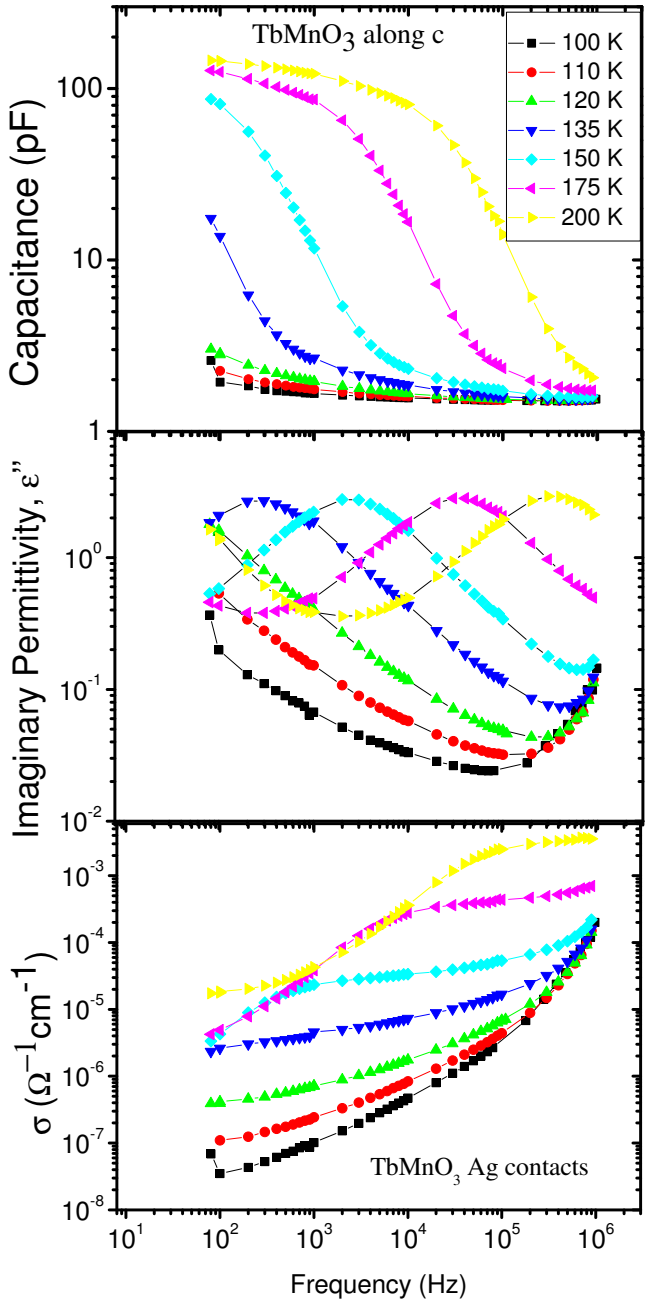

Figure 5.10: *Frequency dependence of (a) dielectric constant, (b) imaginary permittivity, and (c) ac conductivity of $TbMnO_3$ single crystals with Ag contacts, at different temperatures.*

5.3.2. Results and Discussion

We have also observed a giant dielectric constant and relaxation phenomena at high temperatures or low frequencies in single crystal $TbMnO_3$, grown using a floating zone furnace. $TbMnO_3$ is one of the most widely studied multiferroics, belonging to the class of ferroelectrics with spiral magnetic structures. Antiferromagnetic ordering takes place below 41 K, and the ferroelectric transition coincides with a so-called lock-in transition of the magnetic propagation vector and the onset of spiral spin ordering below 26 K [31]. The ferroelectricity in $TbMnO_3$ has been shown to be a direct result of the spiral magnetic ordering [32].

The real and imaginary parts of the dielectric permittivity, as well as the ac conductivity, are shown in Fig. 5.10. We observe that above 135 K, the capacitance of the sample at low frequencies is large. The activation energy calculated using the relationship $\tau = \tau_0 \exp(E_a/kT)$ is 0.267 eV. The time constant, τ, was taken as the inverse of the frequency at the maximum in imaginary permittivity. In similar fashion to $YMnO_3$, the electrical conduction in $TbMnO_3$ is known to involve the hopping of polarons [20]. The presence of a small proportion of Mn^{4+} has been previously reported for pure $TbMnO_3$, because a slight non-stoichiometry is unavoidable [33]. When $RMnO_3$ perovskites are doped with a divalent cation such as Ca^{2+}, the activation energy of the conduction varies linearly with the dopant content (and thus with Mn^{3+} content), as reported for the series $La_{1-x}Ca_xMnO_3$. This observation has been related to the degree of cooperative Jahn-Teller distortion present, which is also proportional to the Mn^{3+} content [34]. We have observed a similar trend for single crystal samples of Ca-doped $TbMnO_3$: the activation energy for the hopping of polarons decreases with Ca doping, that is, with increasing Mn^{4+} content. We obtained activation energies of 0.267 eV, 0.176 eV and 0.107 eV for samples with x = 0, 0.05 and 0.1, respectively. The degree of Jahn-Teller distortion increases monotonically through the series La-Nd-Ho, as illustrated by the activation energies of 0.215 eV reported for $LaMnO_3$, 0.245 eV for $NdMnO_3$, and 0.373 eV for $HoMnO_3$ [20]. The activation energy that we obtained for pure $TbMnO_3$, 0.267 eV, fits well between the reported values for $NdMnO_3$ and $HoMnO_3$. It is not possible to compare with hexagonal $YMnO_3$ within this framework, because Mn^{3+} is not Jahn-Teller active in trigonal bipyramidal coordination [35].

The frequency dependence of the capacitance of a different $TbMnO_3$ crystal under a 1.5 V dc bias is shown in Fig. 5.11. We observe that the capacitance of the sample in the low frequency range decreases when the dc bias is applied. The dependence of the capacitance on dc bias gradually becomes weaker as the frequency is increased, and at the highest frequencies measured the dc bias has almost no effect on the capacitance. Nevertheless, unlike $YMnO_3$, the extrinsic capacitance of $TbMnO_3$ depends to some extent on the dc bias applied. Following the discussion above for $YMnO_3$, two possible mechanisms can again be proposed for the observed dielectric relaxation in $TbMnO_3$:

polaron hopping and Schottky barrier formation. The polaron hopping is unlikely to be the origin of the relaxation because the ac conductivity does not fit the universal dielectric response model, i.e. the coefficient s obtained from the fits to Eqn. 5.6 is larger than 1 in the low frequency regime where we observe the large and extrinsic contribution to the dielectric constant. The dc bias dependence of the capacitance points strongly to the presence of Schottky barriers.

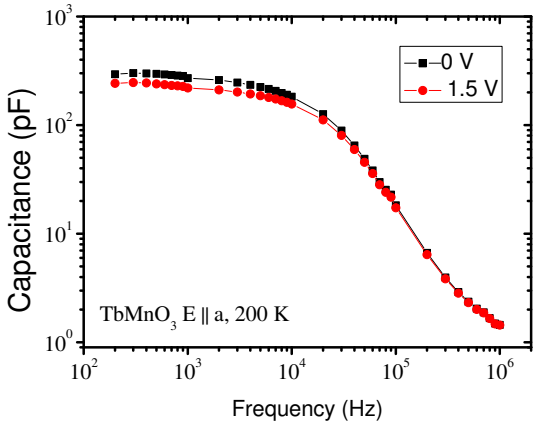

Figure 5.11: *Capacitance vs frequency measurements of $TbMnO_3$ at zero bias and 1.5 V.*

5.4. Polaronic relaxation in polycrystalline $Er_2Cu_2O_5$

As stated in sections 5.2 and 5.3, polaron hopping can contribute to the dielectric constant and give rise to relaxation behavior. Polaron hopping can also lead to the measurement of large dielectric constants. Polycrystalline $Er_2Cu_2O_5$ samples (measured in Chapter 3 of this thesis to demonstrate the presence of magnetodielectric coupling at low temperatures) have previously been shown to possess large dielectric constants at room temperature and low frequencies due to polaron hopping [36]. In order to demonstrate how a diagnosis of dielectric relaxation due to polaron hopping can be made, we have reproduced the measurements reported in ref. [36].

The frequency dependence of the dielectric constant, dielectric loss and ac conductivity is shown in Fig. 5.12. In contrast to the other systems examined in this chapter, there is no step-like transition in the dielectric constant and dielectric loss. The dielectric constant increases following a power law as the frequency is decreased, while the dielectric loss exhibits very broad peaks. The ac conductivity was calculated using the expression $\sigma_{ac} = \omega \times \varepsilon_0 \times \varepsilon$", as described in section 5.2.

The ac conductivity at 201 K is linear up to large frequencies and we obtained an exponent s of 0.46, from the fits to the universal dielectric response equation (5.6). This suggests that the ac

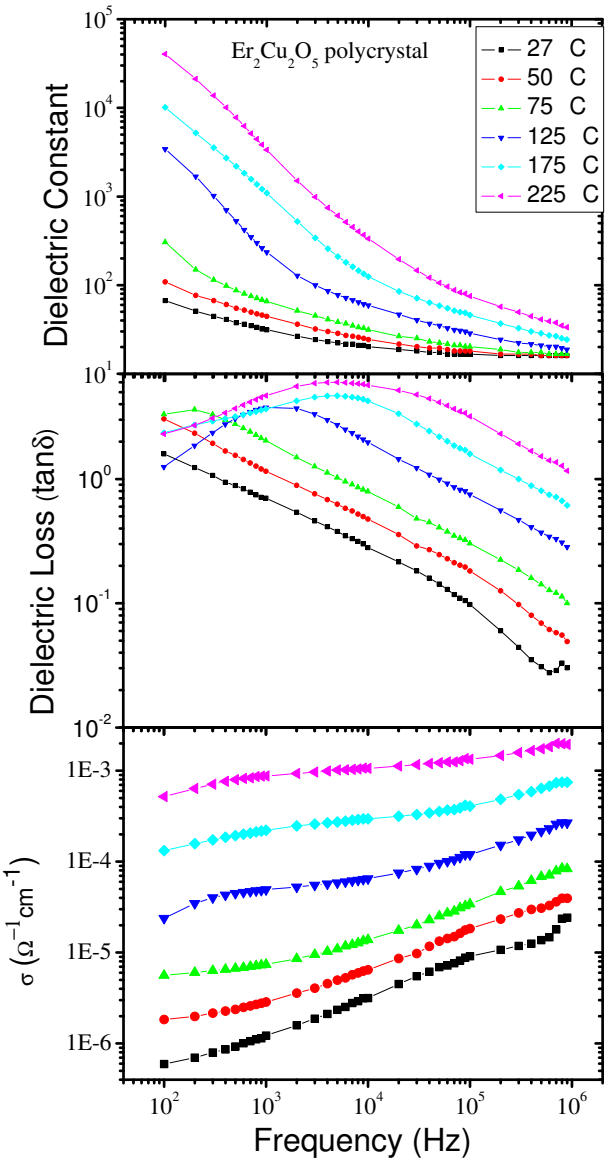

Figure 5.12: *Frequency dependence of (a) dielectric constant, (b) imaginary permittivity, and (c) ac conductivity of polycrystalline $Er_2Cu_2O_5$ with Ag contacts, at different temperatures.*

conductivity behaves according to the universal dielectric response.

This type of behavior, a dielectric constant that decreases at low frequencies following a power law and ac conductivity that is consistent with the universal dielectric response, has previously been observed in other systems such as La_2CuO_4 [27] and is associated with the hopping of polarons.

5.5. Conclusions

The non-intrinsic nature of the high dielectric constant and dielectric loss in hexagonal $YMnO_3$ and orthorhombic $TbMnO_3$ has been demonstrated using frequency, electrode and thickness-dependent dielectric measurements. The activation energies calculated for both the orthorhombic and hexagonal manganites are approximately 0.2 eV. The decrease of the activation energy on Ca-doping in $TbMnO_3$ is consistent with polaronic conduction. However, polaronic conduction can be ruled out as the cause of the dielectric relaxation because the ac conductivity of the samples does not obey the universal dielectric response. Despite the lack of proof provided by dc bias-dependent capacitance measurements on $YMnO_3$, the only possible remaining explanation for the Maxwell-Wagner relaxation observed in both types of materials is the presence of Schottky barriers at the contact-sample interface.

For the case of $Er_2Cu_2O_5$ samples, we were able to reproduce the results reported in [36], showing that polaron hopping might indeed result in dielectric relaxation.

Bibliography

[1] J. F. Scott, J. Mater. Res. 22, 2053 (2007).

[2] J. F. Scott, J. Phys.: Condens. Matter, 20, 021001, (2008).

[3] G. Catalan, Appl. Phys. Lett. 88(10), 102902, (2006).

[4] B. Pevzner, Msc. Thesis, Massachusetts Institute Of Technology, (1995).

[5] A. K. Jonscher, Dielectric Relaxation in Solids, Chelsea Dielectrics Press, 1983.

[6] J. Hemberger, P. Lunkenheimer, R. Fichtl, H.-A. Krug von Nidda, V. Tsurkan, and A. Loidl, Nature (London) 434, 364 (2005).

[7] G. Catalan and J. F. Scott, Nature (London) 448, E4-E5 (2007).

[8] S. Weber, P. Lunkenheimer, R. Fichtl, J. Hemberger, V. Tsurkan, and A. Loidl, Phys. Rev. Lett., 96, 157202, (2006).

[9] G. A. Samara, J. Phys.: Condens. Matter 15, R367, (2003).

[10] A. P. Ramirez, M. A. Subramanian, M. Gardel, G. Blumberg, D. Li, T. Vogt, S.M. Shapiro, Solid State Commun., 115(5), 217, (2000).

[11] C. C. Homes, T. Vogt, S. M. Shapiro, S. Wakimoto, A. P. Ramirez, Science, 293(5530), 673, (2001).

[12] P. Lunkenheimer, R. Fichtl, S. G. Ebbinghaus, A. Loidl, Phys. Rev.B, 70(17), 172102, (2004).

[13] D. C. Sinclair, T. B. Adams, F. D. Morrison, A. R. West, Appl. Phys. Lett. 80(12), 2153, (2002).

[14] J. Li, A. W. Sleight, and, M. A. Subramanian, Solid State Commun. 135(4), 260, (2005).

[15] G. A. Smolenskii and V. A. Bokov, J. Appl. Phys. 35, 915, (1964).

[16] Z. J. Huang, Y. Cao, Y. Y. Sun, Y. Y. Xue, C. W. Chu, Phys. Rev.B, 56(5), 2623, (1997).

[17] G. Nénert, M. Pollet, S. Marinel, G. R. Blake, A. Meetsma, T. T. M. Palstra, J. Phys.: Condens. Matter, 19, 466212, (2007).

[18] C. Moure, J. F. Fernandez, M. Villegas, P. Duran, J. Eur. Ceram. Soc., 19 (1),131-137, (1999).

[19] G. V. S. Rao, B. M. Wanklyn, C. N. R. Rao, J Phys. Chem. Solids, 32(2), 345, (1971).

[20] L. Martin-Carron, R. Ramirez, C. Prieto, A. de Andres, J. Sanchez-Benitez, M. Garcia-Hernandez, J. L. Martinez, Journal of Alloys and Compounds, 323, 527, (2001).

[21] T. T. M. Palstra, A. P. Ramirez, S.-W. Cheong, B. R. Zegarski, P. Schiffer, and J. Zaanen, Phys. Rev. B, 56, 5104, (1997).

[22] R. S. Freitas, J. F. Mitchell, P. Schiffer, Phys. Rev.B, 72(14), 144429, (2005).

[23] N. Biskup, A. de Andres, J. L. Martinez, C. Perca, Phys. Rev.B, 72, 024115, (2005).

[24] J. Yu, T. Ischikawa, Y. Arai, S. Yoda, M. Itoh, and Y. Saita, Appl. Phys. Lett. 87, 252904 (2005).

[25] O. Bidault, M. Maglione, M. Actis, M. Kchikech, B. Salce, Phys. Rev.B, 52(6), 4191, (1995).

[26] C. C. Wang and L. W. Zang, Appl. Phys. Lett. 90, 142905, (2007)

[27] C. Y. Chen, R. J. Birgeneau, M. A. Kastner, N. W. Preyer, and T. Thio, Phys. Rev. B, 43(1), 392, (1991).

[28] Seeger, P. Lunkenheimer, J. Hemberger, A. A. Mukhin, V. Yu. Ivanov, A. M. Balbashov, and A. Loidl, J. Phys.: Condens. Matter 11, 3273, (1999).

[29] J. L. Cohn, M. Peterca, J. J. Neumeier, Phys. Rev.B, 70(21), 214433, (2004).

[30] P. Lunkenheimer, V. Bobnar, A. V. Pronin, A. I. Ritus, A. A. Volkov, A. Loidl, Phys. Rev.B, 66, 052105, (2002).

[31] T. Kimura, T. Goto, H. Shintani, K. Ishizaka, T. Arima, Y. Tokura, Nature, 426, 55, (2003).

[32] M. Mostovoy, Phys. Rev. Lett., 96(6), 067601, (2006).

[33] J. Blasco, C. Ritter, J. Garcia, de Teresa JM, J. Perez-Cacho, M.R. Ibarra, Phys. Rev.B, 62(9), 5609, (2000).

[34] J. M. De Teresa , K. Dorr, K. H. Muller, L. Schultz, R. I. Chakalova, Phys. Rev.B, 58(10), R5928, (1998).

[35] B. B. Van Aken, J. W. G Bos, R. A. de Groot, and T. T. M. Palstra, Phys. Rev. B. 63, 125127, (2001).

[36] G. Knebel, P. Lunkenheimer, A. Loidl, G. Wltschek, and H. Fuess, Journal of Alloys and Compounds, 216, 99-103, (1994).

[37] A. K. Jonscher, Journal of Materials Science, 16, 2037, (1981)

Summary

The study of multiferroics, materials that display simultaneous magnetic and electric ordering, has become one of the most popular areas in the field of solid state physics since the discovery of large magnetoelectric coupling in $TbMnO_3$ in 2003. Even though the magnetoelectric coupling in $TbMnO_3$ is relatively large, utilizing multiferroics as new multistate memory elements is not yet possible since the magnetic (electric) fields necessary to switch the electric (magnetic) state of the materials are too high to be used in memory devices. Therefore, a better theoretical understanding of the magneto(di)electric coupling mechanisms in both current and new materials is required.

This thesis aims to understand magnetodielectric coupling in transition metal oxides. Most known multiferroic and magneto(di)electric materials show weak magneto(di)electric coupling except for a few prominent examples that have spiral magnetic structures. We take two main approaches towards investigating magnetodielectric coupling mechanisms in this thesis. In our first approach, we systematically study the magnetodielectric coupling in a known multiferroic system. We investigate both the effect of varying the rare-earth cation and of substituting non-magnetic Ga^{3+} for Mn^{3+}, which enable us to vary the magnetic exchange interactions systematically. We model the resulting response in magnetocapacitance using Landau theory .

Materials displaying the linear magnetoelectric effect are more abundant than multiferroics because the symmetry requirements are less strict; rather few materials are currently known despite the discoveries of new mechanisms allowing magnetically induced ferroelectricity. In our second approach, we use basic principles of crystallographic and magnetic symmetry to identify and study a family of polar, magnetic compounds that allow the linear magnetoelectric effect -the $R_2Cu_2O_5$ materials.

In Chapter 1, we give a broad overview of the field. First we introduce the terminology and differentiate between similar terms sometimes used for the same purpose in the literature, such as magnetodielectric coupling and magnetoelectric coupling. We justify the necessity of defining a new

class of materials, magnetodielectrics, in addition to the linear magnetoelectrics and multiferroics. We introduce prominent examples of each class of materials from the literature, and present some aspects of how magnetodielectric coupling can be modeled theoretically.

In Chapter 2, we describe the experimental methods used in this thesis. (Magneto)capacitance and pyroelectric current measurements are explained in detail.

In Chapter 3, we follow the process of identifying new materials that might show a magnetodielectric response, choosing $R_2Cu_2O_5$ as a promising family of compounds to investigate. We demonstrate that the magnetocapacitance measurements can be more sensitive to magnetic phase transitions than conventional magnetization measurements, allowing complex magnetic phase diagrams to be mapped as a function of temperature and magnetic field. Our investigation of $Y_2Cu_2O_5$ shows that the dielectric constant is larger in the intermediate-field spin-flip phase which allows a net moment, than in the low-field antiferromagnetic phase and the high-field spin-flop phase.

In Chapter 4, we present the results of our extensive study of the magnetodielectric coupling in hexagonal $RMnO_3$ materials. We show that structural characterization using X-ray diffraction can be a convenient way to study ferroelectric properties such as dipole moments and ferroelectric transition temperatures. We demonstrate the trends in these properties that occur with atomic substitution on both R and Mn sites. We then demonstrate the presence of magnetodielectric coupling in $RMnO_3$ (R = Y, Yb, Er) by studying the anomaly in ε(T) that exists shortly below T_N and by performing magnetocapacitance [ε(H)] measurements at different temperatures. For $YMnO_3$ single crystals, we use Landau theory to explain that the anomaly in ε(T) originates from a term P^2L^2 in the free energy. Similarly, we demonstrate that the quadratic magnetocapacitance behavior of $YMnO_3$ originates from a free energy term P^2H^2. For $YbMnO_3$ single crystals, we observe an anomaly in the magnetocapacitance at T_N; we use Landau theory to model the shape of the curves and to show that the origin of the magnetocapacitance anomaly is competition between two antiferromagnetic phases, one of which allows a net magnetization. We map the magnetic phase diagrams of $RMnO_3$ (R = Y, Yb, Er), using magnetization and magnetocapacitance measurements in applied fields of up to 30 T. We propose symmetries for the magnetic phases of $YMnO_3$ and reveal a previously unknown phase transition in $ErMnO_3$ at high fields and low temperatures. Finally, we study $YMn_{1-x}Ga_xO_3$ and show that despite causing a decrease in T_N, Ga-doping increases the magnetocapacitance of $YMnO_3$ remarkably. We speculate that this is due to the local canting of frustrated spins caused by diluting the magnetic Mn^{3+} sublattice with diamagnetic Ga^{3+}.

In Chapter 5, we characterize the intrinsic and extrinsic contributions to the dielectric constant in the families of compounds examined in the previous chapters. Such a study is indispensable in order to identify the real, intrinsic response of a sample, a topic that has been of much debate in the literature. We start by giving an overview of various mechanisms of intrinsic (ionic and electronic)

and extrinsic (space charge) polarizability and suggest ways by which they can be differentiated. We suggest that Maxwell-Wagner relaxation takes place in the vicinity of room temperature in the multiferroic hexagonal $YMnO_3$ materials and in multiferroic $TbMnO_3$ perovskite, which masks the intrinsic sample response.

In conclusion, even though the materials studied in this thesis show rather weak magnetodielectric coupling, this study provides clues for obtaining strong magnetodielectric coupling and valuable insight into the mechanisms of the coupling. We also establish magnetocapacitance measurements as a technique to study materials with complex magnetic phase diagrams. Further experiments on a variety of different systems are necessary to fully understand the interplay of phonons, magnetism and electrical dipoles.

Samenvatting

Het onderzoek in de vaste stof fysica naar materialen die tegelijkertijd zowel magnetisch als elektrisch geordend zijn, ook wel bekend als multiferroica, heeft een hoge vlucht genomen sinds de ontdekking van sterke magnetoelektrische koppeling in $TbMnO_3$ in 2003. Ondanks de relatief sterke magnetoelektrische koppeling in $TbMnO_3$, is het nog niet mogelijk gebleken om multiferroische materialen als geheugenelementen toe te passen. Toepassing als geheugencel is nog niet mogelijk omdat de voor het schakelen benodigde magnetische (elektrische) velden nog te hoog zijn. Dit noopt tot een beter begrip van magnetodielektrische koppelingsmechanismen in zowel bestaande als nieuwe materialen.

Dit proefschrift stelt zich ten doel om tot een beter begrip te komen van magnetodielektrische koppeling in overgangsmetaaloxiden. Terwijl de meeste bekende multiferroische en magnetodilektrische materialen zwakke magnetodielektrische koppeling vertonen, vormen een aantal in het oog springende materialen met magnetische spiraalstructuren hierop een uitzondering. We benaderen in dit proefschrift het onderzoek naar magnetodilektrische koppeling in overgangsmetaaloxiden vanuit twee invalshoeken. De eerste invalshoek omvat een stelselmatige bestudering van magnetodielektrische koppeling in een bekend multiferroisch systeem. Hierbij variëren we het zeldzame aard kation en vervangen we Mn^{3+} door niet magnetisch Ga^{3+} om zo de magnetische wisselwerkingsinteracties systematisch te benvloeden. We beschrijven de magnetocapaciteitsrespons vervolgens aan de hand van Landau theorie.

Materialen die een lineair magnetoelektrisch effect vertonen, komen veelvuldiger voor dan multiferroica, aangezien de opgelegde symmetrie eisen in het eerste geval minder stringent zijn. Er zijn vele mechanismen ontdekt die magnetisch geïnduceerde ferroelektrische ordening faciliteren, maar dit heeft slechts tot enkele nieuwe materialen geleid.

De tweede invalshoek bestaat uit het toepassen van beginselen uit de kristallografie en de magnetische symmetrie om zo een familie polaire en magnetische materialen die het lineair magnetoelektrisch effect toestaat, te herkennen en vervolgens hun gedrag te bestuderen -de $R_2Cu_2O_5$ materialen.

In hoofdstuk 1 komt een globaal overzicht van het onderzoeksveld aan bod. We introduceren de basisbegrippen en maken tevens onderscheid tussen vergelijkbare terminologie die voor hetzelfde doeleind wordt gebezigd, zoals magnetodielektrische koppeling en magnetoelektrische koppeling. We rechtvaardigen de noodzaak om een nieuwe klasse materialen -magnetodielektrica- te definiren, naast de bestaande magnetoelektrica en multiferroica. Aan de hand van literatuurvoorbeelden presenteren we saillante voorbeelden van elke materiaalklasse en lichten we tevens toe op welke wijze de magnetodielektrische koppeling theoretisch gemodelleerd kan worden.

Hoofdstuk twee beschrijft de experimentele technieken die in dit proefschrift gebruikt worden. We zullen met name de details van (magneto)capacitieitsmetingen en pyroelektrische stroommetingen uitvoerig behandelen.

In hoofdstuk 3 volgen we de selectieprocedure van nieuwe materialen die een mogelijke di lektrische respons bezitten, waarbij we waarbij we $R_2Cu_2O_5$ uitkiezen als veelbelovende materiaalfamilie die in aanmerking komt voor onderzoek. We tonen aan dat magnetocapaciteitsmetingen een grotere gevoeligheid bezitten voor magnetische faseovergangen dan conventionele magnetische metingen. Hierdoor kunnen we complexe magnetische fasediagrammen als functie van temperatuur en magnetisch veld geconstrueren. Ons onderzoek toont aan dat de dielektrische constante van $Y_2Cu_2O_5$ hoger is bij gematigde veldsterkten in de spin-flip fase die een netto moment toelaat, in vergelijking tot de laagveld antiferromagnetische fase en de hoogveld spin-flop fase.

In hoofdstuk 4 bespreken we de resultaten van ons onderzoek naar magnetodielektrische koppeling in hexagonale manganaten. We laten zien dat Röntgendiffractie zich uitstekend leent voor karakterisatie van ferroelektrische eigenschappen, zoals dipool momenten en ferroelektrische ordeningstemperaturen. We brengen trends in deze eigenschappen in verband met substituties op R en Mn roosterposities. Vervolgens leveren we het bewijs van magnetoelektrische koppeling in $RMnO_3$ (R=Y, Yb, Er) aan de hand van een dielektrische anomalie in ε(T) die net boven de Néel temperatuur optreedt en magnetocapaciteit [ε(H)] metingen bij verschillende temperaturen.

We passen de Landau theorie toe op éénkristallen van $YMnO_3$ om te bewijzen dat de anomalie in ε(T) voortvloeit uit een vrij energie term P^2L^2 . Analoog hieraan tonen we aan dat de kwadratische magnetocapaciteit van $YMnO_3$ voortkomt uit een vrij energie term P^2H^2. In éénkristallen van $YbMnO_3$ hebben we een anomalie in de magnetocapaciteit bij T_N waargenomen. We maken gebruik van de Landau theorie om de vorm van deze curves te verklaren. Tevens tonen we aan dat competitie tussen twee antiferromagnetische fasen, waarvan één fase netto magnetisatie toelaat, ten grondslag ligt aan deze magnetocapaciteitsanomalie.

Aan de hand van magnetisatie- en magnetocapaciteitsmetingen waarbij magnetische velden tot 30 T worden gebruikt, construeren we magnetische fasediagrammen van $RMnO_3$ (R=Y,Yb,Er). We stellen ten behoeve van elk van de magnetische fasen van $YMnO_3$ een symmetrie voor en brengen een voorheen onbekende faseovergang in $ErMnO_3$ aan het licht, die optreedt bij hoge velden en lage temperaturen. Tot slot bestuderen we $YMn_{1-x}Ga_xO_3$ en laten zien dat ondanks het feit dat gallium doping een verlagend effect heeft op de Néel temperatuur, de magnetocapaciteit aanzienlijk wordt vergroot. We veronderstellen dat dit wordt veroorzaakt door het kantelen van gefrustreerde spins als gevolg van het verdunnen van het Mangaan subrooster met diamagnetisch Gallium.

In hoofdstuk 5 karakteriseren we de intrinsieke en extrinsieke bijdragen aan de dielektrische constante in de materiaalfamilies die in de voorgaande hoofdstukken aan bod zijn gekomen. Een dergelijke studie is van onschatbare waarde om de echte, intrinsieke materiaalrespons te kunnen onderscheiden, dit onderwerp staat in de literatuur geregeld ter discussie. We starten met een overzicht van de verschillende intrinsieke (ionverplaatsing en elektronisch) en extrinsieke (ruimtelading) mechanismen die bij kunnen dragen aan polariseerbaarheid en stellen manieren voor om ze van elkaar te onderscheiden.

We spreken het vermoeden uit dat Maxwell-Wagner relaxatie optreedt bij kamertemperatuur in multiferroische hexagonaal $YMnO_3$ en in $TbMnO_3$ met perovskietstructuur en dat dit de intrinsieke materiaalrespons maskeert.

Ook al vertonen de materialen in dit proefschrift zwakke magnetoelektrische koppeling, de aanwijzingen en waardevolle inzichten in koppelingsmechanismen die in dit werk naar voren komen, kunnen als richtsnoer dienen voor toekomstig onderzoek. We hebben vastgesteld dat de magnetocapaciteitsmeting een gangbare techniek is om materialen met complexe magnetische fasediagrammen te bestuderen. Vervolgonderzoek naar verschillende systemen is onontbeerlijk om de wisselwerking tussen fonons, magnetisme en elektrische dipolen volledig te kunnen begrijpen.

Acknowledgements

After long 4 years and 8 months, I am able to write the acknowledgements. It is supposed to be one of the easy parts but it is not. Dear Thom, from the day I arrived to Groningen till the day I started to look for a job, you have been a caring supervisor. First years were difficult for me scientifically, since we were new in the field of multiferroics. The measurements had to be setup, the topics had to be distributed. This learning period delayed my progress, but in the end I think you have given the right decisions. You formed the small multiferroics group in such a way that in the end we complemented each other. I appreciate your attitude to notice and reveal one's strengths than the weaknesses. I think I abused your open door policy last years. I learned from you how to measure, analyze and present exprerimental data. You have been a "democratic" supervisor. You paid attention to take the thoughts from everyone, and listened even the most awkward thought. You were also sensitive about my problems unrelated to work and my career struggles. Thanks for everything!

Graeme, thanks for being always available for questions. Your corrections and suggestions about my thesis simplified my job enormously. Thank you for being my copromotor.

Beatriz Noheda played the key role to improve the working conditions in the lab. I benefited a lot from her suggestions and constant encouragement. Thank you Beatriz for always asking how it is going and listening me complaining afterwards. Even though I couldn't use it, thank you also for giving me career advice.

Maxim Mostovoy contributed significantly to this thesis. His theoretical modeling was crucial to understand the magnetoelectric coupling in hexagonal manganites. Thank you Maxim for your efforts and time that you spent to explain me the physics. Thanks also for the small paths in the forests of Stuttgart.

Michael Pollet and Agung Nugroho were my daily supervisors during the first years. Thank you Michael for being a patient teacher and sharing coffee time with me. I also value your efforts

to improve the social atmosphere of the group. Most of the crystals that I measured in this thesis were grown by Agung. Thank you Agung for all those crystals, answering my questions and your collaboration over the years.

I would like to thank to my reading committee members, Prof. Bernd Büchner, Prof. Tsuyoshi Kimura, and Prof. Charles Simon for their corrections and suggestions.

The chapter about the dielectric relaxation couldn't be possible without the help of Gustau Catalan. Thank you Gustau for your swift replies, guidance and support over the years.

We worked with Arramel for his masters thesis research on the cuprates of Chapter 3. Thank you Arramel for getting excited with me during our measurements, being present at long measurement nights and your big contribution to my thesis. Natalia Bellido and Prof. Charles Simon made me a part of the high magnetic field experiments at Grenoble that initiated a very nice collaboration on hexagonal manganites. Thanks Natalia for hosting me at Grenoble and for the nice discussions. I thank Dr. Albin de Muer and Dr. Rudolphe Boursier for their contributions to the long measurement nights. For the high magnetic field experiments at Nijmegen High Field Magnet Laboratory, I would like to thank to Erik Kampert and Dr. Uli Zeitler for their excellent assistance and hosting.

I have to mention Nandang Mufti specially. We worked both on multiferroics and shared an office for long time. Dear Mufti, even if we have a contrasting style and we make fun from arguing, I think we complemented each other a lot. Your extraordinary talent for experimenting and your tendency to try and see if something works or not solved many problems in the lab. I interrupted you many times to ask something and you never complained, always gave me a reply. Thanks also for the crystal of $Y_2Cu_2O_5$ and synthesis advice. I wouldn't be able to collect all the data if you didn't develop various experimental setups. Gwilherm (Nénert) was also working partly on multiferroics. Even though sometimes our interests overlapped, we could benefit from this and managed to start some collaborations, which seems to continue now at our new positions. Thank you Gwilherm for your symmetry input, your ideas, Nancy summerschool and dinners at the Greek restaurant. Even if we didn't work on the same project, Claire Colin contributed to the research on multiferroics and to my thesis. More importantly she improved the group atmosphere and organized activities. Thank you Claire for these and your friendship. I shared the office also with Igor and lately Johan. Thanks Igor for tolerating our frequent discussions with Mufti and for your friendship. Johan, thanks for all your help and friendship over the years, tolerating my views about the political situation in Turkey. Thank you also for translating my summary into Dutch and accepting to be one of my paranimphs.

Thanks to Auke Meetsma, our expert crystallographer, for the single crystal diffraction work which resulted the publication on Ga doped $YMnO_3$ and his help to analyze the crystal structures. I thank Jacob Baas for solving many experimental problems, and being present daily in the labs for questions and keeping, among other devices, the MPMS and PPMS running. Thanks to Ubel Linstra

and Kees Omkees for their cooperation and liquid He supply. I would like to thank our secretary Henriet van Mil for taking great care of the paperwork.

I also thank all the past and current members of the Solid State Chemistry Group. Thank you for contributing to the nice atmosphere, for the lunch breaks, Lunteren, Vlieland and Veldhoven days and labuitjes. Thank you Vadim, Oana-Odi(you still owe me a rematch), Diego, Ard, Mylene, Gijsbert, Gwilherm, Coen, Mufti, Prof. Rob de Groot, Igor, Anne, Syarif, Christophe, Michael, Claire, Johan, Arramel, Jose, Marinda-Szily (my neighbours at the next apartment), Henk, Jacob, and visitors Alexander and Javier.

I met many friends at the Dutch course and some of them I continued to meet. Thanks to Fresia, Kamila, Stephane and Kristin and Paco. In particular, thank you Fresia, for lots of activities, keeping in touch and last minute latex template!

My first months were not so smooth at the international student house. Thanks to my late neighbours, things become better. Thank you Asal, Qui and Cindy for being caring neighbours and your friendship. For almost two years Eda-Aksel and Deniz were the only Turkish people that I knew. They were like family to me, sharing -unfortunate for them- mostly my worries. I can't thank them enough. Later, Turkish students community expanded. Thank you Burcu and Umut Konuş for the films, RKZ Bios visits, raki nights and other activities. Very lately, the group was big enough to gather at Paard van Troja. Thanks to İdil, Can (thanks for our ambitious tennis days)-Özlem, Kanat, Onur, Ebru Burcu, Araz, Cihan, Nadir. I enjoyed to do some sports in Groningen. Thanks to Johan Lambregs for cycling and his friendship. Thanks also to Daniele Fausti for tabletennis sessions and his friendship.

Finally, I thank to my parents. They constantly supported me from distance and without their support, this thesis wouldn't be complete. I am sure that I forgot people. Thanks to everyone who contributed to make my years in Groningen enjoyable!